

**DURABLE SPRAY-APPLIED FIRE-RESISTIVE MATERIAL FOR  
ENHANCED SAFETY OF STEEL STRUCTURES**

**by**

**Qian Zhang**

A dissertation submitted in partial fulfillment  
of the requirements for the degree of  
Doctor of Philosophy  
(Civil Engineering)  
in The University of Michigan  
2015

Doctoral Committee:

Professor Victor C. Li, Chair

Assistant Professor Ann E. Jeffers

Professor Jerome P. Lynch

Professor Richard E. Robertson

© Qian Zhang

---

All rights reserved

2015

To my Dad and Mom,  
for their unconditional love and support

## ACKNOWLEDGEMENTS

Foremost I would like to thank my advisor Professor Victor C. Li for his continuous mentorship, encouragement and support during my PhD study. Without his dedication, I could never complete this research work. His valuable advice on both research and career development is of tremendous help to me and I am forever thankful for him.

I would like to thank my dissertation committee members, Professors Richard E. Robertson, Assistant Professor E. Ann Jeffers, and Professor Jerome P. Lynch for their insightful comments and encouragement.

I would like to extend my gratitude to our lab technicians: Bob Spence, Bob Fischer, Jan Pantolin, and Rick Burch, who have always been helpful with my experiments. Without their assistance, I couldn't finish the experimental work so smoothly. I would also like to thank the administrative staff of the Civil and Engineering Department: Jessica Taylor, Kimberly Simmons, Nancy Osugi, Matt Blank, Sherry Brueger, and Patricia Brainard for providing assistance in administrative matters.

I am also thankful to my colleagues and friends at the ACE-MRL lab. I would like to thank Dr. Ravi Ranade for his help with my experimental setup and being a fantastic co-author as well as a valuable friend. I would also like to thank Emily Herbert, Motohiro Ohno, Dr. Mo Li, Dr. Xiaoyan Huang, Dr. Jiangtao Yu, Dr. Burak Felekoglu, Dr. Aaron

Sakulich, Devki Desai, Danny Soltan, Zhigang Zhang, Hezhi Liu and many more for being great lab mates and co-works.

Finally, I would like to thank my parents and close friends. I could never be the person I am today without the love, support and sacrifices from my parents Jingping Zhang and Fange Lyu, for whom I dedicated this dissertation to. I am fortunate for having so many close friends around me. I am grateful for Shiming Duan, Luying Wang, Qianru Guo, Xiaohu Fan, Zhichao Liu, Yao Zhang, Dan Wei, Honghao Li, Zhijie Wang, and many more for their great friendship, which makes my life in Ann Arbor joyful.

## TABLE OF CONTENTS

DEDICATION .....	ii
ACKNOWLEDGEMENTS .....	iii
LIST OF TABLES .....	viii
LIST OF FIGURES .....	ix
ABSTRACT .....	xiv
CHAPTER 1 INTRODUCTION.....	1
1.1 BACKGROUND AND MOTIVATION .....	1
1.2 PROPOSED MATERIAL SOLUTIONS .....	4
1.3 RESEARCH APPROACH.....	8
1.3.1 Parallel Design.....	8
1.3.2 Material micromechanical Modeling.....	11
1.4 ORGANIZATION OF THIS DOCUMENT .....	13
CHAPTER 2 COMBINING LOW THERMAL CONDUCTIVITY WITH HIGH COHESION IN ECC .....	17
2.1 INTRODUCTION.....	17
2.2 EXPERIMENTAL PROGRAMS .....	19
2.2.1 Material Design Considerations .....	19
2.2.2 Mechanical Properties Characterization.....	23
2.2.3 Thermal property Characterization.....	24
2.2.4 Cohesive property under impact load .....	26
2.2.5 Wrapped-around durability study.....	27
2.3 EXPERIMENTAL RESULTS AND DISCUSSION.....	29
2.3.1 Mechanical properties.....	29
2.3.2 Thermal properties.....	32
2.3.3 Cohesive property under impact load.....	36
2.3.4 Wrapped-around durability.....	38

2.4 CONCLUSIONS.....	43
CHAPTER 3 DESIGN FOR HIGH ADHESION OF FR-ECC TO STEEL.....	48
3.1 INTRODUCTION.....	48
3.2 EXPERIMENTAL PROGRAMS .....	51
3.2.1 Material.....	51
3.2.2 Adhesion Characterization .....	52
3.2.3 Microstructure Investigation.....	55
3.2.4 Mechanical Property.....	55
3.3 RESULTS AND DISCUSSION .....	56
3.3.1 Adhesion Characterization .....	56
3.3.2 Microstructure Investigation.....	61
3.3.3 Mechanical Property.....	64
3.4 CONCLUSION .....	70
CHAPTER 4 DEVELOPMENT AND CHARACTERIZATION OF SPRAY- APPLIED FIRE-RESISTIVE ENGINEERED CEMENTITIOUS COMPOSITES .....	75
4.1 INTRODUCTION.....	75
4.2 EXPERIMENTAL PROCEDURES .....	78
4.2.1 Material design .....	78
4.2.2 Specimen preparation and testing.....	82
4.3 RESULTS AND DISCUSSION .....	85
4.3.1 Mechanical property of Cast Material .....	85
4.3.2 Sprayability characterization .....	90
4.3.3 Performance of sprayed material.....	91
4.4 CONCLUSION .....	98
CHAPTER 5 MICROSTRUCTURE AND MICROMECHANICS OF SFR-ECC....	101
5.1 INTRODUCTION.....	101
5.2 MICROMECHANICS UNDERLYING TENSILE BEHAVIOR .....	102
5.2.1 Experimental programs.....	102
5.2.2 Interpretation of the single fiber pull-out test data .....	107
5.2.3 Deduction of $\sigma(\delta)$ using scale linking .....	109
5.2.4 Results and discussion .....	110
5.3 MICROSTRUCTURAL INVESTIGATION ON COMPRESSIVE BEHAVIOR	125

5.3.1 Specimens and procedures.....	128
5.3.2 Results and discussions .....	128
5.4 SUMMARY AND CONCLUSIONS.....	134
CHAPTER 6 SFR-ECC UNDER HIGH RATE LOADING .....	139
6.1 INTRODUCTION.....	139
6.2 COMPOSITE MECHANICAL PROPERTY .....	140
6.2.1 Experimental procedures .....	140
6.2.2 Results and discussions .....	142
6.3 MICROMECHANICAL INVESTIGATION .....	146
6.3.1 Investigation procedure .....	146
6.3.2 Results and discussions .....	146
6.4 IMPACT RESISTANCE OF SFR-ECC AS COATINGS ON STEEL MEMBERS .....	155
6.4.1 Experimental procedure.....	155
6.4.2 Result and discussion.....	157
6.5 CONCLUSION .....	162
CHAPTER 7 CONCLUDING REMARKS .....	165
7.1 ACCOMPLISHMENT AND FINDINGS .....	165
7.1.1 Development and characterization of SFR-ECC.....	165
7.1.2 Material investigation .....	167
7.2 RESEARCH IMPACTS AND CONTRIBUTIONS.....	168
7.3 FUTURE RESEARCH DIRECTIONS.....	169
7.3.1 Structural scale investigations of SFR-ECC.....	169
7.3.2 SFR-ECC as energy absorption and protective material .....	170
7.3.3 Design for high temperature resistance .....	170



## LIST OF TABLES

Table 2.1 Physical property of glass bubbles and fly ash cenospheres .....	22
Table 2.2 Characteristics of PVA fiber.....	22
Table 2.3 Mix design of FR-ECC candidates .....	22
Table 2.4 Impact details of “durable wrap-around” test.....	29
Table 3.1 Mix proportion (by weight) of the adhesion test specimen .....	52
Table 4.1 Mix details of SFR-ECC.....	82
Table 5.1 Measured interfacial properties of SFR-ECC.....	113
Table 5.2 Input parameters for computing $\sigma(\delta)$ relationship .....	115
Table 6.1 Tensile property of SFR-ECC under various strain rates .....	144
Table 6.2 Observed average residual crack width of SFR-ECC under various strain rates .....	145
Table 6.3 Matrix toughness of SFR-ECC under various loading rates.....	147
Table 6.4 Measured fiber/matrix interfacial properties of SFR-ECC under various loading rates .....	148
Table 6.5 Calculated fiber bridging properties for SFR-ECC under various loading rates .....	149

## LIST OF FIGURES

Fig.1.1 Damage of SFRM (a) on the bottom flange of steel beam (the picture was taken from the ground looking up, showing one end of the beam going into the concrete block wall), and (b) on steel deck, under service condition.....	4
Fig.1.2 Strain hardening of ECC (a) typical stress-strain curve of ECC; (b) multiple cracking of ECC <sup>16</sup> .....	6
Fig.1.3 Interrelating design parameters for SFR-ECC.....	10
Fig.2.1 TGA curve of micro-sized hollow glass bubbles.....	21
Fig.2.2 SEM images of (a) glass bubbles and (b) fly ash cenospheres within the SFR-ECC mixtures.....	23
Fig.2.3 Uniaxial tensile test configurations for FR-ECC <sup>16</sup> .....	24
Fig.2.4 Apparent thermal conductivity test setup (ASTM E2584 <sup>18</sup> ).....	25
Fig.2.5 Drop weight tower impact test setup.....	27
Fig.2.6 Wrapped-around specimen configuration.....	28
Fig.2.7 High tensile strength and ductility attained in two FR-ECC mixes.....	31
Fig.2.8 Crack pattern of FR-ECC tensile specimens.....	31
Fig.2.9 Measured apparent thermal conductivity of FR-ECC and control SFRM.....	34
Fig.2.10 Measured apparent thermal conductivity of FR-ECC (Mix 1) during two consecutive heating/cooling cycles.....	35
Fig.2.11 Damage condition of (a) SFRM after 6 impacts; and (b) FR-ECC panel specimens after 12 impacts.....	38
Fig.2.12 Condition of SFRM protected steel beam before and after impacts.....	40

Fig.2.13 Condition of FR-ECC protected steel beam before and after impacts.....	41
Fig.2.14 Damage condition of FR-ECC protected steel beam after eccentric impact.....	42
Fig.3.1 Adhesion test <sup>4</sup>	
(a) specimen and load configuration, and (b) interface fracture model.....	53
Fig.3.2 Molding of multiple fire-resistive material / steel specimens .....	54
Fig.3.3 Example of the data analysis of an adhesion specimen of Mix 1	
(a) Point-based calculation of adhesion energy on the specimen; (b) Extraction of the adhesion energy from the slope of the curves.....	58
Fig.3.4 The adhesion energy of FR-ECC matrices to steel is significantly higher than that of SFRM / steel .....	58
Fig.3.5 The surface condition of peeled off steel strips from Mix 1, 2 and 4 is significantly different from that of control SFRM.....	60
Fig.3.6 SEM images of the interface (cementitious material side) of (a-b) Mix 1, (c-d) Mix 2, and (d-e) Mix 4.....	62
Fig.3.7 Compressive strength and dry density of Mix 1, 2 and 3 decrease with increase in latex bonding agent dosage.....	64
Fig.3.8 Uniaxial tensile stress-strain curves of Mix 1, 2 and 3, showing the drastic reduction in tensile ductility with increase in bonding agent dosage.....	66
Fig.3.9 Polystyrene beads used as artificial flaws .....	68
Fig.3.10 Recovery of tensile ductility of Mix 2 by the addition of artificial flaws.....	68
Fig.3.11 Crack pattern of Mix 2 modified with artificial flaws.....	69
Fig.3.12 Modified Mix 2 retains similar apparent thermal conductivity of unmodified FR-ECC (Mix 1).....	70

Fig.4.1 Vermiculites have irregular shape and porous structure .....	80
Fig.4.2 Vermiculite particle size gradation.....	80
Fig.4.3 Schematics of assembled single specimen for thermal conductivity test.....	84
Fig.4.4 Uniaxial tensile behavior of the cast Mix 1-3.....	86
Fig.4.5 Mix 2 and 3 with higher glass bubble content shows lower first crack strength...	86
Fig.4.6 Uniaxial tensile behavior of the cast Mix 4-5.....	88
Fig.4.7 Compressive stress-strain curve of SFR-ECC (Mix 2) indicating foam behavior	89
Fig.4.8 Direct spray test (a) shows that SFR-ECC can build up to 40-45mm for (b) Mix 2 and 60 mm for (c) Mix 5 in 2 sprays .....	91
Fig.4.9 Sprayed SFR-ECC maintains substantial ductility.....	92
Fig.4.10 Different multiple cracking behavior between cast specimens and sprayed specimens; (a) casted Mix 2; (b) sprayed Mix 2; (c) casted Mix 5; and (d) sprayed Mix 5.....	94
Fig.4.11 (a) Sprayed SFR-ECC (Mix 5) has less large flaws than (b) cast SFR-ECC specimen (Mix 5) .....	95
Fig.4.12 Comparable apparent thermal conductivity of SFR-ECC to SFRM .....	96
Fig.4.13 Fibers bridge across the interfacial crack between steel and SFR-ECC.....	97
Fig.4.14 Steel strips peeled off from SFR-ECC (a) Mix 2; (b) Mix 5.....	98
Fig.5.1 Matrix toughness test configuration .....	103
Fig.5.2 Single fiber pull-out test configuration (a) preparation of specimens, (b) test setup, and (c) specimen for inclined fiber.....	105
Fig.5.3 Single crack test configuration .....	106
Fig.5.4 Examples of different single fiber pull-out behaviors of SFR-ECC specimens..	111

Fig.5.5 SEM image of HTPP fibers pulled-out from SFR-ECC showing nonhomogeneous fiber/matrix interface .....	112
Fig.5.6 Deduction of the snubbing coefficient $f$ .....	114
Fig.5.7 SEM image showing bundled fibers and fibers within air pores in SFR-ECC ...	117
Fig.5.8 Computed fiber bridging curve using micromechanical model as comparison to testing curves from single crack test.....	118
Fig.5.9 SEM image of cracked surface of single crack specimen .....	119
Fig.5.10 Linear elastic and bilinear fiber constitutive models.....	121
Fig.5.11 Computed fiber bridging curve considering fiber stretching as comparison to the previous model.....	122
Fig.5.12 Effect of chemical bond on $\sigma(\delta)$ relationship of SFR-ECC .....	124
Fig.5.13 Typical compressive stress-strain relationship of SFR-ECC .....	125
Fig.5.14 Brittle and cellular-like fracture of brittle matrix foam material <sup>21</sup> .....	127
Fig.5.15 Cellular microstructure of SFR-ECC .....	130
Fig.5.16 Crack forms connecting air pores at plateau stage .....	131
Fig.5.17 Successive deformation SFR-ECC during the plateau stage under compression .....	132
Fig.5.18 Collapse of glass bubbles during densification .....	132
Fig.5.19 Microstructure of SFR-ECC at later stage of densification.....	132
Fig.5.20 Different compressive failure mode for (a) cube and (b) cylinder specimen of SFR-ECC matrix due to different confinement level .....	133
Fig.5.21 Densification of SFR-ECC composite under compression ( $\Phi 76 \times 152$ mm cylindrical specimen).....	134

Fig.6.1 SFR-ECC remains ductile under high rate loading .....	143
Fig.6.2 Crack pattern of SFR-ECC under different strain rates .....	144
Fig.6.3 Measured compressive strengths of SFR-ECC under various strain rates .....	145
Fig.6.4 Observed trend of first cracking strength and matrix fracture toughness of SFR-ECC.....	147
Fig.6.5 Computed $\sigma(\delta)$ curve of SFR-ECC under various loading rates .....	150
Fig.6.6 Comparison between calculated fiber bridging strength and measured composite ultimate tensile strength of SFR-ECC.....	151
Fig.6.7 Trend for $\sigma_0 / K_m$ and $\delta_{avg}$ under increasing displacement rates .....	153
Fig.6.8 The influence of chemical bond on computed (a) fiber bridging strength; (b) crack width.....	154
Fig.6.9 Condition of conventional SFRM protected steel panel after impacts (a) Final condition of the steel panel; (b) Delaminated SFRM; (c) The thickness of residual SFRM on the steel panel after impacts as comparison to (d) The original thickness of the SFRM on the steel panel.....	158
Fig.6.10 Condition of SFR-ECC protected steel panel (with surface bonding agent) after impacts (a) Crack pattern on the top surface; (b) Close-up view of the cracks .....	159
Fig.6.11 Cracking on the bottom surface of the SFR-ECC in SFR-ECC protected steel panel specimen (without surface bonding agent) (a) Crack pattern; (b) Close-up view of the fine cracks.....	160
Fig.6.12 Conditions of protected beams after impacts (a) SFR-ECC protected beam; (b) SFRM protected beam to impacts.....	162

## **ABSTRACT**

Although spray-applied fire-resistive materials (SFRM) are the most commonly used passive fire protection for steel structures, its performance is often called into question due to their unsatisfactory durability performance. The inherent brittleness, low strength and poor bond with steel lead to delamination and partial loss of fire protection even under service loads, significantly lowering the structural fire resistance. This could be further exaggerated under multi-hazards, such as post-earthquake and post-impact fires, greatly endangering the fire safety of steel structures.

To address this critical issue, a new ductile cementitious SFRM, namely spray-applied fire-resistive engineered cementitious composite (SFR-ECC), has been developed that overcomes the aforementioned problem. Following a parallel design process, SFR-ECC has been developed to satisfy multiple performance targets in one material, including low thermal conductivity, high tensile ductility, high adhesion to steel and sprayability. The resultant material possesses tensile strength, strain capacity, interfacial adhesive energy of 1-2 orders of magnitude higher than the conventional SFRM, yet possesses similar thermal conductivity and sprayability, providing a durable alternative to conventional SFRM. SFR-ECC is also found to exhibit ductile cellular behavior under compression, further enhancing its energy absorption capacity.

The micromechanical and microstructural mechanisms underlying the unique tensile and compressive behavior of SFR-ECC are studied. The material macro- and micro-mechanical behavior under high loading rates have also been investigated. SFR-ECC is found to maintain high tensile ductility under high rate loadings, ensuring its performance under earthquake and impact loads.



# **CHAPTER 1 INTRODUCTION**

## **1.1 BACKGROUND AND MOTIVATION**

Steel structure is vulnerable under fire hazard. Steel loses its stiffness and strength rapidly when subjected to high temperature. As an illustration, unprotected steel structural members (e.g. columns and beams) fail in about 20 minute under standard fire conditions.<sup>1</sup> However, building codes mandate fire resistance ratings of 2 to 4 hours for typical steel structural members to ensure adequate evacuation time. To satisfy this requirement, the current practice is to apply external insulation (fire protection) to limit the temperature rise in steel, so as to ensure structural stability under fire conditions.

Commonly used insulation materials include insulation boards, intumescent paint and spray-applied fire-resistive materials (SFRM). They all have very low thermal conductivity, therefore delay the temperature rise in the steel structures and prevent fire induced structural failures.

Insulation boards are slab-like gypsum or calcium silicate elements that are attached to wood/metal frame and then attached to the steel members. Insulation boards can achieve high fire rating up to 4 hrs. However, the installation time of these boards are relatively long. It is also difficult to apply insulation boards to irregular shaped members.

Intumescent paint is another major type of fire protection material. It is painted onto the steel members. Under heat, the material swells and forms a char. The thickness of the char is

typically 15-30 times that of the original paint. The char is very porous and has very low thermal conductivity, therefore protects the steel structure against fire. However, intumescent paints have relatively lower fire ratings, typically limited to 2 hrs. It is also most expensive compared to the other two types of fire protection material. When higher fire rating is required, the cost could be prohibitively high. For example, for a W10x49 beam of 20 ft long to achieve 2-hr fire rating, the total cost (including installation) of using intumescent paint is about 16-20 USD/ft<sup>2</sup>. For the same beam to achieve 3-hr fire rating, the price is increased to about 33-40 USD/ft<sup>2</sup>. This could be 10 times higher than the cost of using SFRM. (The cost is obtained through private communications with local contractors in Michigan, US.). The high cost substantially limits the application of intumescent in the construction industry in US.

Spray-applied fire-resistive materials (SFRM) are typically lightweight plasters made of cementitious (gypsum or Portland cement) binders and inorganic porous aggregates (perlite, vermiculite, etc.) or mineral wools. Among those, cementitious SFRMs are more commonly used; many of which are Portland cement based. SFRM are applied by spraying onto the steel structures during constructions. SFRM have very low thermal conductivity due to their extreme porous structure which lends them excellent fire resistance. SFRM can achieve fire rating up to 4 hrs. SFRM are applied through spraying process, which significantly shortens the installation time and therefore lowers the cost. It also allows SFRM to cover detailed features easily, like bolts and connections. Most importantly, SFRM are very cost effective compared to other fire protection materials, particularly intumescent paints, which makes them extensively used in US.<sup>2</sup>

Although SFRM are widely used for steel structures in US, the performance of SFRM is often called into questions due to their poor durability.<sup>3</sup> The term durability (in the context of fire protection materials) mainly refers to the ability of SFRM to stay on the steel substrate, which is

often found to be insufficient even under service loads due to their brittleness, low tensile strength and poor bond with steel. For example, impacts and vibrations caused by regular mechanical or electrical maintenance work could easily delaminate the existing SFRM. For example, **Fig.1.1** are the documented photos showing the delamination of SFRM during regular service condition due to interruptions from regular maintenance work (Cambrian College, ON, Canada, 2000). Failure to restore the SFRM could lead to reduced fire resistance of the structure. This problem is further exacerbated under extreme loading conditions such as earthquakes and impacts. The collapse of WTC twin towers, which was partly attributed to damaged fire protection, has brought wide attention on this issue. Experimental studies and computational analysis<sup>4,5,6</sup> demonstrated that SFRM could debond and fall off when the steel substrate experiences large deformation or when subjected to impact loads. Tests and analysis also revealed that even minor losses of SFRM in a steel member cause significant increase of temperature when fire occurs.<sup>7,8,9,10</sup> This leads to a reduction in fire resistance of structural members that could result in failure of the structural system. Therefore the poor durability of SFRM greatly endangers the steel structures under fire hazards.

It is recognized that there is an urgent need for improving the durability characteristics of the SFRM and developing more durable fire protection materials. The FEMA/ASCE WTC investigation report, as well as the NIST report, both recommended that fireproofing be tested for durability. NIST has also developed a series of experimental procedures to better characterize the performance of SFRM which includes characterization of durability properties.<sup>11</sup> Recent IBC code also increased the bonding requirement for fireproofing materials applied to high rise buildings.

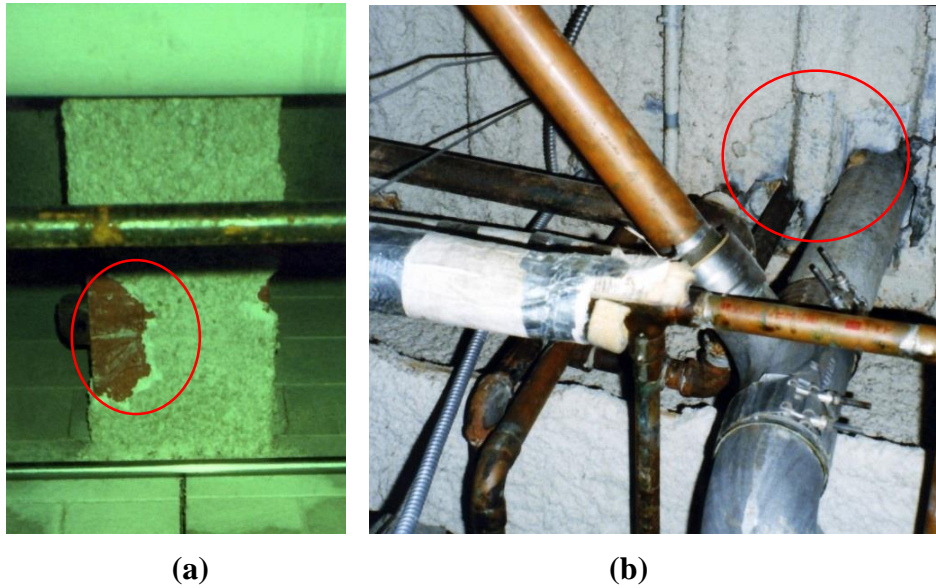


**Fig.1.1 Damage of SFRM (a) on the bottom flange of steel beam (the picture was taken from the ground looking up, showing one end of the beam going into the concrete block wall), and (b) on steel deck, under service condition<sup>12</sup>**

Despite the urgent needs and more stringent requirement, there has been no real breakthroughs from the material engineering side. There has been no research done to systematically study the material engineering of more durable SFRM. Recognizing the knowledge gap and urgent research need, this doctoral dissertation focuses on development of a new generation of durable SFRM through a systematic material engineering approach. The new generation of SFRM with superior durability performance will therefore substantially enhance the fire safety of the steel structures.

## **1.2 PROPOSED MATERIAL SOLUTIONS**

Durability of SFRM mainly include two major parts: adhesion and cohesion. Adhesion refers to the resistance to interfacial fracture/failure between SFRM and steel substrate, which sometimes could be enhanced through steel surface treatment or applying external bonding adhesives on the interface. Cohesion refers to the resistance to fracture/failure (e.g. delamination, cracking) within SFRM themselves, which is intrinsically associated with SFRM's own

mechanical property. However, conventional SFRM have very poor mechanical performance. The tensile strength of a common medium density (352-480 kg/m<sup>3</sup>) SFRM material is below 0.1 MPa,<sup>13</sup> and the fracture toughness of SFRM has not been reported, but is expected to be substantially less than normal concrete, i.e. less than  $0.2 \text{ MPa} \cdot \sqrt{\text{m}}$ . Because SFRM are often loaded via imposed displacement (e.g. due to displacement of the structural steel substrate), another important tensile property of SFRM is the tensile strain capacity. Although there is no documented tensile strain capacity data in the literature, the tensile ductility is expected to be comparable to or less than that of normal concrete material (approximately 0.01%, which is low). For such material, the durability mainly relies on the interfacial adhesion to keep SFRM on the steel substrate. However, the interfacial adhesion is often found to be insufficient as well. In addition, even with high interfacial adhesion, the delamination due to poor cohesion could also result in reduction of the effective thickness, which significantly reduces the fire resistance. The inherently low cohesive strength greatly limits the durability performance of the conventional SFRM.

In order to fundamentally overcome the durability challenges for conventional SFRM, a new generation of durable fire protection material called Spray-applied Fire-resistive Engineered Cementitious Composites (SFR-ECC) is proposed in this doctoral research adopting ECC technology. ECC is a special family of ultra-ductile high performance fiber reinforced cementitious composites.<sup>14,15</sup> Under tensile load, ECC develops multiple micro-cracks instead of one large crack, and the load carrying capacity continues to increase after first crack achieving pseudo strain-hardening behavior, as illustrated in **Fig.1.2**. The tensile strain capacity of ECC typically reaches 3-5%, which are about 300-500 times that of conventional concrete material,<sup>16</sup> while the crack width is typically controlled to be under 100  $\mu\text{m}$ . The highly ductile behavior of

ECC results in substantially higher fracture resistance and damage tolerance. Therefore, ECC is of inherently high cohesion.

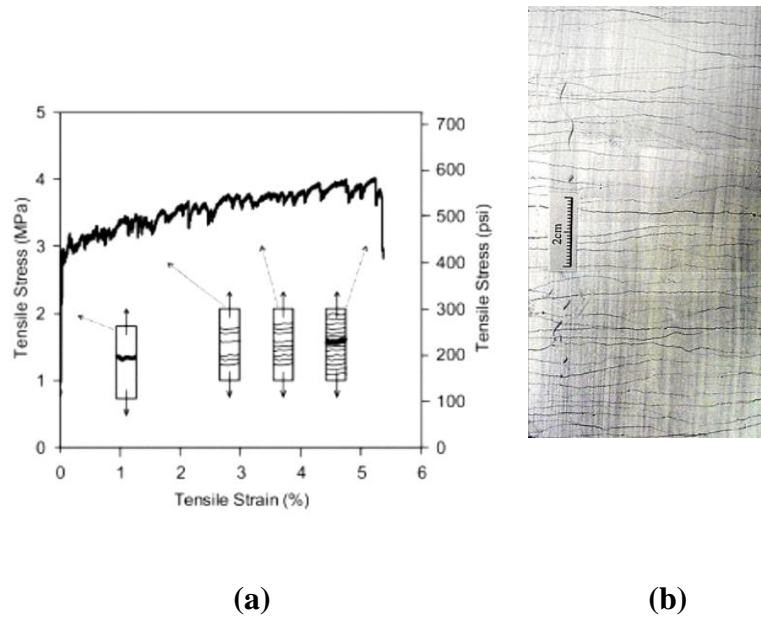


**Fig.1.2 Strain hardening of ECC**  
**(a) typical stress-strain curve of ECC;<sup>17</sup> (b) multiple cracking of ECC<sup>16</sup>**

As previously discussed, cohesion is an intrinsic material property, while adhesion is interfacial property and sometimes can be modified externally. Adopting the ECC technology is expected to introduce inherent high cohesive property into the proposed SFR-ECC and therefore significantly improve the durability characteristics of SFRM.

In addition, ECC is a designable material with a theoretical basis. ECC is designed based on micromechanics theory, which will be discussed in details in **1.3.2**. Tailoring of the material composition under the guideline of ECC design theory resulted in many new materials that exhibit different functions within the ECC family. For example, lightweight ECC<sup>18</sup>, sprayable ECC<sup>19</sup>, and self-consolidating ECC<sup>20</sup>, etc. have been developed successfully in previous researches. This also

demonstrates the plausibility of combining other necessary functions with high cohesive strength in the proposed SFR-ECC.

Apart from the high cohesion requirements, the new material should also possess high interfacial adhesion and essential functionality properties that qualifies it as a SFRM, namely low thermal conductivity and sprayability. Summarizing all the target performance, the newly developed material needs to possess properties in the following aspects:

- (a) high cohesion (mechanical property);
- (b) strong adhesion to the steel substrate;
- (c) low thermal conductivity and
- (d) suitable fresh property for sprayability.

It is worth pointing out that ECC typically uses polymer fibers with low melting temperature as reinforcement. Although the fibers melt at high temperature (e.g. above 200 °C), it has been found that ECC typically possesses very similar or even higher residual compressive strength than that of conventional cementitious material. This is partly associated with the effect that the melting polymer fibers create connected channel to release the internal vapor pressure, which prevents spalling under high temperature.<sup>21,22</sup> Regarding the tensile properties, a number of previous researches<sup>23,24,25</sup> have found that ECC generally experiences reduction in tensile ductility under elevated temperature. After the polymer fibers completely melt, ECC behaves similarly to normal brittle cementitious material.

The present doctoral research focuses on enhancing the fire safety of steel structures by improving the durability of the SFRM at ambient temperature, therefore, the adoption of ECC technology that employs polymer fibers are plausible. As previously indicated, the main concern

with conventional SFRM is that they tend to dislodge and delaminate under severe loading conditions as well as under service loads, which mostly happen under ambient temperature. For example, for post-earthquake/impact fires, the earthquakes or impacts typically happen before the fire event and under ambient temperature. The problem is that when the fire occurs, the SFRM has already been lost during the events at ambient temperature and therefore could not provide sufficient fire protection to the steel structure. However, if the SFRM are well preserved when the fire occurs, based on the fire resistance tests (conducted by SFRM manufacturers) and past experience, the conventional SFRM are able to effectively protect the steel structures. Therefore the durability of SFRM under ambient temperature rather than under high temperature is considered critical and needs to be enhanced most urgently. As a result, the proposed SFR-ECC with enhanced durability at ambient temperature and similar performance (both thermally and mechanically) under elevated temperature compared to conventional SFRM will greatly contribute to enhance the overall fire safety of steel structures.

### **1.3 RESEARCH APPROACH**

The material design will be performed following a parallel design methodology to achieve multiple design targets simultaneously. Micromechanical modeling and characterization will also be used in the design for high tensile ductility and further investigation of the developed material.

#### **1.3.1 Parallel Design**

As previously discussed, SFR-ECC material design involves simultaneous tailoring of the material for multiple performance targets in one mixture. The design targets can be grouped into two major categories: enhanced durability properties and proper functionality properties. Durability properties refer to cohesive and adhesive properties, which mainly include to tensile



strength, tensile ductility and interfacial adhesion to steel for SFR-ECC. Functionality properties refer to those required to ensure proper functional performance of SFR-ECC as a spray-applied fire-resistive material, which mainly include thermal conductivity and sprayability.

The design process of SFR-ECC must consider potential conflicting requirements for each individual design target. Designing for low thermal conductivity requires tailoring the microstructure of the material to possess high air void content and small air void size. This can be achieved by using porous or hollow lightweight aggregates in the mixture. Designing for tensile ductility requires tailoring the fiber, matrix, and fiber/matrix interfacial micromechanical parameter of the mixture according to micromechanics including keeping the matrix toughness low and controlling the interfacial bond property between fiber and matrix for maximum bridging force but with minimum breakage. This will be discussed in details in **1.3.2**. Designing for high adhesion (to steel) involves modifying the cementitious material/steel interfacial transition zone and often requires adding polymeric admixtures into the mixture that might have side-effects on rheological and micromechanical characteristics. Designing for sprayability involves controlling the rheology of the mixture. This is often achieved by controlling the water content, chemical admixtures, aggregate absorption and geometry, using water holding and non-abrasive aggregates, and properly selecting the fiber content and geometry.

Due to the above interrelations, there are also potential conflicts between individual design procedures. For example, to achieve proper sprayability, relatively low fiber content and shorter fibers are preferred to avoid excessive fiber clumping during the pumping and spraying process. However, this is often not favorable for achieving high tensile ductility. Another example would be that using polymeric latex in the mixture (in favor of high adhesive property) could lead to air entrainment, which could lower the strength of SFR-ECC. In addition, the polymeric latex also

could alter the interfacial bond property of SFR-ECC, which might have complicated influence on the tensile behavior.

To simultaneously attain the desired fresh property and mechanical and thermal properties of SFR-ECC, the interdependencies and potential conflicts highlighted above need to be taken into account in the design procedure. The design targets and corresponding design parameters of SFR-ECC are presented in **Fig.1.3**.

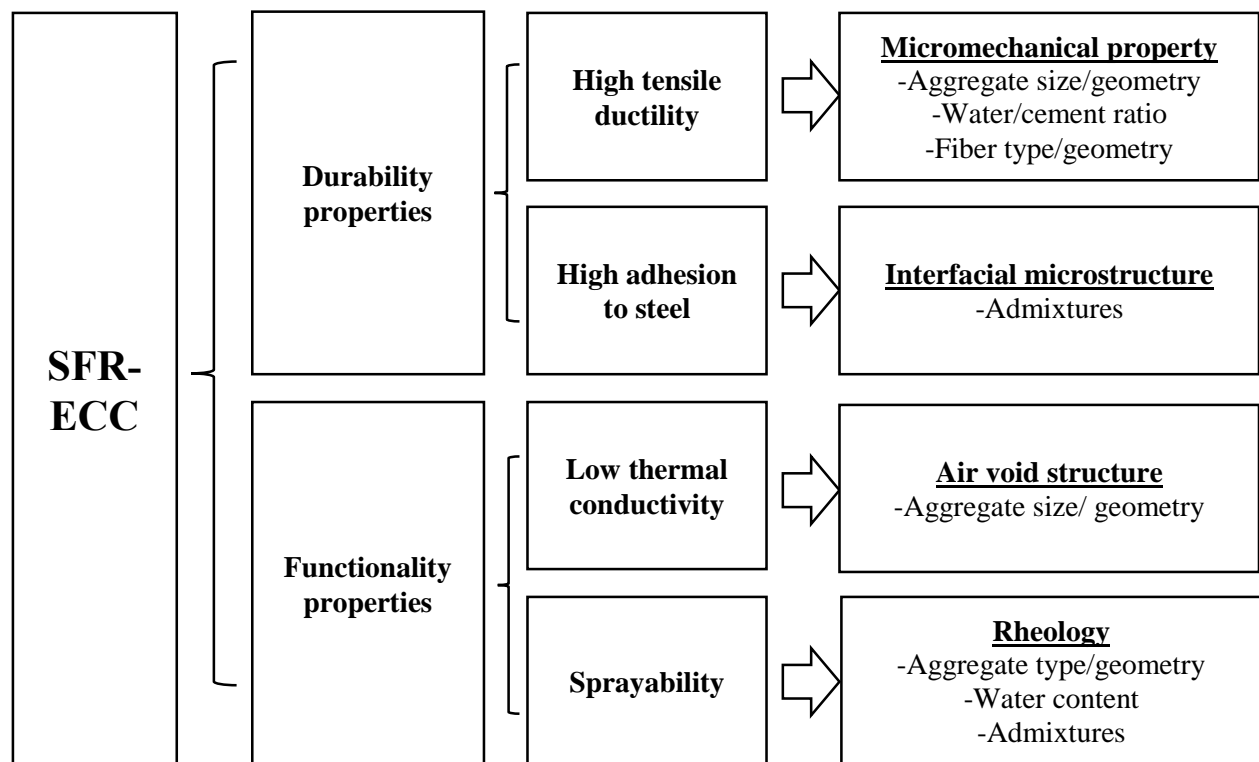


**Fig.1.3 Interrelating design parameters for SFR-ECC**

To better handle the design conflicts and interrelations, a parallel design procedure will be used in this dissertation. During the parallel design process, design for individual targets, which includes the tailoring of micromechanical properties, interfacial microstructure, air void structure, and rheology are conducted at the same time. When selecting the design parameters for one individual design target, for example, design for thermal conductivity, the design parameters need

to be selected such that the adverse effect on other target performance is minimized or can be compensated.

The parallel design process requires thorough knowledge of the individual design process and their interrelations. Therefore, prior to the parallel design process, each individual design process and their interdependencies need to be studied carefully.

### 1.3.2 Material micromechanical Modeling

Micromechanics modeling will also be extensively used in this doctoral research, both as guideline in the design process for high tensile ductility (cohesion) and for modeling the material behavior under various conditions (different loading rate).

Micromechanical modeling links micro-scale constituent parameters (fiber, matrix and fiber/matrix interface) to fiber bridging constitutive behavior and steady state crack analysis, connects fiber bridging property to multiple cracking behavior and thus tensile strain hardening behavior in the composite scale. Together they provide a link from the microstructure and micromechanical properties to the macro-scale mechanical properties. Also, such link can be used backwards for material microstructure/composition tailoring so as to achieve desirable composite properties.

The core of the micromechanics-based ECC theory is the strain-hardening criteria, which refer to the energy and strength balance that need to be satisfied within the composites. The criteria are stated as follows:

$$\text{Energy based criterion: } J_{tip} \leq \sigma_0 \delta_0 - \int_0^{\delta_0} \sigma(\delta) d\delta \equiv J'_b \quad (1.1)$$

$$\text{Strength based criterion: } \sigma_0 > \sigma_{cs} \quad (1.2)$$

where  $\sigma_0$  is the maximum bridging stress corresponding to the crack opening  $\delta_0$ ;  $\sigma_{cs}$  is the cracking strength of the matrix;  $J_{ip}$  is the fracture energy of the matrix, which is approximately equal to  $\frac{K_m^2}{E_m}$ , where  $K_m$  is the matrix fracture toughness, and  $E_m$  is the matrix Young's modulus.

**Eq.1.1** describes the energy balance in the crack extension process. Failure to meet this criterion results in the Griffith crack mode with unrestricted crack width as the crack extends.<sup>26</sup> The composite ingredients should be tailored to achieve sufficient margin between complimentary energy of fiber bridging  $J'_b$  and crack tip toughness  $J_{ip}$  to enable saturated multiple cracking and robust tensile ductility.<sup>27</sup> This requires limiting the matrix fracture toughness (that limits  $J_{ip}$ ) and/or increasing the  $J'_b$  by adjusting fiber properties (volume fraction, length, diameter, tensile strength and modulus) and fiber/matrix interfacial properties (fiber/matrix frictional and chemical bonds). **Eq.1.2** describes the strength criterion of multiple cracking, which requires the fiber bridging strength to be higher than the matrix cracking strength that is a function of the matrix defect size. If either inequality (**Eq.1.1** or **1.2**) is not satisfied, the composite fails with a single localized fracture, instead of multiple cracking, and a typical tension-softening behavior of normal fiber reinforced concrete is observed.

The above micromechanical theory can be used to tailor the composite for desired tensile property. However, as discussed in **1.3.1**, micromechanical parameters are not always designable. Certain performance requirements, in this case, thermal insulation property, sprayability, and good cohesion/adhesion performance may involve modification of the microstructure and therefore micromechanical properties of the mixture, and make some of the micromechanical properties less

flexible. Therefore design constraints are posed. Then other parameters need to be tailored carefully to recover the superior mechanical properties.

In addition to material design, micromechanics based model will also be extensively used in this doctoral research to model and understand the behavior of SFR-ECC under high rate loading and elevated temperature.

## **1.4 ORGANIZATION OF THIS DOCUMENT**

This doctoral dissertation has been organized into seven chapters. The first chapter introduces background and motivations of this research. Proposed material solutions and research approach are also introduced in the first chapter.

Chapter 2-4 covers the material development of SFR-ECC. In Chapter 2, preliminary mix designs of SFR-ECC that combines the thermal insulating property of SFRM and high cohesive property ECC are presented. An effective material engineering approach for achieving low thermal conductivity is therefore demonstrated. The correlation between high cohesive property and better durability performance of SFR-ECC is experimentally verified via low velocity impact test on SFRM/SFR-ECC protected steel members. This chapter demonstrates the feasibility and validity of the proposed research and lays the foundation for further development of SFR-ECC. In Chapter 3, a complete study on design for high adhesion of SFR-ECC (to steel) is presented. Chapter 3 investigates material engineering techniques for achieving high adhesion and the mechanisms behind the improvement. This chapter also studies the interrelations between the design for high adhesion and the design for high tensile ductility (cohesion), which provides valuable input to the parallel design process in Chapter 4. Based on the findings described in Chapter 2 and 3, parallel design and material characterization of SFR-ECC were conducted, and the results are documented

in Chapter 4. In Chapter 4, SFR-ECC that exhibits enhanced durability characteristics (high cohesion and adhesion to steel) and suitable functionality properties (low thermal conductivity and acceptable sprayability) has been developed.

Chapter 5 and 6 documents findings of research that provide insights into the behavior and failure mechanisms of SFR-ECC under both static and high rate loading. These findings provide fundamental knowledge for further study/application of SFR-ECC in structural configurations. In Chapter 5, the unique micromechanical and microscopic behavior of SFR-ECC that resulted in the macro-scale behavior of SFR-ECC are investigated. Chapter 6 documents the study on the durability (mechanical) properties of SFR-ECC under high rate loading and the underlying micromechanical mechanisms. SFR-ECC is shown to maintain its desirable tensile performance under high rate loadings due to relatively insensitivity of its micromechanical properties to loading rate. This ensures high durability of SFR-ECC under impact and earthquake load.

Chapter 7 is the conclusion chapter which summaries the major findings of this doctoral research and its broader impacts. Conclusions in relation to the research objectives are drawn. In addition, future research directions are also identified in this chapter.

## References

---

1. Milke, J., Kodur, V., Marrion, C., "Overview of Fire Protection in Buildings", FEMA (2002). World Trade Center Building Performance Study, Federal Emergency Management Agency (FEMA). Federal Insurance and Mitigation Administration, Washington, DC.
2. Fire protection of structural steel in high-rise buildings. Goode MG (ed.). NIST GCR 04-872, 2004.
3. NIST NCSTAR (2005). "Collapse of the World Trade Center Towers. Final Report. Federal Building and Fire Safety Investigation of the World Trade Center Disaster." National Institute of Standards and Technology; National Construction Safety Team, 208
4. Leo Braxtan, N., Pessiki, S., "Bond performance of SFRM on steel plates subjected to tensile yielding. Journal of Fire Protection Engineering," 2010; 21(1), 37-55.
5. Braxtan, N. L. and Pessiki, S. P., "Post-earthquake fire performance of sprayed fire-resistive material on steel moment frames. Journal of Structural Engineering," 2011; 137(9), 946-953.
6. Dwaikat, M., & Kodur, V., "Modeling fracture and delamination of spray-applied fire-resisting materials under static and impact loads," Journal of Engineering Mechanics, 2011; 137(12), 901-910.
7. Gu, L. and Kodur, V., "Role of insulation effectiveness on fire resistance of steel structures under extreme loading events," Journal of Performance of Constructed Facilities, 2010; 25(4), 277-286.
8. Keller, W. J. and Pessiki, S. "Effect of earthquake-induced damage to spray-applied fire-resistive insulation on the response of steel moment-frame beam-column connections during fire exposure," Journal of Fire Protection Engineering, 2012; 22(4), 271-299.
9. Tomecek, D. V. and Milke, J. A., "A study of the effect of partial loss of protection on the fire resistance of steel columns," Fire Technology, 1993; 29(1), 3-21.
10. Wang, W. Y. and Li, G. Q., "Behavior of steel columns in a fire with partial damage to fire protection," Journal of constructional steel research, 2009; 65(6), 1392-1400.
11. Tan, K. T., White, C. C., and Hunston, D. L., "An adhesion test method for spray-applied fire-resistive materials," Fire and Materials, 2011; 35(4), 245-259.
12. Achim Hering, "Fireproofing delamination", photo, Wiki Commons, Jun.30, 2007, Creative Commons License  
[http://commons.wikimedia.org/wiki/File:Fireproofing\\_delam\\_1.jpg](http://commons.wikimedia.org/wiki/File:Fireproofing_delam_1.jpg)  
[http://commons.wikimedia.org/wiki/File:Fireproofing\\_delam\\_2.jpg](http://commons.wikimedia.org/wiki/File:Fireproofing_delam_2.jpg)
13. Carino, N. J.; Starnes, M. A.; Gross, J. L.; duYang, J. C.; Kukuck, S. R.; Prasad, K. R.; Bukowski, R. W.; "Passive Fire Protection". In Federal Building and Fire Safety Investigation of the World Trade Center Disaster NIST NCSTAR 1-6A, 2005
14. Li, V. C., "On engineered cementitious composites (ECC)," Journal of advanced concrete technology, 2003; 1(3), 215-230.
15. Li., V. C., "Reflections on the research and development of engineered cementitious composites (ECC)," In Proceedings of the JCI International Workshop on Ductile Fiber Reinforced Cementitious Composites (DFRCC)—Application and Evaluation, 2002; 1-21.
16. Li, V. C., Wang, S., and Wu, C., "Tensile strain-hardening behavior of polyvinyl alcohol engineered cementitious composite (PVA-ECC)," ACI Materials Journal, 2001; 98(6), 483-492.

- 
17. Yang, E.H., Y. Yang, and V.C. Li, "Use of High Volumes of Fly Ash to Improve ECC Mechanical Properties and Material Greenness," *ACI Materials J.*, 2007; 104 (6), 620-628.
  18. Wang, S. and V. C. Li, "Lightweight ECC", HPCFRCC-4, Ann Arbor, MI, USA, 2003; 379-390.
  19. Kim, Y.Y., H.J. Kong and V.C. Li, "Design of Engineered Cementitious Composite (ECC) Suitable for Wet-mix Shotcreting," *ACI Materials J.*, 2003; 100 (6), 511-518.
  20. Kong, H. J., S. Bike, and V.C. Li, "Development of a Self-Consolidating Engineered Cementitious Composite Employing Electrosteric Dispersion/Stabilization," *J. Cement and Concrete Composites*, 2003; 25 (3), 301-309.
  21. Sahmaran, M., M. Lachemi, and V.C. Li, "Assessing the Mechanical Properties and Microstructure of Fire-Damaged Engineered Cementitious Composites", *ACI Materials J.*, 2010; 107 (3), 297-304.
  22. Sahmaran, M., Ozbay, E., Yucel, H.E., Lachemi, M., and V.C. Li, "Effect of Fly Ash and PVA Fiber on Microstructural Damage and Residual Properties of Engineered Cementitious Composites Exposed to High Temperatures," *J. of Materials in Civil Engineering*, 2011; 23(12), 1735-1745.
  23. Magalhães, M. S., R. D. Toledo Filho, and E. M. R. Fairbairn., "Physical and mechanical properties of strain-hardening cement-based composites (SHCC) after exposure to elevated temperatures." *International Conference on Advanced Concrete Materials*, Stellenbosch, South Africa, Nov. 17-19, 2009; 203-207.
  24. Mechtcherine, V., de Andrade Silva, F., Müller, S., Jun, P., & Toledo Filho, R. D., "Coupled strain rate and temperature effects on the tensile behavior of strain-hardening cement-based composites (SHCC) with PVA fibers." *Cement and Concrete Research*, 2012; 42(11), 1417-1427.
  25. Bhat, Prakash S., Vivian Chang, and Mo Li. "Effect of elevated temperature on strain-hardening engineered cementitious composites." *Construction and Building Materials*, 2014; 69, 370-380.
  26. Griffith, A. A., "The Phenomena of Rupture and Flow in Solids," *Philosophical Transactions of the Royal Society of London*, 1921; 221, 163–198.
  27. Kanda, T. and Li, V. C., "Multiple Cracking Sequence and Saturation in Fiber Reinforced Cementitious Composites," *JCI Concrete Research and Technology*, 9(2), 19-33, 1998.



## **CHAPTER 2      COMBINING LOW THERMAL CONDUCTIVITY WITH HIGH COHESION IN ECC**

This chapter documents the feasibility research that validates the proposed idea of enhancing the durability performance of conventional SFRM by incorporating ECC technology.

### **2.1 INTRODUCTION**

There are two main objectives of this feasibility research. The first objective is to develop preliminary SFR-ECC mixtures. This preliminary mixture needs to possess the most essential properties of the proposed SFR-ECC material. The second objective is to validate that the high cohesion of the preliminary SFR-ECC contributes to enhanced durability of the steel fire protection. This involves testing of SFR-ECC protected steel members and evaluating their durability performance in comparison to that of conventional SFRM.

Among all the target performance of SFR-ECC (high cohesion, strong adhesion to steel, low thermal conductivity and sprayability) identified in Chapter 1, the most essential requirements for SFR-ECC are high cohesion and low thermal conductivity. Cohesion mainly refers to the resistance to delamination and damage within the material itself which is closely associated with the material's mechanical property, mainly including strength and ductility of the material. Regarding SFR-ECC, ductility might be more important, since SFR-ECC is often loaded via deformation of the steel substrate. Adhesive property reflects the interfacial microstructure between SFR-ECC and structural steel. This sometimes can be modified through surface treatment

or applying external interfacial bonding adhesives. Sprayability offers versatility and ease for construction. However, even without sprayability, SFR-ECC could be applied in other ways, for example, troweling or casting. On the other hand, cohesion and thermal conductivity are inherent material properties, which cannot be modified externally, yet they are the essential target performance for the proposed material. Therefore, in this chapter, the material design for the preliminary SFR-ECC aims at combining the high cohesive property and low thermal conductivity.

In this chapter, two preliminary mix designs of SFR-ECC are presented developed with two different types of lightweight aggregates. Since the preliminary mixtures do not possess sprayability, they are denoted as fire-resistive ECC (FR-ECC) in this chapter. The thermal conductivity of FR-ECC is characterized in accordance with the test procedures of ASTM E2584<sup>1</sup>. The cohesive (mechanical) behavior of FR-ECC is characterized by direct uniaxial tension and compression tests. Low velocity impact tests are carried out on SFR-ECC coated steel panels to evaluate the durability of the material under impact load. In addition, because of the high cohesive strength and damage tolerance of ECC, a new durability concept “wrapped-around durability” is introduced. “Wrapped-around durability” refers to fully wrapping a highly ductile and strong insulation material around a steel member. The integrity of this fire-protection system relies solely on the cohesion property of the insulation material with almost no dependence on the adhesion between the insulation material and steel substrate. In this study, validity of this concept is demonstrated by low velocity impact tests. Test results and findings are documented in this chapter.

## 2.2 EXPERIMENTAL PROGRAMS

### 2.2.1 Material Design Considerations

In this chapter, the objective of the material design of FR-ECC is to achieve good insulation property and ductile mechanical performance (strain capacity >2%) simultaneously in one material for the targeted application. The desired thermal insulating property of FR-ECC is very low thermal conductivity of the material, similar to or less than that of conventional SFRM, so that it delays temperature rise of steel under fire. Typical thermal conductivity of a conventional SFRM is 0.05-0.32 W/(m K) within the temperature range of 20-650°C measured in the authors' laboratory in accordance with ASTM E2584<sup>1</sup>. Such low thermal conductivity is typically achieved by using lightweight aggregates and air entrainment within the material. Without any modification, the thermal conductivity of a frequently studied ECC (M45) is 0.15-0.63 W/(m K) within the same temperature range. In addition to low thermal conductivity, ductile mechanical performance of FR-ECC, e.g. tensile strain capacity greater than 2%, is required which is achieved by following the micromechanics based design principles.<sup>2,3</sup>

Thermal conductivity is closely associated with the microstructure, particularly pore structure, of the material. It is known that the thermal conductivity decreases with increase in total porosity of the material<sup>4,5,6,7,8,9</sup> due to the fact that air has significantly lower thermal conductivity compared to solid and liquid phases. As the total porosity is closely related to bulk density, the thermal conductivity of concrete often decreases with decrease in bulk density.<sup>10,11,12</sup> In addition to porosity, pore size distribution is also important for high temperature applications.<sup>8,9,13</sup> Heat transfer theory predicts that the equivalent thermal conductivity of a pore due to radiation is proportional to pore size. The apparent thermal conductivity equals the sum of true conductivity

due to conduction through the solid and equivalent conductivity due to radiation across the voids. Hence, to attain low thermal conductivity at high temperature, it is desirable to have high porosity and small pore size.

To reach the targeted low thermal conductivity in cementitious insulation materials, a widely used technique is to add lightweight porous aggregates, such as expanded perlite and vermiculite, in the matrix. For choosing a suitable lightweight aggregate for FR-ECC with the desired composite properties, the following considerations are important: (1) air void size inside the aggregate is minimized to reduce the radiation heat transfer effect; (2) aggregate size is preferably smaller than 1 mm and with smooth-shape to reduce adverse effects on the mechanical performance of ECC. The second consideration is based on the ECC design theory, which has been discussed in Chapter 1. In order to achieve high tensile ductility, the fracture toughness of the matrix needs to be kept low, therefore, coarse and irregular-shaped aggregates are not preferred.

In a previous study<sup>14</sup>, micron-sized hollow glass bubbles (GB) were successfully used to produce lightweight ECC material with mechanical properties (compressive strength and tensile ductility) suitable for structural applications. The average size of these micro glass bubbles is 20-40 microns. Unlike other angular lightweight aggregates, these tiny spherical glass bubbles have less resistance to crack propagation thus lowering the matrix fracture toughness. In addition to the benefit of enhancing tensile ductility and reducing the density of ECC, glass bubbles have a hollow spherical structure with air entrapped inside and thus possess very low thermal conductivity. Glass bubbles are thermally stable up to high temperature (600 °C) as shown in the Thermal Gravimetric Analysis (TGA) curve presented in **Fig.2.1**. The weight loss of the glass bubbles is less than 0.5% up to 600 °C. Therefore the size of entrapped air voids in these bubbles will be maintained at micron size up to a high temperature when a significant fraction of the strength of steel is lost (about 537 °

C). As previously discussed, this is beneficial in maintaining low equivalent thermal conductivity (due to radiation across pores) at high temperature. As a result, lightweight ECC made with these glass bubbles as aggregates seems a suitable candidate for FR-ECC. One of the lightweight ECC mixtures (with minor modification on the fiber geometry) studied by Wang and Li was selected and investigated in this research.

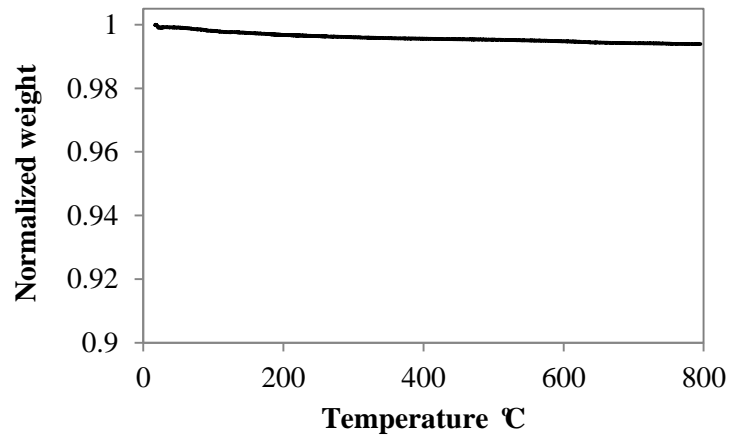


**Fig.2.1 TGA curve of micro-sized hollow glass bubbles**

Adopting the same philosophy, a similar mix was designed substituting the glass bubbles with fly ash cenospheres (FAC). Fly ash cenospheres are the lightweight part of fly ash, which are produced during combustion of coal. Fly ash cenospheres resemble the hollow spherical structure of glass bubbles and have even greater thermal stability under high temperature, yet they are much more economical and environmentally friendly compared to glass bubbles. To keep the matrix toughness low, fly ash cenospheres of size available in less than 106 microns were used.

The physical properties of the lightweight aggregates (GB and FAC) and the PVA fiber are listed in **Table 2.1** and **Table 2.2**, respectively. Two candidate mixes for FR-ECC using glass

bubbles (Mix 1) and fly ash cenospheres (Mix 2) were studied in this research and the mix details are listed in **Table 2.3**.

**Table 2.1 Physical property of glass bubbles and fly ash cenospheres**

	Glass bubble	Fly ash cenosphere
Specific gravity	0.38	0.85-0.95
Composition	Soda-lime-borosilicate glass	Silica/Alumina/Iron
Average diameter ( $\mu\text{m}$ )	40	75
Effective maximum diameter ( $\mu\text{m}$ )	85	106
Isostatic crush strength (MPa)	27.6	22.1
Melting temperature ( $^{\circ}\text{C}$ )	600	1200-1400

**Table 2.2 Characteristics of PVA fiber**

	PVA
Nominal Strength, MPa	1620
Apparent Strength, MPa	1092
Diameter, $\mu\text{m}$	39
Length, mm	8
Young's Modulus GPa	42.8
Elongation (%)	6.0
Density, $\text{kg/m}^3$	1300
Melting temperature, $^{\circ}\text{C}$	230

Micrographs from a Scanning Electron Microscope (SEM) of the mixes are shown in **Fig.2.2**. It can be seen in that the micro glass bubbles/fly ash cenospheres are well dispersed within the matrix and maintain their spherical shape with entrapped air inside. This indicates that these micro spherical aggregates survive the mixing procedure and maintain their original microstructure as desired.

**Table 2.3 Mix design of FR-ECC candidates**

	Cement	GB/FAC	Water	Fiber
Mix 1	1	0.5 (GB)	0.75	2% by Volume
Mix 2	1	0.8 (FAC)	0.75	2% by Volume

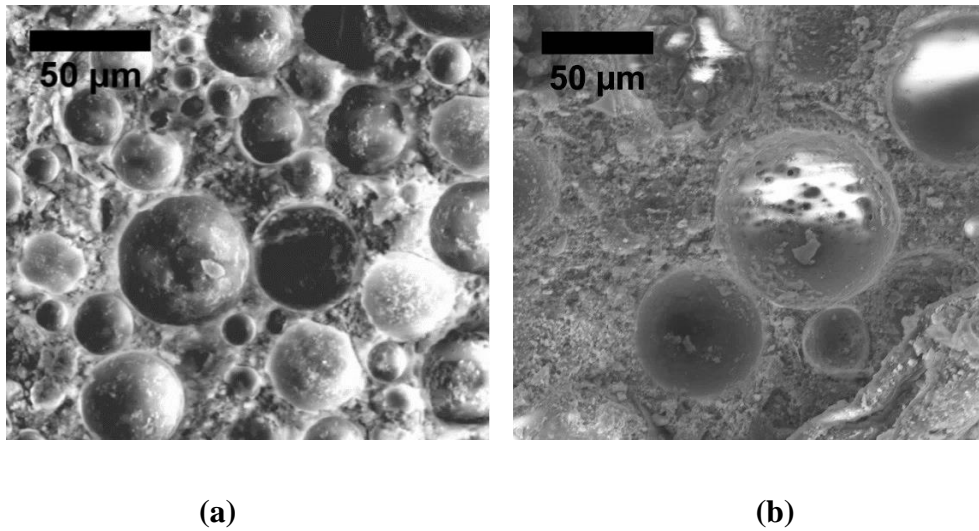


**Fig.2.2 SEM images of  
(a) glass bubbles and (b) fly ash cenospheres within the SFR-ECC mixtures**

### **2.2.2 Mechanical Properties Characterization**

The cohesive (mechanical) properties characterization of FR-ECC (Mix 1 and 2) involved experimental determination of uniaxial compressive strength and direct tension behavior.

Compressive strength of FR-ECC was measured using a set of three cube specimens of side 50.8 mm. The test was conducted using a compression test system at a loading rate of  $1300 \pm 300$  N/sec in accordance with ASTM C109<sup>15</sup>.

The direct tension tests were conducted using the uniaxial tension test setup on a set of three dogbone-shaped specimens. In this preliminary study, the material was cast into the desired specimen configuration instead of spraying. Tests were conducted on a test system with 20 kN capacity, under a displacement control at the rate of 0.5 mm/min as recommended by the Japan Society of Civil Engineers for direct tension testing of High Performance Fiber Reinforced Cementitious Composites<sup>16</sup>. Two external linear variable differential transducers (LVDTs) were attached to the specimen edges, with a gage length of approximately 101.6 mm, to measure the tensile strain. The uniaxial tensile test configuration is plotted in **Fig.2.3**.

All specimens were tested at the age of 28 days after curing under laboratory room conditions ( $23\pm 3\text{ }^{\circ}\text{C}$ ;  $30\pm 10\%$  RH). The compressive strength and tensile stress-strain curve of the FR-ECC specimen were obtained using the aforementioned test setups.

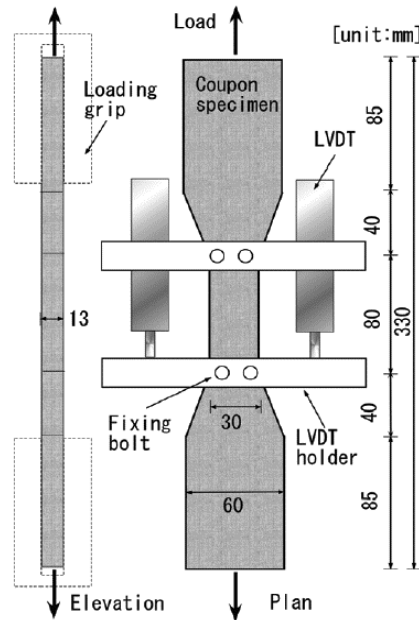


**Fig.2.3 Uniaxial tensile test configurations for FR-ECC<sup>16</sup>**

### 2.2.3 Thermal property Characterization

To assess the insulation property of FR-ECC, the apparent thermal conductivity of the material was measured using a thermal capacitance calorimeter in accordance with ASTM E2584<sup>1</sup>. A high density SFRM with density of  $704\text{-}768\text{ kg/m}^3$  (similar to the density of FR-ECC) commonly used in the US was adopted as control to evaluate the performance of FR-ECC mixes. The test configuration is shown in **Fig.2.4**. The setup requires two plate specimens of insulation material (that is being tested) with dimension of  $152.4\text{ mm} \times 152.4\text{ mm} \times 25.4\text{ mm}$  sandwiching a stainless steel slug. Additional insulation material with very low thermal conductivity was used to cover all four edges of the specimen to enforce a one dimensional heat transfer within the specimen. The



assembled specimen was then placed in a small-scale furnace with maximum heating capacity up to 1000 °C, and heated up from room temperature to a critical temperature where the corresponding steel slug temperature reaches 537 °C (the temperature at which steel experiences substantial strength loss) at the rate of 5 °C/min. The temperature of the slug ( $T_{slug}$ ) and outer surface of the specimen ( $T_{surface}$ ) were measured and recorded at a constant time interval of 1 minute using K-type thermocouples. After reaching the critical point, the test was aborted by shutting down the furnace and the specimen was allowed to naturally cool down to room temperature. Two heating and cooling cycles were adopted for more reliable data.

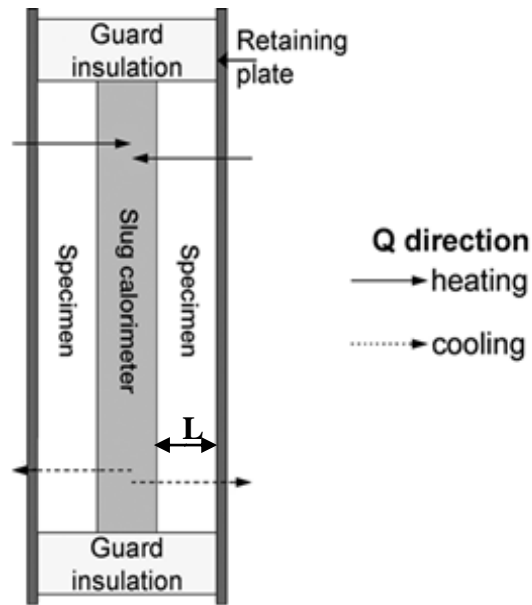


**Fig.2.4 Apparent thermal conductivity test setup (ASTM E2584<sup>18</sup>)**

The apparent thermal conductivity of FR-ECC/SFRM is calculated based on one-dimensional heat transfer analysis as:

$$\lambda_a = \frac{FL(M^{SSS} C_p^{SSS} + M^{SPEC} C_p^{SPEC})}{2A\Delta T} \quad (2.1)$$

where  $\lambda_a$  is the apparent thermal conductivity of the tested specimen; F is the measured heating rate within the slug (determined as the time derivative of  $T_{\text{slug}}$ ); L is the thickness of the specimen;  $M^{\text{SSS}}$  and  $M^{\text{SPEC}}$  are the masses of steel slug and plate specimen of the insulation material being tested, respectively;  $C_p^{\text{SSS}}$  and  $C_p^{\text{SPEC}}$  are their respective heat capacities – here, heat capacity of the steel slug is determined using the expression  $C_p^{\text{SSS}} = 6.683 + 0.04906 * T + 80.74 * \ln(T)$  (T is in Kelvin.)<sup>20</sup>; A is the area of the specimen perpendicular to the heat flow; and  $\Delta T$  is the temperature gradient between the two surfaces of a plate specimen (determined as the difference between  $T_{\text{surface}}$  and  $T_{\text{slug}}$ ). The specific heat capacity ( $C_p^{\text{SPEC}}$  in **Eq. 2.1**) of materials (FR-ECC and control SFRM) was characterized using differential scanning calorimetry (DSC) in accordance with ASTM E1269<sup>17</sup>.

#### 2.2.4 Cohesive property under impact load

To directly assess the cohesive property of FR-ECC compared to conventional SFRM, FR-ECC (and control SFRM) covered steel substrate was tested under impact load. In this part of the study, Mix 1 was used to represent FR-ECC. As pointed out above, failure of the insulation cover can be due to lack of adhesion between insulation material and steel, or lack of cohesion within the insulation material. This study focuses on comparing the cohesive behavior of FR-ECC and SFRM. The integrity of FR-ECC compared to conventional SFRM under impact loads was evaluated using a drop weight test (**Fig.2.5**) in terms of number of drops needed to detach the insulation cover from a steel substrate. Thin square steel panels with dimensions of 304.8mm x 304.8mm x 9.53mm were used as steel substrates to emulate a real steel structural element. In this preliminary study, again the FR-ECC was cast, instead of sprayed, on this steel substrate. A widely used type of commercial water-based bonding agent was applied on the substrates to enforce

adequate bonding on the steel surface to deliberately force the damage to form within the material, thereby eliminating the possibility of adhesive failure. Control specimen with the same type of conventional high density SFRM was also prepared and tested. One specimen for each type of insulation material (FR-ECC or SFRM) was tested for behavior characterization.

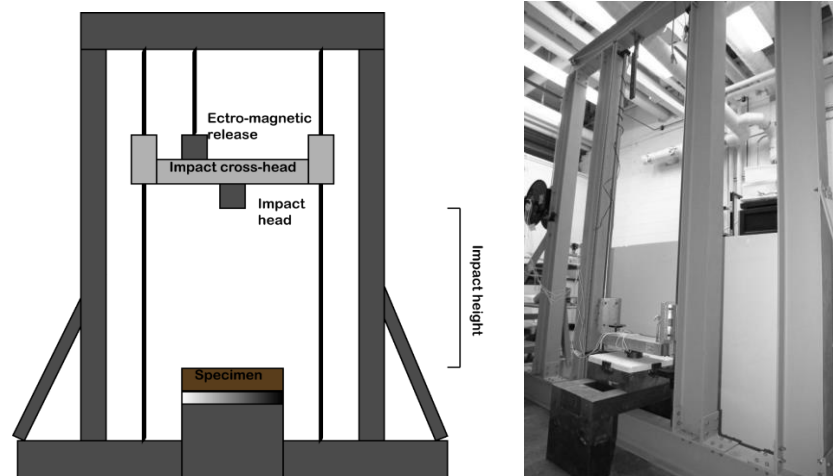


**Fig.2.5 Drop weight tower impact test setup**

During the test, the steel substrate was simply supported on its edges. Impact test was performed using drop weight of 8.91 kg with an impact head of 50.8 mm in diameter freely falling from a height of 1.17m on the specimen (FR-ECC/SFRM coated steel panel). After each impact, the conditions of the FR-ECC and SFRM material (including the interfacial condition) were examined and photographically documented to qualitatively assess the integrity of the insulation cover.

### **2.2.5 Wrapped-around durability study**

The damage tolerance of FR-ECC gives rise to a potentially new concept of wrapping a continuous layer of FR-ECC around the steel members thereby eliminating the need for a strong adhesive strength at the steel-FR-ECC interface. The central idea is that if a structural steel member

is continuously covered by FR-ECC (fully wrapped-around – **Fig.2.6**) which can maintain its continuity and integrity under mechanical and thermal loads, the integrity of the steel-FR-ECC system is assured even when the bonding between steel and the FR-ECC (insulation) cover is lost. Thus, the wrapped-around durability concept provides an extra level of safeguard for steel members against fire, in addition to strong adhesive bonding between FR-ECC and steel.

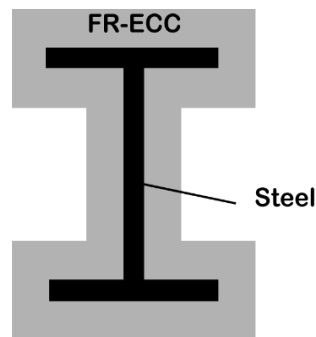


**Fig.2.6 Wrapped-around specimen configuration**

In order to evaluate the wrapped-around durability concept, low velocity impact testing of a steel I-beam section fully wrapped with FR-ECC (and SFRM as control) was performed using the drop-weight test with an impact head of 50.8 mm in diameter. Again Mix 1 was used to represent FR-ECC in this part of study. The wrapped-around durability is directly related to the impact resistance of the fire-proofing material (SFRM/FR-ECC). The beam specimens were prepared by applying approximately 12.7 mm thick FR-ECC/SFRM layer on an S4x7.7 I-beam. The thickness of the fire-proofing materials was chosen based on common practice in the field. The beam was 609.6 mm long, and the fireproofing material was applied on the mid 406.4 mm length leaving about 101.6 mm space at each end for the simple-support. For FR-ECC specimen, oil release agent was applied on steel surface to deliberately create a totally “bond-free” interface between steel and FR-ECC to evaluate the integrity of the fire-proofing material with no bond with steel under impact loadings. In the control specimen made with SFRM, no oil release agent was

used and SFRM was naturally bonded to the steel surface. Impact tests consisting of four series of impacts were applied to the wrapped-around beam specimens. The drop weight, drop height, and number of impacts in each impact series are listed in **Table 2.4**. The drop weight test was designed to fail the specimen by gradually increasing the impact energy applied to the specimens, and the drop weights and heights were chosen considering the capacity of the drop weight tower. Examinations and photo documentations of the specimens were conducted after each impact to qualitatively evaluate the damage condition of the specimen.

**Table 2.4 Impact details of “durable wrap-around” test**

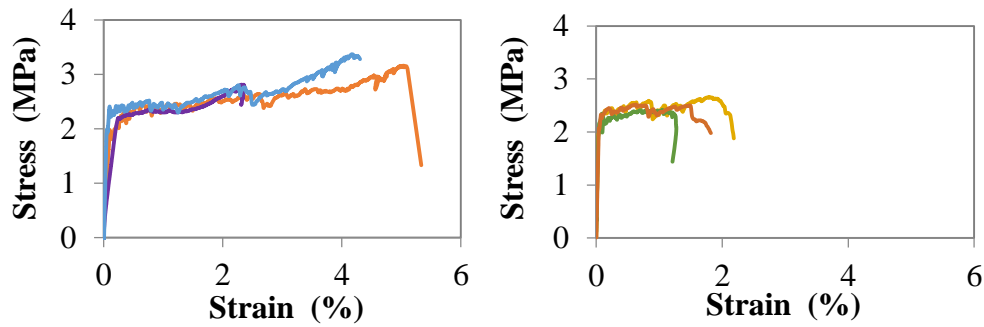
Impact Series	Number of Impacts	Drop Weight kg	Drop Height cm
1	3	5.05	86.36
2	3	7.31	86.36
3	3	7.31	111.76
4	6	8.91	111.76

## 2.3 EXPERIMENTAL RESULTS AND DISCUSSION

### 2.3.1 Mechanical properties

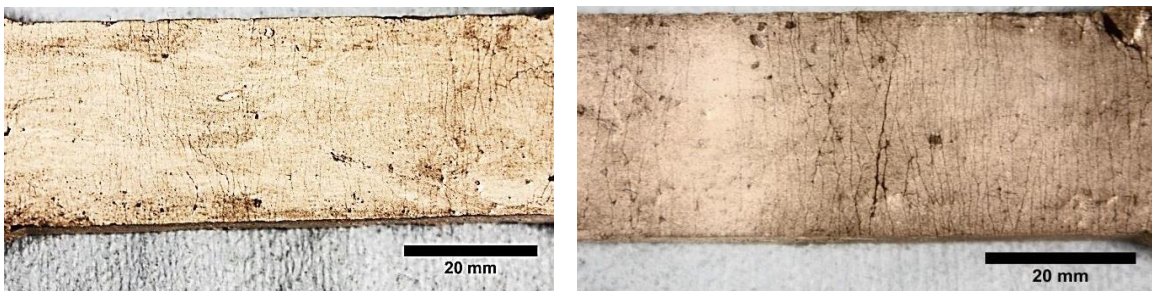
Compressive strength of FR-ECC Mix 1 and 2 at 28 days are measured to be  $22.3 \pm 3.3$  MPa and  $20.5 \pm 0.5$  MPa, respectively. The measured compressive strength of Mix 1 is fairly similar to the reported compressive strength in the literature (21.8 MPa)<sup>14</sup>. The compressive strengths of both FR-ECC mixes surpass the minimum strength specifications<sup>18,19</sup> for fire-proofing materials by an order of magnitude. The dry densities of FR-ECC measured according to ASTM E605<sup>20</sup> are 857 kg/m<sup>3</sup> and 960 kg/m<sup>3</sup> for Mix 1 and 2, respectively. Such densities are comparable with conventional high density SFRM typically within the range of 640-1280 kg/m<sup>3</sup>.

The direct tensile stress-strain relationships of FR-ECC Mix 1 and 2 are shown in **Fig.2.7**. Robust strain-hardening behavior with average tensile strain capacities exceeding 1.5% and tensile strength over 2 MPa are observed for both mixes. In particular, Mix 1 exhibits a tensile strain capacity as high as 2.9% on average. These values are about one to two orders of magnitude larger than those of SFRM. The high tensile strength and tensile ductility enables FR-ECC to withstand stress induced by vibration and accommodate large deformation without delamination or substantial cracking. This will be critical under multi-hazard scenarios. Under impact, the induced acceleration could impose tensile stress in the fire-resistive material. Under earthquake loading, structural steel is likely to go through large deformation and even yield at certain locations and such deformation poses large strain on the fire-resistive material covering the steel. The higher tensile strength and strain capacity of FR-ECC are expected to reduce the tendency of delamination and cracking under such loading conditions. In addition, the average residual crack width after unloading is approximately 15  $\mu\text{m}$  for both Mix 1 and 2. The crack patterns of the specimens are shown in **Fig.2.8**. In these pictures, carbon black solution was applied to the specimen surface after the tensile test to improve the visibility of the cracks, since these cracks are almost invisible for naked eyes. The micro-sized cracks have minimal effect on the thermal insulation property of FR-ECC compared with large crack openings. Therefore, FR-ECC with high strength and ductility as well as tight crack width, is expect to maintain its integrity and functionality and protect steel structures against fire even under extreme loading conditions, particularly under multiple hazards.



(a) Mix 1 containing glass bubbles (b) Mix 2 containing fly ash cenospheres

**Fig.2.7 High tensile strength and ductility attained in two FR-ECC mixes**



(a) Mix 1 containing glass bubbles (b) Mix 2 containing fly ash cenospheres

**Fig.2.8 Crack pattern of FR-ECC tensile specimens**

Comparing the tensile results of FR-ECC Mix 1 and 2, Mix 1 shows better tensile behavior, with slightly higher tensile strength and doubled the strain capacity when compared with those of Mix 2. It should be noticed that the volume fraction of lightweight aggregate (GB or FAC) in Mix 1 is higher than that of Mix 2, yet Mix 1 shows higher first cracking strength and ultimate tensile strength. It is observed that the workability of Mix 1 is better than that of Mix 2. Possible reasons of the difference in workability are that fly ash cenospheres have higher water absorption than glass bubbles and the shape of fly ash cenospheres are not perfectly smooth and spherical (due to the nature of industrial waste). The resulting lower workability could affect the homogeneity of the matrix and lead to non-uniform fiber dispersion. It is also likely that the fiber/matrix interfacial bonding properties are affected by the fresh property. These effects may result in lower strength and larger variability in the strain capacity of Mix 2. The overall mechanical performance of FR-

ECC Mix 1 (with glass bubbles) is better and more consistent than Mix 2 (with fly ash cenospheres). However, Mix 2 still exhibits significantly improved mechanical performance over conventional SFRM, with the benefit of being greener by consuming an industrial by-product.

### 2.3.2 Thermal properties

The thermal conductivities, which directly relate to fire-proofing abilities, of the three materials (FR-ECC Mix 1, 2 and control SFRM) are compared using the calculated apparent thermal conductivity obtained from the one-dimensional heat conduction analysis (**Eq.2.1**). The specific heat capacities of both the materials and masses of the plate specimens needed in Eq.2.1 were experimentally determined.

The specific heat capacities of FR-ECC Mix 1, Mix 2 and control SFRM ( $C_p^{\text{SPEC}}$  in **Eq.2.1**) were determined using DSC. Instead of treating the specific heat capacity as a temperature-dependent variable, the specific heat capacity measured (at 400 °C) for both materials was assumed constant throughout the entire temperature range (approximately 40-670 °C) under investigation. This assumption is justified by previous research<sup>21</sup> which indicates negligible difference in the apparent thermal conductivity derived using **Eq.2.1**. The measured specific heat capacities  $C_p^{\text{SPEC}}$  are 930 J/(kg K), 757 J/(kg K) and 947 J/(kg K) for FR-ECC Mix 1, Mix 2 and SFRM (control), respectively.

The mass of the specimen was considered as temperature-dependent in this study as it varied considerably (for both FR-ECC and SFRM) before and after the thermal conductivity tests due to physical and chemical reactions (such as loss of moisture and decomposition of hydration product). During the thermal conductivity experiments, the mass loss is typically 15-30% after heating from room temperature (20 °C) up to approximately 700 °C. Based on this observation, the



mass of the specimen ( $M^{SPEC}$ ) was assumed to be a linear function of temperature as shown in Eq.2.2.

$$M^{SPEC} = M_0 + \frac{M_f - M_0}{T_{max} - T_0} (T - T_0) \quad (2.2)$$

where  $M_0$  and  $M_f$  are measured specimen mass before and after test;  $T_{max}$  and  $T_0$  are the maximum specimen temperature during test and the initial room temperature before heating. The error caused by assuming that the mass loss is a linear function of temperature is expected to be insignificant because the  $M^{SSS}C_p^{SSS}$  term is much larger than the  $M^{SPEC}C_p^{SPEC}$ . The linear function of mass is used only in the heating phase of first heating/cooling cycle and assumed to be a constant during the cooling phase of the first cycle and entire second cycle. This assumption is reasonable because most of the physical and chemical changes associated with temperature are completed during the first heating phase.

The apparent thermal conductivity of FR-ECC Mix 1, Mix 2 and SFRM (control) specimens are subsequently determined by the temperature measurements on the outer surface of the specimen ( $T_{surface}$ ) and in the stainless slug ( $T_{slug}$ ). The apparent thermal conductivity, as a function of average specimen temperature (determined as the average of  $T_{surface}$  and  $T_{slug}$ ) within the heating phase of the first heating/cooling cycle, are plotted in **Fig.2.9**. These curves are based on the test results of sets of three specimens for all materials investigated. The drop in apparent thermal conductivity in the first cycle is caused by a variety of physical and chemical reactions, such as evaporation of moisture, loss of physical bonded water, etc., which delays the temperature rise. This phenomenon was not observed in the heating phase of the second cycle.

It is observed that apart from a slightly higher averaged thermal conductivity of FR-ECC

compared to SFRM between 180 °C and 240 °C, FR-ECC exhibits a lower thermal conductivity compared to the control (SFRM) specimen over much of the temperature range investigated in this paper. The reduction in apparent thermal conductivity between 100 ~ 400 °C for all materials tested is associated with endothermic reactions including evaporation of free moisture, and decomposition of physically and chemically bonded water, that delay the temperature rise. The generally higher water content in SFRM compared to FR-ECC may be the reason behind the observed lower apparent thermal conductivity of SFRM over this temperature range. Based on the measured thermal conductivity data, it is expected that the FR-ECC would offer similar, if not better, fire resistance for steel structures when compared with the control SFRM.

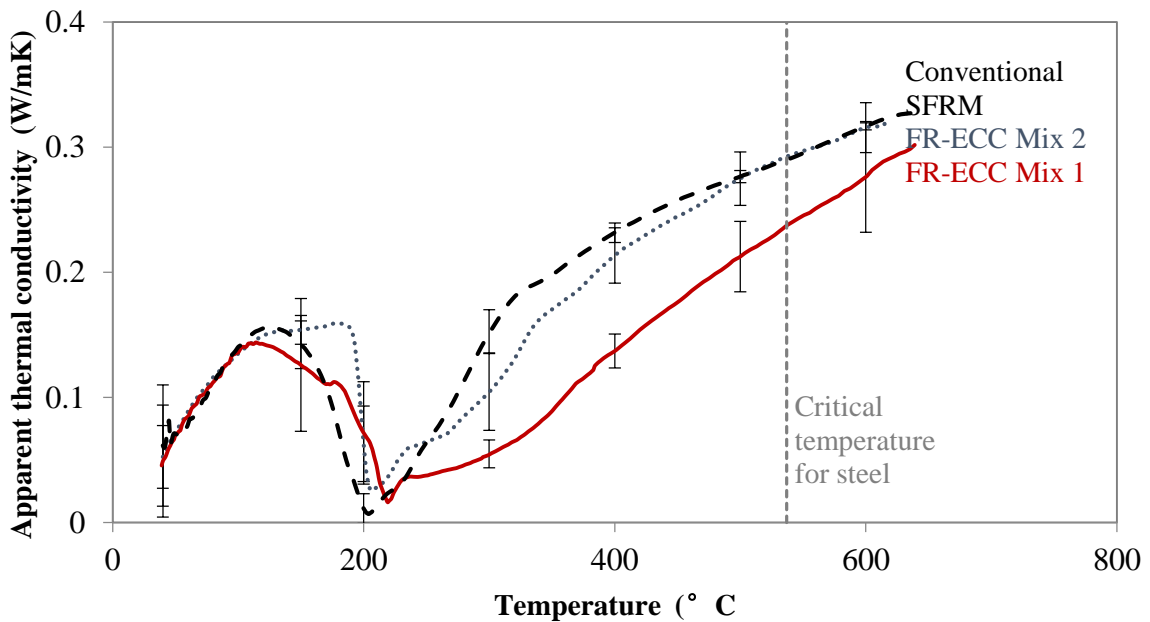


**Fig.2.9 Measured apparent thermal conductivity of FR-ECC and control SFRM**

It is also observed that FR-ECC Mix 1 exhibits a lower thermal conductivity than FR-ECC Mix 2. This is due to a lower density (and higher air content) in Mix 1 than that in Mix 2, associated with higher volume fraction of lightweight aggregates. Further, glass bubbles have a lower thermal

conductivity than fly ash cenospheres.

**Fig.2.10** shows the apparent thermal conductivity of FR-ECC (Mix 1) measured during two consecutive heating and cooling cycles. Other than the first heating cycle (reasons explained above), the thermal conductivity shows a good consistency during both heating/cooling cycles. Since the thermal conductivity is mainly governed by the pore structure inside the material, this consistency may indicate that the pore structure is stable under multiple heating and cooling cycles. This observation also justifies using these lightweight aggregates as they are very stable under elevated temperature and are able to maintain the pore structure as desired. The thermal insulation ability of FR-ECC over the heating cycles is considered satisfactory.

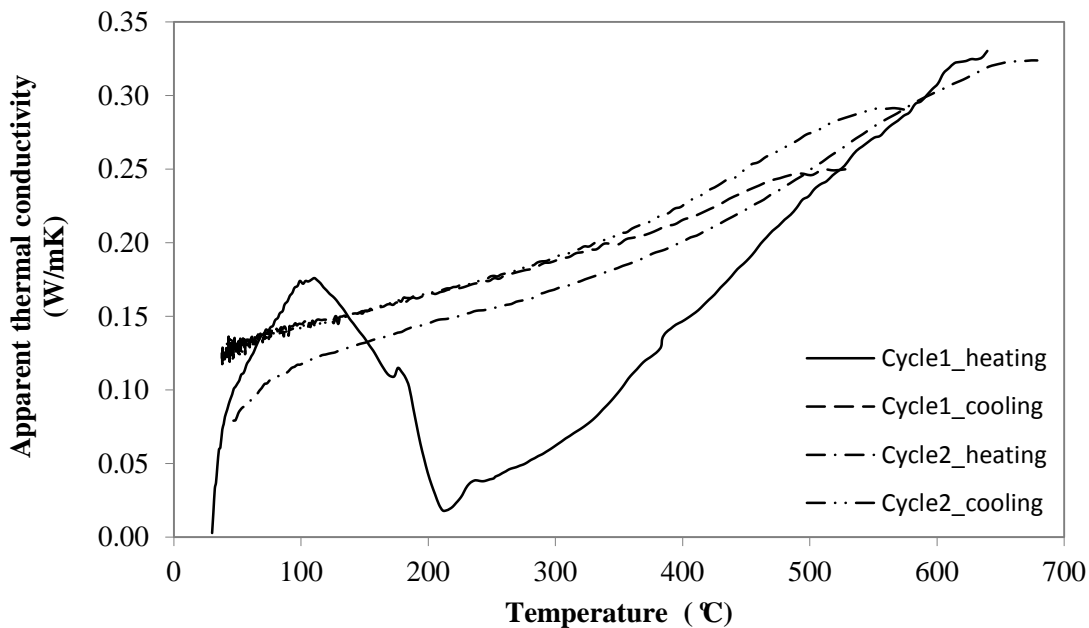


**Fig.2.10 Measured apparent thermal conductivity of FR-ECC (Mix 1) during two consecutive heating/cooling cycles**

The thermal conductivity characterization demonstrated that the lightweight ECC (developed with glass bubbles and fly ash cenospheres) possess suitable thermal insulating property as a fire protection material. It is feasible to combine low thermal conductivity and high

tensile ductility simultaneously in one material. This experimental study also confirmed that glass bubbles and fly ash cenospheres are effective in reducing the thermal conductivity (as compared to regular ECC M45) of the ECC material. This technique could therefore be used in the further development of the ultimate SFR-ECC for achieving thermal insulating property.

### **2.3.3 Cohesive property under impact load**

The cohesive strengths of both fire-proofing materials (FR-ECC and SFRM) were evaluated experimentally using drop-weight impact tests on steel panel substrates covered with a fire-proofing material layer of thickness 25.4 mm (which is a typical thickness in field construction), as detailed in previous section. **Fig.2.11** shows the contrast of failure pattern in SFRM (after six successive impacts) and micro-crack pattern (without failure) in FR-ECC specimen after twelve successive impacts.

The material integrity was not preserved in the SFRM specimen even with the presence of strong interfacial adhesion with steel substrate. After the first impact, no noticeable damage was observed in SFRM specimen. However, the SFRM began to detach from the substrate after the second impact. Finally, after the sixth impact, most of the SFRM had detached as shown in **Fig.2.11(a)**. Delamination occurred within a few millimeters near the interface and large millimeter sized radial cracks formed due to the tensile stress in the circumferential direction caused by the impacts. The conventional SFRM, when strongly bonded with the steel, disintegrates through development of large millimeter sized radial cracks and delamination within the SFRM parallel to the steel/SFRM interface.

FR-ECC specimen survived all 12 successive impacts without loss of material integrity. After the first impact, minor debonding of the ECC/steel interface at the edge was observed. After

six impacts, micro-cracks began to appear in the ECC specimen and gradually increased in length, thereafter. **Fig.2.11(b)** shows the final crack pattern after all the 12 impacts. Although slight debonding at the steel-FR-ECC interface was observed at the edge and corners; the use of bonding agent kept most of the interface intact and bonded. In the FR-ECC specimen, the impact energy is mainly dissipated through the development of micro-sized multiple cracks distributed over the volume of material. During the micro-cracking process, the fibers bridging the cracks partially debond and slip against the matrix, which dissipates the impact energy at the fiber/matrix interface and prevents catastrophic failure of the FR-ECC insulation.

These impact test results show that even with the enforced strong bonding with the steel substrate, the cohesive strength is still a bottleneck for conventional SFRM, which prevents it from resisting the impact loads. In contrast, for FR-ECC, the high tensile strength and ductility ensure high cohesive strength and deformation compatibility with the steel substrate, which allow the FR-ECC insulation to take repeated impacts without failure.

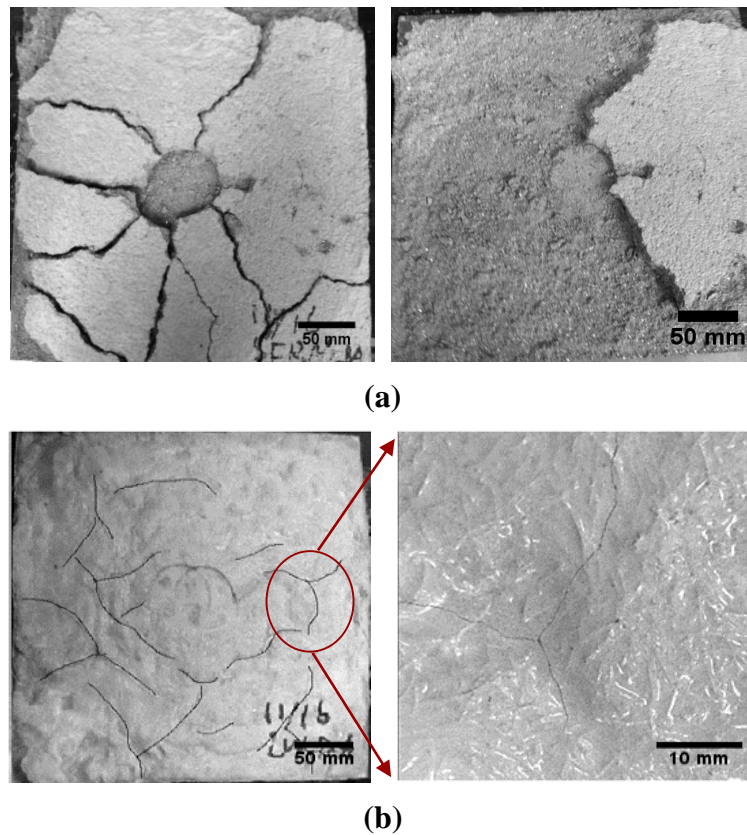


**Fig.2.11 Damage condition of**

**(a) SFRM after 6 impacts; and (b) FR-ECC panel specimens after 12 impacts**

**Left image in (a) shows the delaminated SFRM. Right image in (a) shows the final condition of the steel panel.**

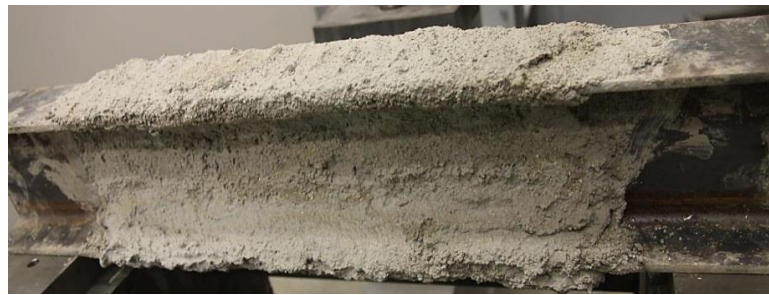
**Left image in (b) shows the overall crack pattern. Right image shows enlarged micro-cracks in red circle in left image**

### **2.3.4 Wrapped-around durability**

Very different behavior of SFRM and FR-ECC protected beam were observed during the impact tests on wrapped-around specimens.

Significant loss of insulation layer in the SFRM protected beam was observed after the second series of impacts, especially around the disk-shape impact head. After four series of impacts, most of the insulation material was detached leaving the steel beam almost bare, as shown in **Fig.2.12**. The detachment of insulation layer initiated in the flange region and later extended to the web region of the steel beam. It was observed that the insulation material detached piece by

piece which indicates that the material remaining on the steel beam exerted no restraint on the adjacent falling piece, and the insulation was attached to the substrate mainly due to adhesion at the interface. For such material system, adhesion is necessary and adhesive failure could lead to ultimate failure. The “wrapped-around” concept is not valid in conventional SFRM due to the poor cohesion within the material.



**(a) Before impact**



**(b) After 1<sup>st</sup> series of impacts (damage at impact point, top flange (arrow))**



**(c) After 2<sup>nd</sup> series of impacts (SFRM dislodged at impact point, and partially delaminated adjacent to impact)**



**(d) After 3<sup>rd</sup> series of impacts (complete delamination on top flange)**

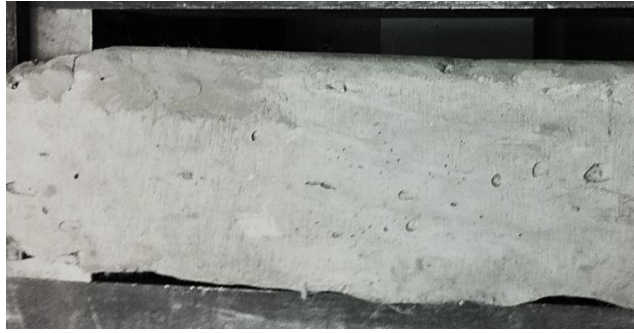


**(e) After 4<sup>th</sup> series of impacts (cracking and delamination of SFRM on web)**

**Fig.2.12 Condition of SFRM protected steel beam before and after impacts**

In the beam wrapped around by FR-ECC, shown in **Fig.2.13**, no major damage was observed in the first three series of impacts. Instead the impact head left a disk-shape indent on the FR-ECC. Slight damage on the edge of the flange was observed after the fourth series of impacts. The damage was located at the edge of the beam flange, where the steel beam imposed shear force on the FR-ECC layer due to the vibration caused by impact. However, the integrity of the FR-ECC layer was still maintained. These test results show that despite zero bonding deliberately introduced in this experiment, the high cohesion and deformation capacity of the wrapped-around FR-ECC fireproofing system provides an additional mechanism (beyond the normal adhesion between FR-ECC and steel) to keep the insulation material in place, thereby improving impact resistance and durability of the insulation layer.





(a) Before impacts



(b) After 3<sup>rd</sup> series of impacts (indent of impact head on FR-ECC on top flange)



(c) After 4<sup>th</sup> series of impacts (further indent of impact head, with minor damage adjacent to impact point; no damage of FR-ECC on web)

**Fig.2.13 Condition of FR-ECC protected steel beam before and after impacts**

It is also observed that FR-ECC protected steel beam can resist eccentric impact without catastrophic failure. In addition to the above-described impacts, an additional impact using 8.9 kg weight dropped from 112 cm height was applied at the edge of the beam where the insulation is not fully supported by the beam. Cracks in FR-ECC formed at the edge of the flange along with multiple micro cracks in the middle of the upper flange due to bending effects as shown in **Fig.2.14**. In spite of this, local and overall material integrity was still maintained under such eccentric

loading, which indicates that FR-ECC can potentially withstand various accidental impacts without major loss of insulation functionality.



**Fig.2.14 Damage condition of FR-ECC protected steel beam after eccentric impact**

The above experimental findings validated the idea of “wrapped-around” durability in FR-ECC type of material. However, this is not applicable to SFRM type of material with low cohesive strength. Such mechanism provides an extra safeguard in addition to the interfacial adhesion. In reality, the “wrapped-around” configuration is not rare. Most columns are protected in a “wrapped-around” manner, therefore in such case, the “wrapped-around” mechanism is expected to add to the durability performance of the FR-ECC insulation cover.

Similarly to the “wrapped-around” concepts, other configurations involving mechanical anchorage of FR-ECC will also contribute to the durability. For example, edges, angles and even openings on structural members could serve as mechanical anchorage for FR-ECC. FR-ECC could hang onto those elements solely depending on its cohesive characteristics. In addition to these

commonly existing anchors, additional clips and studs could also be used to provide extra anchorage for FR-ECC if needed.

Given the extra durability mechanisms, FR-ECC is more tolerable to local or even global adhesive failure. Although high adhesion to steel can be achieved through external interfacial adhesives (use of bonding agent) or through material tailoring (which will be discussed in Chapter 3), as an interfacial property, adhesion is often subject to large variability. Many factors, such as the condition of the steel surface or application methods, could have noticeable influence on the adhesive property. Totally relying on interfacial adhesion, which is the case for conventional SFRM, could result in lower robustness of the system. In the case of local debonding (loss of adhesion), local failure is expected in conventional SFRM. This has already been observed during the impact tests on SFRM covered panel/beam specimens. In contrast, FR-ECC in the debonding area could hold in place with the help of adjacent FR-ECC that are still firmly bonded or mechanically anchored to the steel. This has been demonstrated in section 2.3.3. Local debonding between the FR-ECC cover and steel substrate was observed, but the local debonding never resulted in global adhesive failure. Therefore, with the highly cohesive nature, FR-ECC is expected to show more robust durability behavior.

## **2.4 CONCLUSIONS**

In this chapter, preliminary FR-ECC mix design using large volume fraction of micro-sized hollow glass bubbles or fly ash cenospheres were investigated for its thermal and mechanical performance. The cohesive performance of FR-ECC insulation was characterized under impact load and the concept of “wrapped-around durability” was also evaluated through impact tests. Based on the results of this experimental investigation, the following conclusions are drawn:

1. The feasibility of developing a fire-resistive ECC (FR-ECC) combining good thermal insulation property and durability, facilitated by high tensile strength (relative to SFRM) and high tensile ductility, was demonstrated experimentally. The new FR-ECC has comparable thermal insulation property as current SFRM, but with tensile ductility at least two orders of magnitude higher than SFRM.
2. Glass bubbles and fly ash cenospheres were successfully used in the ECC material to achieve low thermal conductivity without sacrificing tensile performance. Therefore it is an effective material engineering approach for design of the thermal insulating property of the proposed SFR-ECC.
3. The low cohesive strength of SFRM prevents them from resisting impact loads even with the presence of strong interfacial adhesion. Therefore, low cohesion is the major bottleneck of conventional SFRM.
4. High tensile strength and damage tolerance of FR-ECC greatly improves the cohesion of the FR-ECC insulation system over conventional SFRM and helps to maintain material integrity even under severe loadings. Micro-crack formation helps to dissipate the energy induced by impact loading without catastrophic failure.
5. The “Wrapped-around” concept is experimentally demonstrated to be feasible. FR-ECC insulation systems can withstand impact load even without the presence of adhesion at the steel/FR-ECC interface, which is impossible for SFRM insulation system. Such mechanism provides extra level of safeguard in addition to interfacial adhesion and results in more robust durability behavior of FR-ECC.

The study presented in this chapter shows that FR-ECC with good mechanical performance and suitable thermal property has the potential to overcome the current durability issue of conventional SFRM and improve the overall fire resistance of a steel structure, therefore justifies the proposed solution for the problem. In addition, this chapter also demonstrated the effectiveness of using small-sized smooth-shaped lightweight aggregates (glass bubbles and fly ash cenospheres) to achieve low thermal conductivity without sacrificing the tensile ductility (high cohesion) in FR-ECC design, which provides useful information and experience for the further development of the material in Chapter 4.

## References

---

1. ASTM Standard E2584-07: Standard Practice for Thermal Conductivity of Materials Using a Thermal Capacitance (Slug) Calorimeter, ASTM Standards, ASTM Int'l, 2007.
2. Yang, E.H., and V.C. Li, "Fiber-bridging Constitutive Law of Engineered Cementitious Composites", *Journal of Advanced Concrete Technology*, Vol. 6, No.1, pp.181-193, February 2008.
3. Kanda, T. and V.C. Li, "New Micromechanics Design Theory for Pseudo Strain Hardening Cementitious Composite," *ASCE J. of Engineering Mechanics*, Vol. 125, No. 4, pp. 373-381, 1999.
4. Russell, H.W., "Principles of Heat Flow in Porous Insulators," *J. of American Ceramic Society*, 18, 1-5, 1935.
5. Loeb, A.L., "Thermal Conductivity: VIII, A Theory of Thermal Conductivity of Porous Materials," *J. of American Ceramic Society*, 37, 96-99, 1954.
6. Laurent, J.P., "An Estimation Model for the Dry Thermal-Conductivity of Autoclaved Aerated Concrete," *Material and Structures*, 24, 221-226, 1991.
7. Kunii D. and J. M. Smith, "Heat Transfer Characteristics of Porous Rocks," *A.I.Ch.E.J.*, 6(71), 1960.
8. Bouguerra, A., A. Ledhem, F. de Barquin, R.M. Dheilily, M. Queneudec, "Effect of Microstructure on the Mechanical and Thermal Properties of Lightweight Concrete Prepared From Clay, Cement, and Wood Aggregate," *J. of Cement and Concrete Research*, 28(8), 1179–1190, 1998.
9. Dos Santos, W.N., "Effect of Moisture and Porosity on the Thermal Properties of A Conventional Refractory Concrete," *J. of European Ceramic Society*, 23(5), 745-755, 2003.
10. Lu-shu, K., S. Man-qing, S. Xing-Sheng, L. Yun-xiu, "Research on Several Physico-Mechanical Properties of Lightweight Aggregate Concrete," *Int'l J. Lightweight Concrete*, 2(4), 185– 191, 1980.
11. Akman, M.S., Tasdemir, M.A, "Tasiyici Malzeme Olarak Perlit Betonlu (Perlite Concrete as a Structural Material)," 1st National Perlite Congress, Ankara, Turkey, 1977.
12. Blanco, F., P. Garcia, P. Mateos, J. Ayala, "Characteristics and Properties of Lightweight Concrete Manufactured With Cenospheres," *J. of Cement and Concrete Research*, 30, 1715–1722, 2000.
13. Bave, G., "Aerated Light-Weight Concrete-Current Technology," *Proc. of the 2nd Int'l Symposium on Light-weight Concretes*, London, 1980.
14. Wang, S., and V.C. Li, "Materials Design of Lightweight PVA-ECC," in *Proc. of HPFRCC*, A.E. Naaman and H.W. Reinhardt (ed.), Ann Arbor, MI, 379-390, 2003.
15. ASTM Standard C109: Standard Test Method for Compressive Strength of Hydraulic Cement Mortars (Using 2-in. or [50-mm] Cube Specimens), Philadelphia, PA, 2002.
16. JSCE: Recommendations for Design and Construction of High. Performance Fiber Reinforced Cement Composites with Multiple Fine Cracks (HPFRCC), March, 2008.
17. ASTM Standard E1269-11: Standard Test Method for Determining Specific Heat Capacity by Differential Scanning Calorimetry, West Conshohocken, PA, 2011.
18. International Code Council-Evaluation Service (ICC-ES): Acceptance Criteria for Spray-Applied and Intumescent Mastic Coating Fire-Protection Materials (AC377), July, 2004.
19. USACE, UFGS, Division 7, Section 07810, spray-Applied Fireproofing, August, 2002.
20. ASTM E605: Standard Test Methods for Thickness and Density of SFRM Applied to

---

Structural Members, ASTM International, West Conshohocken, PA, 2006.

21. Bentz, D.P, "Combination of Transient Plane Source and Slug Calorimeter Measurements to Estimate Thermal Properties of FRM," ASTM J. of Testing and Evaluation, 35(3), 2007.

## **CHAPTER 3 DESIGN FOR HIGH ADHESION OF FR-ECC TO STEEL**

The study documented in Chapter 3 investigates the adhesive property of FR-ECC. This includes properly characterizing the interfacial adhesive property between FR-ECC and structural steel, modifying the FR-ECC mixture for enhanced adhesion to steel, and identifying the interdependencies between the design for adhesive property and mechanical property. The findings in this chapter will provide the knowledge basis for the design of FR-ECC regarding adhesive property (to steel), which will be used in the parallel design process of SFR-ECC in Chapter 4.

### **3.1 INTRODUCTION**

In Chapter 2, fire-resistive ECC (FR-ECC), combining the thermal insulating property and high tensile strength and ductility, was developed to address the lack of durability issue with conventional spray-applied fire-resistive material (SFRM). The durability of the fire-resistive material is recognized to include two major aspects: cohesion and adhesion.<sup>1</sup> FR-ECC was shown to have inherently better cohesive property compared to conventional brittle SFRM, and therefore possesses enhanced durability.

Another important target performance of FR-ECC is strong adhesion to steel. Up to now, there has been no published information on the characterization of the adhesion of ECC material in general, and FR-ECC in particular, to steel. This chapter is intended to fill this knowledge gap.

The current SFRM/steel bond-testing standard is the so-called “mayonnaise cap” standard testing procedure<sup>2</sup>, which is a strength-based test. This measurement approach does not



differentiate between different failure mechanisms, nor does it measure the true material property since it is specimen-size dependent<sup>3</sup>. It also heavily relies on the operators' individual testing protocol and judgment. Recently, National Institute of Standard and Technology (NIST) developed a material science based approach using linear fracture mechanics principles to experimentally determine the adhesion between spray-applied fire-resistive materials (SFRM) and steel.<sup>3,4</sup> This fracture-based test method was proposed as an alternative to the strength-based standard test and proved to measure the true material properties in a more rigorous manner. Enhancing the adhesion and proper characterization of the adhesive bond between FR-ECC and steel are necessary to fully evaluate the performance and potential of FR-ECC before large-scale testing and field applications.

Previous researches<sup>5,6,7,8,9,10,11</sup> have shown that polymer latex addition is effective in strengthening the interfacial bond between cementitious material and various types of substrate including steel. The improvement is associated with the enhancement of interfacial transition zone between cementitious material and other surfaces.<sup>10,12,13,14</sup> Studies also demonstrated that for low volume content of latex addition, the non-combustible nature of the latex modified cementitious composites remained unchanged,<sup>13,15</sup> making it suitable for FR-ECC application. In this study, commercially available acrylic polymer latex was adopted as admixtures and interfacial adhesives to modify the FR-ECC/Steel bond. It is hypothesized that the utilization of polymer latex will lead to enhanced adhesion properties of FR-ECC to steel.

The inclusion of polymer admixtures into ECC may result in a change in the microstructure and micromechanical properties of ECC that may alter its mechanical properties. According to ECC design theory, the macroscopic mechanical property (tensile strength, tensile ductility, crack widths, etc.) can be linked to the microscopic microstructural and micromechanical properties (matrix toughness, flaw size and distribution, fiber geometry, fiber mechanical properties,

fiber/matrix interfacial bond properties, etc.).<sup>16,17,18</sup> Ohama found that when latex is mixed with cementitious material, a polymer film envelops the cement hydrates and aggregate surface due to coalescence of polymer particles and therefore a cement-polymer co-matrix is formed in such material. In ordinary concrete materials, the cement hydrates (C-S-H and C-H) are considered to be bound together by weak van de Waals force, resulting in low fracture toughness and tensile strength.<sup>19</sup> The formation of a co-matrix in latex-modified cementitious material provides a stronger bond between cement hydrates, and between paste and aggregates, thereby improving the fracture toughness and tensile strength of such material.<sup>20,21,22,23</sup> Also, the bond between matrix and polymer fibers may be expected to be stronger in latex modified fiber composites. In addition, increased air entrainment with polymer addition has been observed.<sup>19,21</sup> These changes in matrix properties and fiber/matrix interfacial bond could lead to competing effects on the tensile performance of ECC, according to micromechanical models. No research has been performed on characterizing the impact(s) of latex admixtures on the tensile and compressive mechanical performance of ECC, and FR-ECC in particular. However, for the final design of spray-applied fire-resistive ECC (in Chapter 4), high adhesion and cohesion (mechanical property) need to be achieved simultaneously, therefore, it is very important to understand these interdependencies.

In this chapter, the effectiveness of employing polymer latex bonding agent as admixtures and interfacial adhesives was evaluated using a recently developed fracture-based adhesion test method. Microscopic investigation was conducted to study the mechanisms of the adhesion enhancement. In addition, the impact of polymer modification on the mechanical behavior of FR-ECC was assessed by direct uniaxial compression and tension test. Experimental results and findings are all documented in this chapter.

## 3.2 EXPERIMENTAL PROGRAMS

### 3.2.1 Material

The previously studied FR-ECC (Mix 1 in Chapter 2) is used for this study. The detailed mix design is listed in **Table 3.1** (Mix 1). Acrylic latex-based bonding agent was adopted as admixture in Mix 2 and 3. The solid latex/cement weight ratio of Mix 2 and 3 were 1.875% and 3.75% respectively. The latex was added as a replacement of water as recommended by the manufacturer, thus avoiding increasing water/cement ratio. Mix 4 was identical to Mix 1 except that the bonding agent was applied directly on the steel/FR-ECC interface to facilitate adhesion. Type I ordinary Portland cement (OPC) conforming to the requirements of ASTM C150 was used in all Mix 1-4. Polycarboxylate-based high range water reducing (HRWR) admixture and viscosity modifying agent (VMA) were used simultaneously to obtain proper workability and control of fiber dispersion. Micro spherical glass bubbles and PVA fibers were used in all mixtures. In the adhesion characterization study, 0.5% fibers (by volume fraction) were used for Mix 1-4, which will be further explained in Section 3.2.2. In the study on mechanical properties of FR-ECC, 2% fibers (by volume fraction) were used for Mix 1-3. Specimens of one type of commercially available Portland cement-based medium density SFRMs were also prepared in accordance with manufacturer's guide as control specimens for comparison purposes.

**Table 3.1 Mix proportion (by weight) of the adhesion test specimen**

	Description	Cement	Water	Glass Bubble	Bonding Agent
Mix 1	FR-ECC (Mix 1 in Chapter 2)	1	0.75	0.5	0
Mix 2	Mix 1 with latex bonding agent as admixture	1	0.675	0.5	0.075
Mix 3	Mix 1 with latex bonding agent as admixture	1	0.6	0.5	0.15
Mix 4	Mix 1 with latex bonding agent applied on steel surface	1	0.75	0.5	NA

### 3.2.2 Adhesion Characterization

To properly characterize the adhesion between the previously described mixtures and steel substrate, a linear elastic fracture mechanics based method<sup>3,4</sup> was adopted in this research. This approach measures the fracture energy  $G_c$  to characterize the adhesion of the SFRM/steel assembly in “peeling” mode. The experimental configuration is illustrated in **Fig.3.1**. It involves peeling a thin steel strip off the slab composed of the fire-resistive material. The load, displacement and crack width are recorded during the test. This configuration is modeled as lifting of an elastic beam on a flexible foundation; the critical energy release rate  $G_c$  can be calculated as<sup>3</sup>

$$G_c = \frac{6P^2(\lambda a + 1)^2}{E_{steel} b^2 \lambda^2 h_{steel}^3} \quad (3.1)$$

where P is the load in equilibrium with the extended crack length  $a$ ;  $E_{steel}$  is the elastic modulus of steel; b and  $h_{steel}$  are the width and thickness of the steel strip respectively;  $\lambda$  is a coefficient associated with the stiffness of the foundation and can be calculated as<sup>3</sup>:

$$\lambda = \left( \frac{3E_{SFRM}}{E_{steel} h_{SFRM} h_{steel}^3} \right)^{\frac{1}{4}} \quad (3.2)$$

where  $E_{SFRM}$  is the elastic modulus of the SFRM (or Mix 1-4) and  $h_{SFRM}$  is the thickness of the SFRM (or Mix 1-4) slab. **Eq.3.1** is valid for the case of sufficient bonded length between steel and the slab (greater than 25 mm in this configuration).

Eq.3.1 (and the fact that  $G = G_c$  during crack propagation) leads to  $\frac{dG}{da} > 0$  implying unstable crack growth. However, under displacement control test, the load will drop as the crack extends, resulting in crack arrest. As a result, multiple pairs of  $P$ - $a$  can be measured in a single specimen.

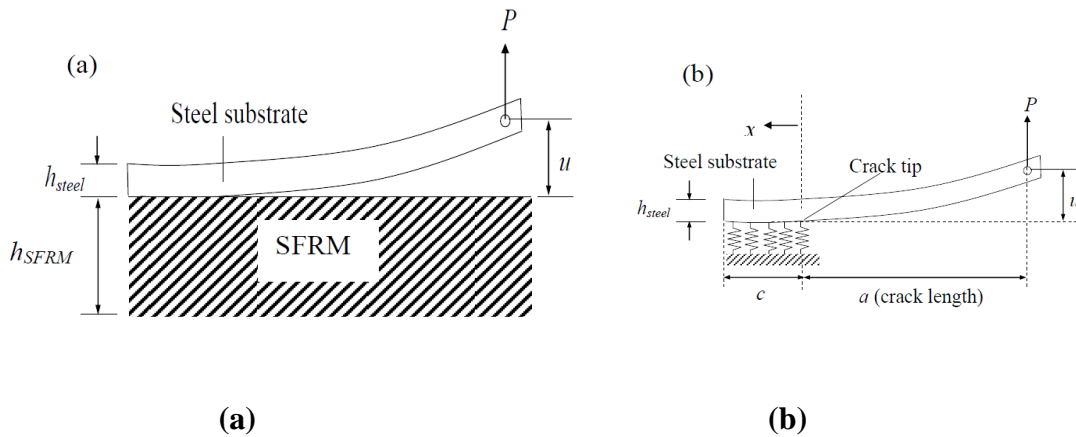


**Fig.3.1 Adhesion test<sup>4</sup>**

**(a) specimen and load configuration, and (b) interface fracture model**

The specimen was prepared by placing the steel strips at the bottom of the mold and casting the fire-resistive material to form a specimen as shown in **Fig.3.2**. Structural steel strips of 12.7mm wide and 1.27mm thick were placed at a center-to-center space of 50 mm. The thickness of casted material (Mix 1-4 and control SFRM) was approximately 25mm. The steel surface was roughened using sanding paper and cleaned with alcohol, and then a pre-crack of 12.7mm was formed by applying nonstick Teflon tape at one end of the steel strip. Mix 1-4 with 0.5% volume fraction of

fibers were used to prepare the adhesion specimen. Adhesion tests were conducted at 14 days after curing the specimens at laboratory room condition ( $23 \pm 3$  °;  $30 \pm 10\%$  RH).

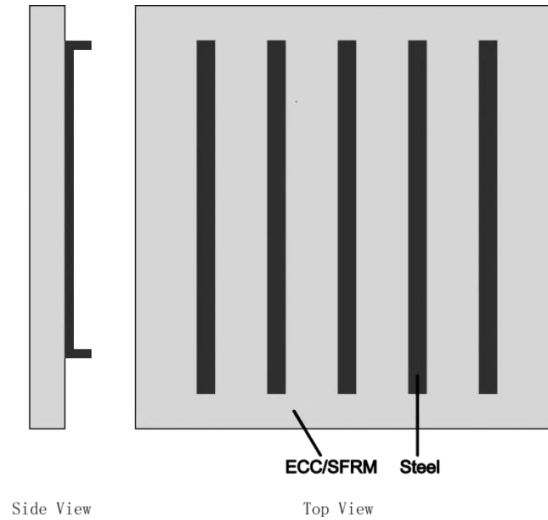


**Fig.3.2 Molding of multiple fire-resistive material / steel specimens**

This study focuses on the effect of the admixtures and surface adhesives on the adhesion, which is assumed to be mostly associated with the matrix property. A minimum fiber content (0.5%) was used to avoid large measurement deviation caused by inhomogeneity of the material associated with fibers. The small amount of fiber was included to prevent premature fracture of the FR-ECC matrix panel due to gripping during testing. As reported in Section 3.3.3, a re-test of  $G_c$  using an FR-ECC with 2% fiber shows similar results as for these specimens with lower fiber content.

The experiment was conducted on an electrodynamic load-frame with an attached S-beam load cell for higher precision (0.04N accuracy). During the test, the steel strip was lifted at one end (where the pre-crack was located) under a constant displacement rate of 1mm/min. When crack extension occurred on the interface, correspondingly, there would be a load drop. The reduced load  $P$  was recorded. At this time, the test was aborted manually and the extended crack length ' $a$ ' was

measured using a length scale with precision of 1 mm. Then the specimen was unloaded and reloaded until another crack propagation occurred. The complete unloading of the steel strip was used to confirm that no plastic yielding occurred within the steel. For the same mix proportion, at least 4 steel strip specimens were tested.

**Eq.3.1** is a simplified equation; this equation no longer holds when the crack tip approaches the other end of the strip. Depending on specimens, typically 3-6 loadings were performed on the same specimen before the crack tip became too close to the other end of the steel strip.

### **3.2.3 Microstructure Investigation**

SEM images were taken from the fractured surfaces adjacent to the steel/cementitious material interface from the cementitious material side. Environmental Scanning Electronic Microscope (ESEM) facilitated by EDAX was used in this study and images were taken after the adhesion test without any polishing or grinding preparation of the specimen. These investigations allow the examination of the modes of failure at or near the fire-resistive material/steel interface, the microstructural makeup, and the chemical composition of the surface material exposed by the fracture surface of the various mixes.

### **3.2.4 Mechanical Property**

To further understand the effect of the latex addition on the mechanical property of FR-ECC, mechanical properties characterization of Mix 1, 2 and 3 (with 2% fiber content) was performed.

Compressive strength of the mixes was measured using a set of three cube specimens of side 50.8 mm. The test was conducted using a compression test system at a loading rate of  $1300 \pm 300$  N/sec in accordance with ASTM C109<sup>24</sup>.

Direct tension tests were conducted using the uniaxial tension test setup on a set of three specimens in accordance to Recommendations for Direct Tension Testing of High Performance Fiber Reinforced Cementitious Composites by the Japan Society of Civil Engineers<sup>25</sup>. A set of 3 dog-bone shape specimens were tested on a test system with 20 kN capacity, under a displacement control at the rate of 0.5 mm/min. Two external linear variable differential transducers (LVDTs) were attached to the specimen edges, with a gage length of approximately 101.6 mm, to measure the tensile strain.

All specimens were tested at the age of 28 days after curing under laboratory room conditions ( $23 \pm 3$  °C;  $30 \pm 10\%$  RH). The compressive strength and tensile stress-strain curves of the mixes were obtained using the aforementioned test setups.

### **3.3 RESULTS AND DISCUSSION**

#### **3.3.1 Adhesion Characterization**

The  $G_c$  on the interface between the mixes and steel can be calculated at various crack length using Eq.3.1. A typical  $G_c$  v.s. crack length curve for FR-ECC (Mix 1) specimen is plotted in **Fig.3.3(a)**. As **Fig.3.3(a)** shows, the curve reaches a plateau value. This indicates that small scale yielding behavior dominates. At smaller length (usually during the first loading), the measured  $G_c$  might be higher or lower than the plateau value. A plausible reason is that the crack initiates from the blunt pre-crack resulting in a  $G_c$  higher than the plateau value, and this is often



observed in control SFRM specimen. However, for Mix 1-4, the initial  $G_c$  values at small crack length may be below the plateau value, suggesting the possibility of a process zone development before small scale yielding becomes valid at larger crack length. The plateau value represents the steady-state critical energy release rate and is used to quantify the adhesion on the interface.

Due to the naturally large standard of deviation with adhesion data, a further step of interpreting the data is taken to better extract useful information from the data. Using **Eq.3.1**,  $P^2$  can be plotted against  $\frac{\lambda^2}{(\lambda a + 1)^2}$  based on the data from the plateau regime, and linear regression of the data is then used to obtain  $G_c$  from the slope  $k$  of the best fit line. As shown in **Fig.3.3(b)**, linear regression is carried out on data derived from the **Fig.3.3(a)**, the coefficients of linear regression of most specimen are greater than 0.95. Then the adhesion energy is calculated as:

$$G_c = \frac{6k}{E_{steel} b^2 h_{steel}^3} \quad (3.3)$$

where  $E_{steel}$  is the elastic modulus of steel; and  $b$  and  $h_{steel}$  are the width and thickness of the steel strip, respectively. The mean value and standard deviation of the adhesion energy based on multiple specimens are then calculated. The results of  $G_c$  for all material mixes tested are summarized in **Fig.3.4**.

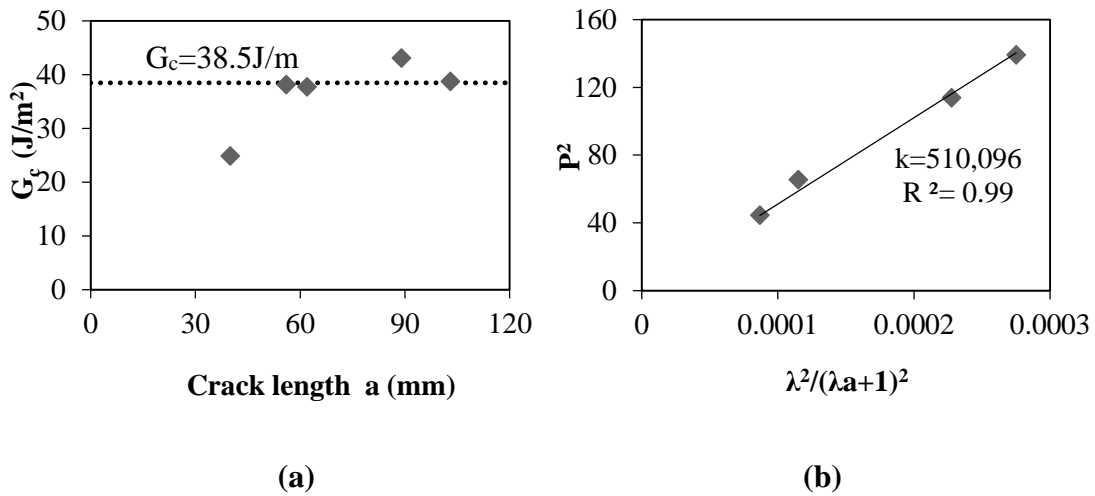


**Fig.3.3 Example of the data analysis of an adhesion specimen of Mix 1**  
**(a) Point-based calculation of adhesion energy on the specimen; (b) Extraction of the adhesion energy from the slope of the curves**

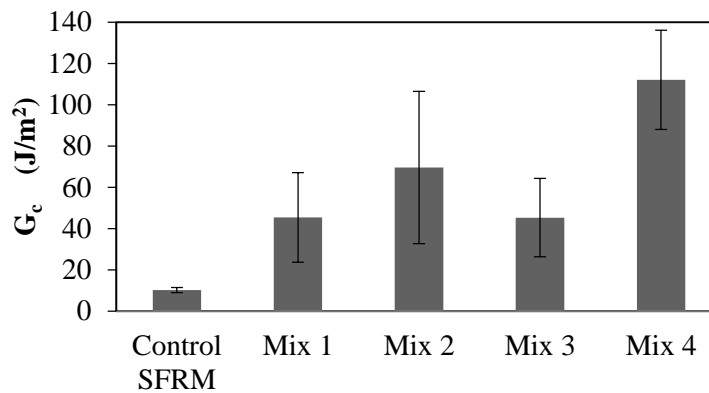


**Fig.3.4 The adhesion energy of FR-ECC matrices to steel is significantly higher than that of SFRM / steel**

The adhesion test result shows that Mix 1 has a better adhesion to steel substrate than the SFRM control specimens and the adhesion is further improved by modifying the mixture with acrylic latex emulsion. The measured adhesion energy for SFRM is 11.1 J/m<sup>2</sup>, this value is on the higher end of the reported data in the literature<sup>3</sup> for SFRM adhered to structural steel substrate (3~12 J/m<sup>2</sup>). The control SFRM used in this study is a medium density, Portland cement-based SFRM reinforced with cellulose fiber, which could lead to a relatively higher  $G_c$ . Mix 1-4 all exhibit significantly higher adhesion than the control SFRM. Mix 2 performs significantly better

(54% improvement) compared to unmodified Mix 1, which demonstrates that the addition of latex bonding agent as admixtures is effective in improving the surface adhesive property between such mix and steel substrate. However, the Mix 3 specimens do not have substantial improvement over unmodified Mix 1 specimen. It is suspected that excessive amount of water replacement by polymer latex can cause the paste to dry up too rapidly to allow sufficient time for the cementitious material to interact with the substrate at the interface. This observation is also consistent with previous research findings<sup>9</sup>. Consequently, Mix 3 will not be further investigated. Applying the bonding agent directly on the steel surface (Mix 4) is demonstrated to be the most effective method to improve the adhesion, which increases the critical energy release rate by 147% over that of Mix 1.

The failure mode of the FR-ECC (matrix) mixes is very different from that of the control SFRM. In SFRM specimens, crack propagation dominantly occurs within the cementitious material; while in FR-ECC specimens except for Mix 4, crack propagates at the interface between the cementitious material and steel. **Fig.3.5** shows the representative condition of steel strips peeled off from control specimen, Mix 1, Mix 2 and Mix 4 after the adhesion test. It can be observed that for the control specimen, a relatively thick layer of cementitious material still adheres to the steel strip. For such material, the cohesive strength is very low; fracture failure within the SFRM material adjacent to the interface can be expected. In the case of Mix 1, apart from some spots, most of the area on the steel strip is clear of any cementitious residuals. This indicates that adhesive type of fracture occurs on the interface, which is quite different from the control specimen. Considering the fracture self-selects the plane requiring minimum energy for propagation, this adhesive fracture behavior reflects the influence of the higher cohesive (fracture toughness) property the FR-ECC (matrix) compare to the control SFRM specimen. For Mix 2, a very thin

layer of cementitious film remains adhered to the steel substrate, which shows that the adhesive property has been improved in Mix 2 by the addition of latex polymer. However, this film is very thin and not continuous throughout the contact area. Mix 4 behaves very differently from Mix 1 and 2 specimens; a relatively thick layer of cementitious material adheres onto the steel strips through most of the contact area. This clear cohesive failure indicates a further improvement of adhesion on the interface. In addition, the much higher  $G_c$  suggests that the interfacial transition zone is also enhanced compared to Mix 2.

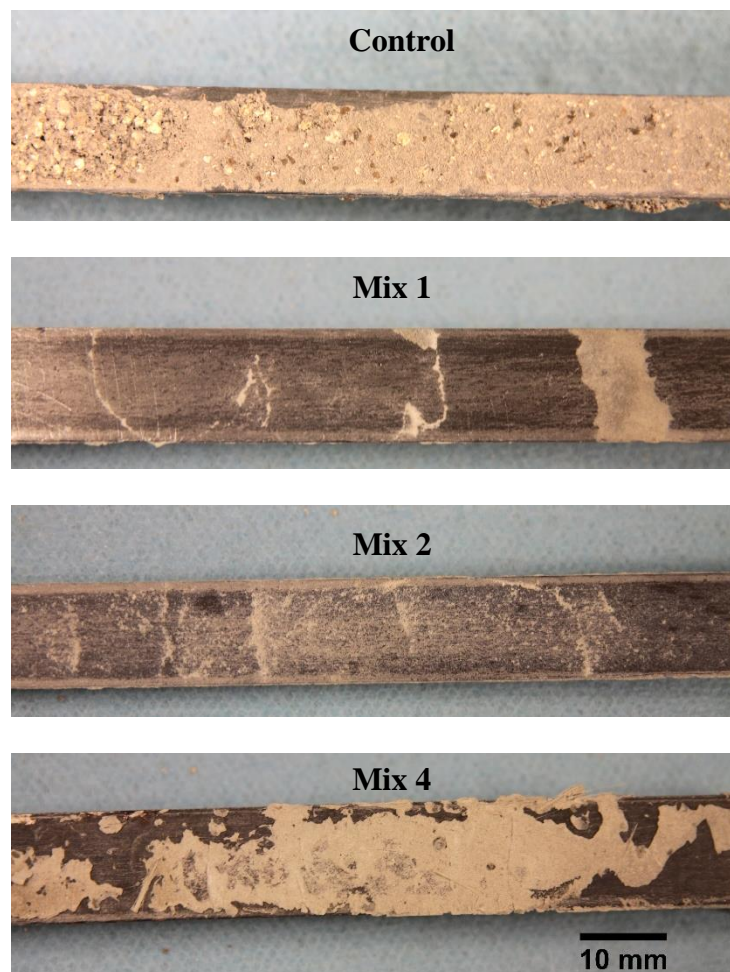


**Fig.3.5 The surface condition of peeled off steel strips from Mix 1, 2 and 4 is significantly different from that of control SFRM**

Failure on the interface is the dominant failure mode for FR-ECC (matrix) specimens, while cohesive failure is dominant in control SFRM specimens and Mix 4 specimen with bonding agent applied on steel surface. This also explains the larger variability in the test result of FR-ECC (matrix) specimens. Cohesion is an intrinsic material property while adhesion is an interfacial property, which is naturally subject to larger variability. It is demonstrated that higher interfacial bond as measured by  $G_c$  can be achieved 1) by enhancing the cohesive strength of the fire-resistive material (from SFRM to Mix 1), and 2) by enhancing the adhesive strength of the cohesively strong fire-resistive material/steel interface (from Mix 1 to Mix 2 and especially Mix 4).

### 3.3.2 Microstructure Investigation

The micrographs of the interfaces from the cementitious material sides are presented in **Fig.3.6**. The microstructure of the interfacial part is a weak interfacial transition zone (ITZ) similar to that between cement paste and aggregate.

**Fig.3.6(a)** shows a representative area of the interfacial layer of Mix 1 after the steel strip has been peeled off. On the left side of this image, a film formed right adjacent to the steel surface is visible, which covers most of the contact area of the specimen. It is a well-defined layer parallel to the steel surface even down to micron scale (**Fig.3.6(b)**). This film is a solid layer of roughly ten microns thick. Below that solid film layer, the more porous matrix is formed with a large volume fraction of glass bubbles. EDAX analysis on the general area of the solid film reveals that the calcium to silica (C/S) ratio is around 3.0, which is much larger than the common C/S ratio of C-S-H (1.5-2.0<sup>26</sup>). This indicates that it is a duplex film containing both C-S-H and C-H. Previous researchers<sup>27,28</sup> have also observed duplex films on the interface between cementitious material and other solid surfaces.

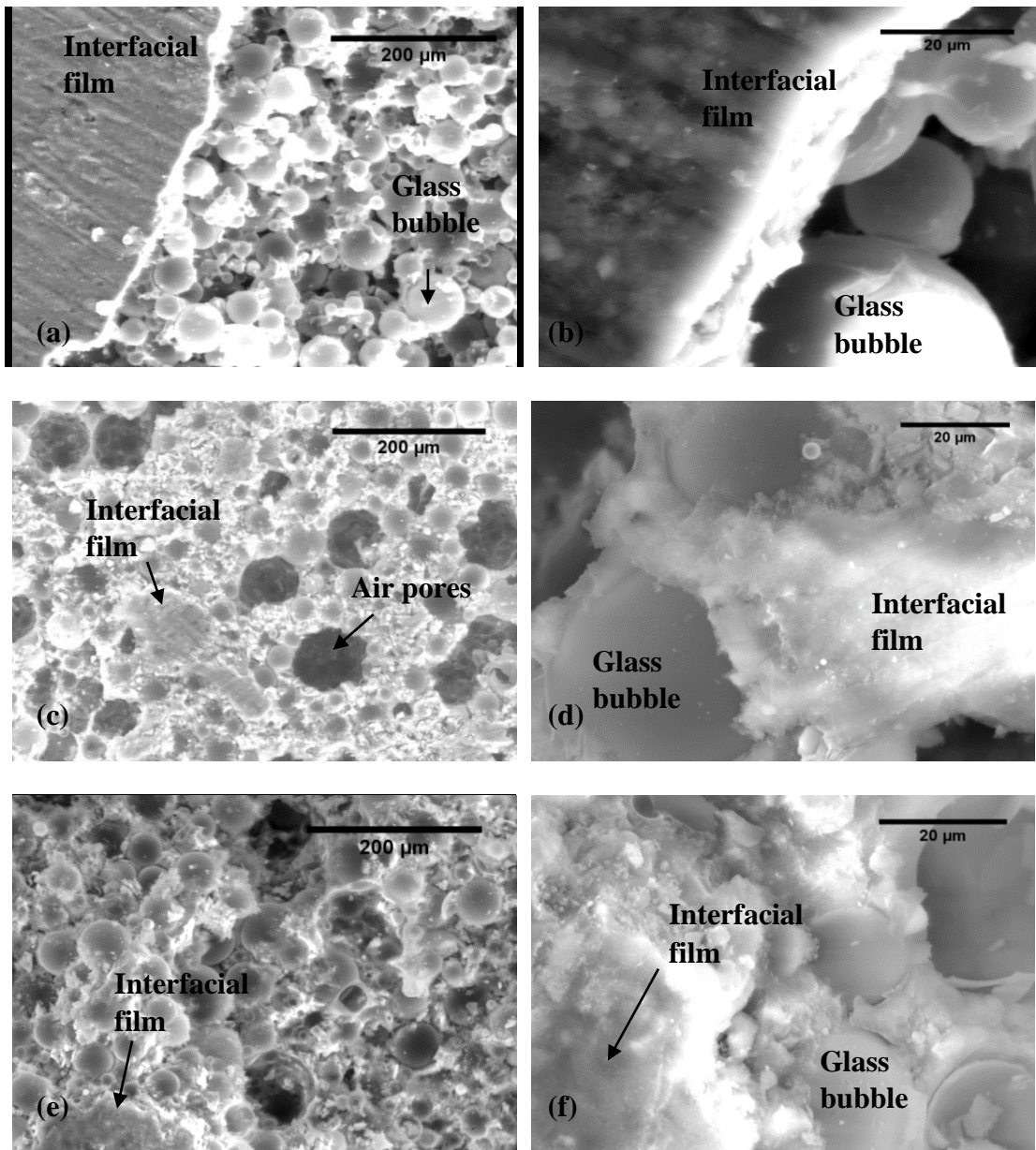


**Fig.3.6 SEM images of the interface (cementitious material side) of (a-b) Mix 1, (c-d) Mix 2, and (d-e) Mix 4**

**Fig.3.6(c)** shows the interfacial microstructure of Mix 2, which is Mix 1 modified by the addition of latex admixtures. From this figure, it can be observed that right adjacent to the interface, the solid layer was not continuous as in Mix 1 and most of the film has been peeled off during the

adhesion test, leaving a much more porous material surface when compared to that of Mix 1. EDAX analysis shows the C/S ratio of the film is 1.93. This ratio lies within the C-S-H range indicating less (or no) C-H formation on the interface. A possible explanation for such change in the composition of the interfacial film can be found in the literature. The interfacial film is formed due to two effects: wall effect and bleeding, which result in a higher effective water to cement ratio, larger crystals of hydrated products and lower bond strength.<sup>27,29,30</sup> However, it has also been reported that the presence of polymeric materials (latex) alters the state of flocculation/coagulation and reduces bleeding<sup>14</sup> which can reduce the local effective water/cement ratio. In addition, the introduction of polymer chains increases the viscosity of the solution reducing ions mobility and dissolution.<sup>14,31</sup> These modifications of the ITZ by latex polymer favor the formation of C-S-H adjacent to the steel surface.<sup>32</sup>

In addition, in **Fig.3.6(c)**, relatively large air pores with diameter up to 100 microns can be observed in the ITZ. The air pores are caused by the air entraining effect of latex emulsion during mixing. It can also be observed (**Fig.3.6(d)**) that a polymer-cement co-matrix formed between glass bubbles. This is expected to enhance the bond between the cement paste and the glass bubbles, and therefore the fracture resistance. In contrast, glass bubbles are loosely packed in the matrix adjacent to the interface in Mix 1 as shown in the zoomed-in image (**Fig.3.6(b)**).

**Fig.3.6(e)** presents the microstructure of the interface of Mix 4/steel. The fracture surface moves further away from the interfacial film. The interfacial film is similar to that of Mix 2. Also, this film is densely bonded with glass bubbles (**Fig.3.6(f)**) due to the high dosage of polymer bonding agent present on the interface. This enhancement extends to about 50  $\mu\text{m}$  away from the surface due to the penetration of the bonding agent and results in a deeper and more tortuous fracture surface. The localized latex polymer also alters the film composition. As analyzed by

EDAX, C/S ratio of this film is around 2.6, suggesting a duplex film with CH presence. This could be explained by the effect of polymeric material altering the flocculation and bleeding, together with the presence of high water content introduced by the latex emulsion.

The interfacial bond improvement with the use of latex admixture is associated with altering the interfacial layer composition and refinement of the porous ITZ. Further improvement can be expected by using anti-foaming agent along with latex admixtures to reduce the porosity of the mixture, especially in the ITZ. Applying the bonding agent directly on the surface alters the interfacial film composition, and enhanced the ITZ effectively without causing major air entraining effect. This is consistent with the highest adhesive bond  $G_c$  based on adhesive peel-off test reported in Section 3.3.1.

### 3.3.3 Mechanical Property

The compressive strength and uniaxial tensile stress-strain curves for Mix 1, 2 and 3 are plotted in **Fig.3.7** and **Fig.3.8**, respectively.

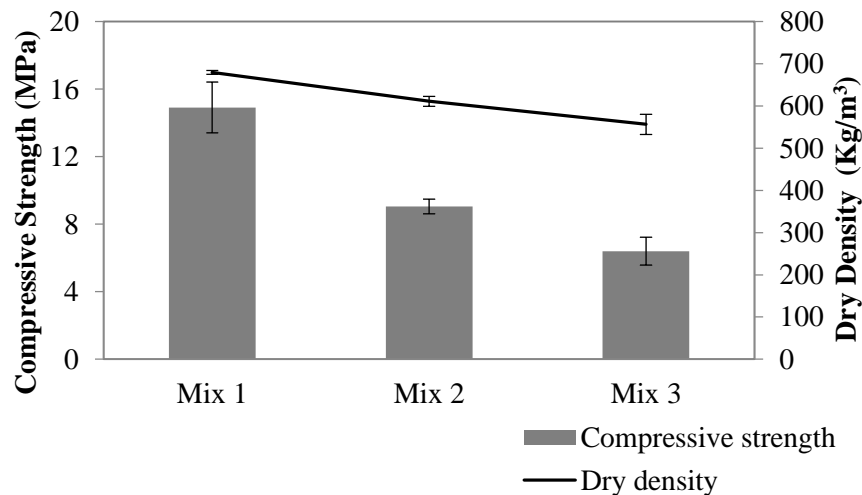


**Fig.3.7 Compressive strength and dry density of Mix 1, 2 and 3 decrease with increase in latex bonding agent dosage**



The compressive strength of the mixes under investigation decreases with increasing latex bonding agent dosage. This is mainly caused by the air entraining effect of latex bonding agent. The dry densities (measured at 28 days) of the mixes are also plotted in **Fig.3.7**. It can be observed that the dry-density also decreases as the latex dosage increases, which indicates increased air content within the mixes. The dry density trend agrees well with the compressive strength decrease. Another possibility is that the viscosity increases significantly with the latex modification, which may cause difficulties in the processing and casting process, and this could contribute to the presence of larger flaws in the high latex content mixes. Thus, the benefit of latex addition on adhesive bond property is offset by a reduction in compressive strength. Nevertheless the compressive strength of Mix 1, 2 and 3 are all considered sufficient since fire resistive materials are considered nonstructural.<sup>33,34</sup>

The tensile performance of FR-ECC is also affected by the latex admixture as shown in **Fig.3.8**. The first crack strength drops from 1.78 MPa to 1.58 MPa and 1.10 MPa from Mix 1 to Mix 2 and Mix 3. The first crack strength is governed by the largest flaw size and the fracture toughness of the mix. The fracture toughness of the mix is expected to increase with latex addition, associated with the polymer-cement co-matrix formation. However, the air entraining effect of latex also causes larger flaws within the material, resulting in a competing effect. As the results show, the air entrainment effect appears to dominate, leading to the observed decreasing trend of first crack strength with latex addition.

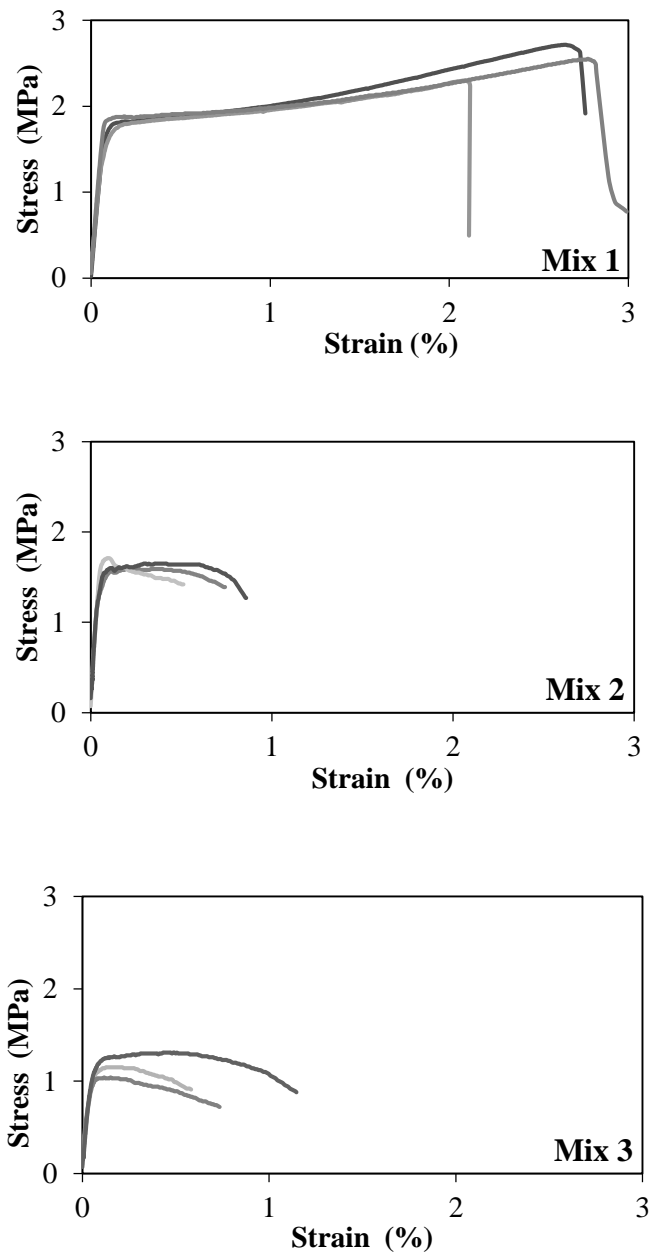


**Fig.3.8 Uniaxial tensile stress-strain curves of Mix 1, 2 and 3, showing the drastic reduction in tensile ductility with increase in bonding agent dosage**

The tensile ductility shows significant degradation with increased latex addition. From **Fig.3.8**, we can observe that Mix 1 shows very consistent strain hardening with average strain capacity of 2.57%. Mix 2 shows inconsistent strain hardening behavior with significantly less strain capacity (<1%) and even softening behavior. Mix 3 shows consistent softening behavior

featuring single crack opening. These phenomena might be associated with change in the interactions between matrix and fibers. The margin between the maximum fiber bridging stress  $\sigma_0$  and the matrix crack strength  $\sigma_{cs}$  is critical to the tensile behavior. At stress level between  $\sigma_{cs}$  and  $\sigma_0$ , matrix cracks at multiple locations. The micro crack opening is the dominant component of the strain capacity. The more crack opens, the large tensile ductility the material exhibits. A higher  $\sigma_0/\sigma_{cs}$  often allows more crack openings and is associated with higher tensile ductility. As shown in **Fig.3.8**, for Mix 2, the  $\sigma_0/\sigma_{cs}$  ratio is slightly higher than 1 in some specimens and below 1 in others. This lower margin is mainly attributed to a lower  $\sigma_0$  value. One plausible reason for this lower  $\sigma_0$  value is that the higher viscosity resulted from latex addition may have adversely affected the uniformity of the fiber dispersion and lead to lower fiber bridging capacity. Another plausible reason is a lower than intended fiber content due to the presence of air voids caused by the air entraining effect of latex admixtures; the 2% fiber content was calculated based on the rule of mixture without considering the air voids. The resulting lower  $\sigma_0/\sigma_{cs}$  could also explain the significant reduction in ductility from Mix 1 to Mix 2.

Artificial flaws were used in this study to recover the tensile ductility of Mix 2. Introduction of artificial flaws has been demonstrated to effectively enhance the multiple cracking behavior and improve the ductility of ECC mixes in a previous study<sup>35</sup>. In this study, 3% (by volume fraction) of polystyrene beads (**Fig.3.9**) of 4 mm size were added to the mix after adding the fiber. The uniaxial tensile test result of this modified mix is shown in **Fig.3.10**. The first crack strength drops slightly from 1.58 MPa to 1.53 MPa on average compared to Mix 2, which indicates that the natural pre-existing flaws in Mix 2 are slightly smaller than the beads. By adding the artificial flaws, a

larger margin between  $\sigma_0$  and  $\sigma_{cs}$  has been achieved. The relatively large flaws of similar size initiate a large number of cracks at small stress interval and result in an average strain capacity of 2.15%. **Fig.3.11** shows the crack pattern of the modified specimens. In these pictures, carbon black solution was applied to the specimen surface after the tensile test to improve the visibility of the cracks. The left figure depicts the saturated multiple fine cracks throughout the specimen length. The right figure shows typical micro cracks under optical microscope. The crack spacing is as narrow as 1 mm and the residual crack width is no more than 5  $\mu\text{m}$ . The desired tensile ductility is restored in Mix 2 adjusted with 3% volume fraction of polystyrene beads serving as artificial flaws.



**Fig.3.9 Polystyrene beads used as artificial flaws**

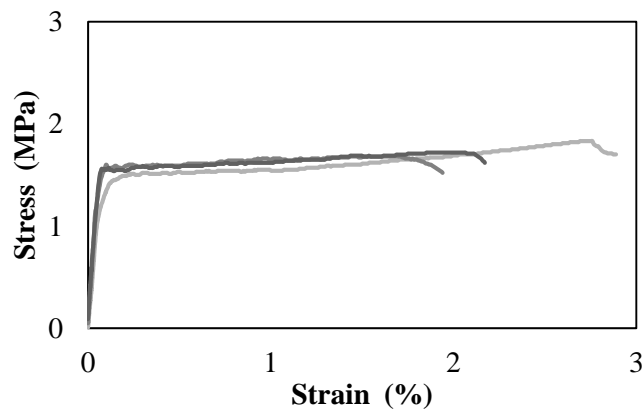


**Fig.3.10 Recovery of tensile ductility of Mix 2 by the addition of artificial flaws**

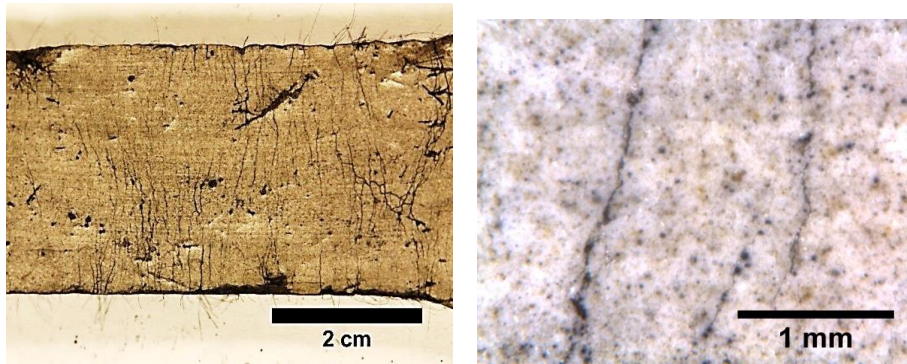


**Fig.3.11 Crack pattern of Mix 2 modified with artificial flaws**

Experiments were also conducted to confirm that other targeted properties of Mix 2 are not altered by the addition of artificial flaws. The compressive strength of the new mixture (Modified Mix 2) was measured to be  $8.00 \pm 0.34$  MPa with a dry density of  $575 \text{ kg/m}^3$ . The adhesion ( $G_c$ ) for the modified FR-ECC (with full 2% fiber content) was measured to be  $70.0 \pm 20.6 \text{ J/m}^2$  that is quite close to the unmodified Mix 2 (with  $G_c$  of  $69.6 \pm 36.9 \text{ J/m}^2$ ) with similar failure mechanism. Finally, the measured thermal conductivity (as detailed in Chapter 2) of modified Mix 2 does not show significant difference from the original mix (Mix 1) as shown in **Fig.3.12**. Therefore, the inclusion of polystyrene beads does not noticeably alter the other target properties.

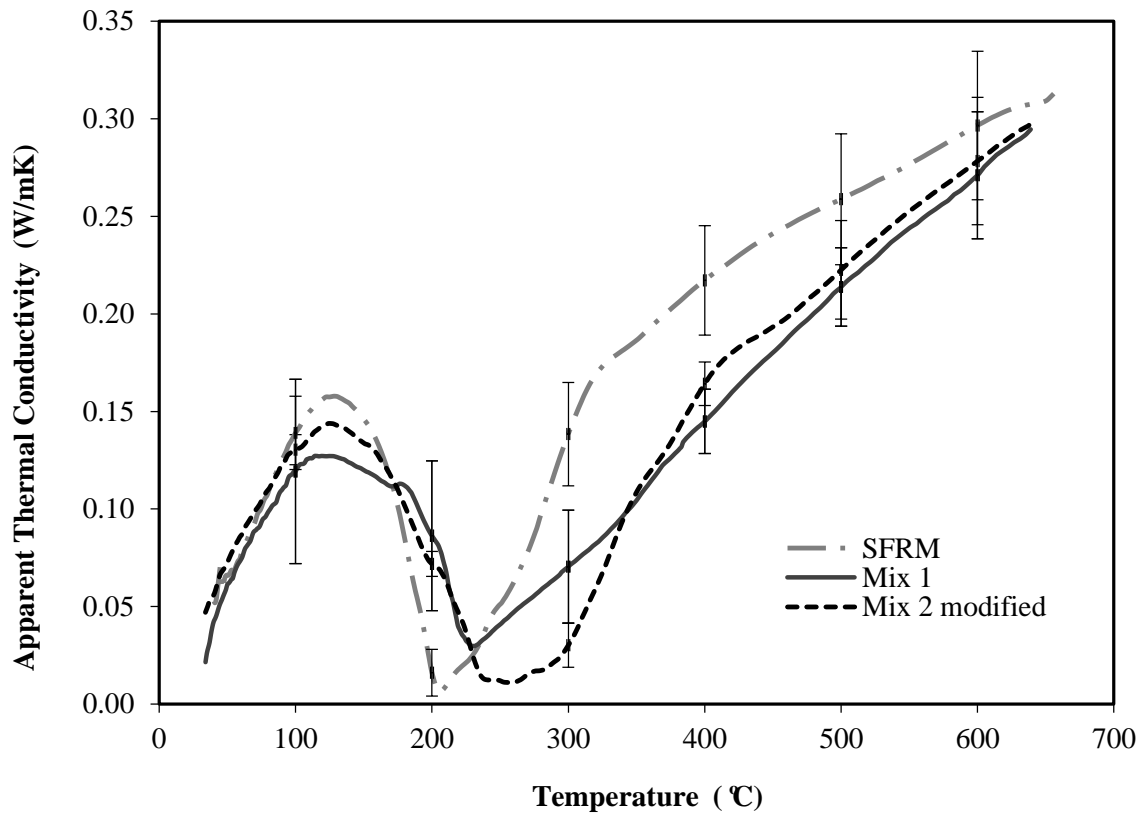


**Fig.3.12 Modified Mix 2 retains similar apparent thermal conductivity of unmodified FR-ECC (Mix 1)**

### 3.4 CONCLUSION

The following conclusions can be drawn based on the experimental findings documented in Chapter 3:

1. The apparent interfacial fracture energy of FR-ECC (matrix)/steel is measured to be 3 times higher than a conventional medium-density SFRM/steel, which tends to fail cohesively inside the SFRM near the interface. With significant increase in cohesive property of FR-ECC compared to SFRM, the failure mode was transformed to adhesive failure.
2. The hypothesis that latex bonding agent can enhance the FR-ECC/steel adhesive bond is experimentally confirmed. Latex bonding agent as admixtures is found to effectively

improve the interfacial adhesion energy between FR-ECC (matrix) and steel by 54%. Alternatively, directly applying the bonding agent on the steel surface results in a dramatic improvement of adhesion energy by 147%. The adhesive bond improvement was significant enough to drive the failure mode from dominantly adhesive failure back to cohesive failure in the FR-ECC.

3. The enhancement of interfacial adhesion with latex modification is attributed to a change in composition and microstructure of the ITZ between the FR-ECC (matrix) and steel, as confirmed by SEM with EDAX.
4. Latex polymer bonding agent as admixtures was found to reduce the tensile ductility and compressive strength of FR-ECC due to its notable air entraining effect. Nevertheless, the compressive strength of 6.40 MPa is within the acceptable range for fire-resistive materials.
5. The use of artificial flaws was found to be effective in restoring the tensile ductility of FR-ECC containing latex. This modified FR-ECC possesses remarkably improved mechanical properties (with compressive strength of 8.00 MPa, tensile strength of 1.75 MPa and tensile ductility of 2.15%) over conventional SFRM, while maintaining similar thermal conductivity. The adhesion energy  $G_c$  for the modified FR-ECC/steel was found to be  $70.0 \pm 20.6 \text{ J/m}^2$ , about 6.3 times that of SFRM/Steel at  $11.1 \text{ J/m}^2$ .

In this chapter, a complete study on the design process for high interfacial adhesion (to steel) of FR-ECC was conducted. This study provides valuable information for the parallel design process of the final version of SFR-ECC. In this chapter, an effective material engineering technique (using polymer latex) for enhancing the adhesive property (to steel) of FR-ECC was demonstrated. This technique therefore will be used in the further development of the final version of SFR-ECC in Chapter 4. In addition, the impacts of polymer latex addition on the mechanical

and thermal properties of FR-ECC were also studied. This provides the necessary knowledge for understanding the interdependencies between the design for high adhesion (to steel) and the design for other performance target in the proposed parallel design process.



## References

---

1. Li, G., and Kodur, V., "Role of Insulation Effectiveness on Fire Resistance of Steel Structures under Extreme Loading Events," *J. of Performance of Constructed Facilities*, 25(4), 2011.
2. ASTM E736-00(2011): Standard Test Method for Cohesion/Adhesion of Sprayed Fire-Resistive Materials Applied to Structural Members, ASTM International, West Conshohocken, PA, 2011, DOI: 10.1520/E0736-00R11, www.astm.org.
3. Tan, K.T., White C.C., and Hunston D.L., "An adhesion test method for spray-applied fire-resistive materials," *Fire and Materials*, 35, 245-259, 2011.
4. Bentz, D.P., White C.C., Prasad K.R., Flynn, D.R. Hunston, D.L., and Tan, K.T., "A materials science-based approach to characterizing fire resistive materials." *J. of ASTM Inter* 6, No. 5, 2009.
5. Nakayama, M. and Beaudoin, J.J., "Bond Strength Development Between Latex-Modified Cement Paste And Steel", *Cement and Concrete Research*, 17(4), 562-572, 1987.
6. Najm, H., Naaman, A.E. Chu, T-J. and Robertson, R.E., "Effects of poly(vinyl alcohol) on fiber cement interfaces. Part I: Bond stress-slip response", *Advanced Cement Based Materials*, 1(3), 115-121, 1994.
7. Gao, J.M., Qian, C.X., Wang, B. and Morino, K., "Experimental study on properties of polymer-modified cement mortars with silica fume", *Cement and Concrete Research* 32(1), 41-45, 2002.
8. Fu, X. and Chung, D.D.L., "Improving the bond strength between steel rebar and concrete by ozone treatment of rebar and polymer addition to concrete," *Cement and concrete research*, 27(5), 643-648, 1997.
9. Chew, M.Y.L., "Factors affecting ceramic tile adhesion for external cladding." *Construction and Building Materials* 13(5), 293-296, 1999.
10. Jenni, A., Holzer, L., Zurbriggen, R. and Herwegh, M., "Influence of polymers on microstructure and adhesive strength of cementitious tile adhesive mortars," *Cement and Concrete Research*, 35(1), 35-50, 2005.
11. Brien, J.V., and Mahboub, K.C., "Influence of polymer type on adhesion performance of a blended cement mortar," *International Journal of Adhesion and Adhesives*, 43, 7-13, 2013.
12. Su, Z., "Microstructure of polymer cement concrete", Delft University Press, Delft, The Netherlands, 1995.
13. Chandra, S., and Ohama, Y. "Polymers in concrete". CRC Press, Boca Raton, Fla., 1994.
14. Kim, J., Robertson, R.E., Naaman, A.E., "Structure and properties of poly(vinyl alcohol)-modified mortar and concrete", *Cement and Concrete Research*, 29 (3), 407-415, 1999.
15. Ohama, Y., and Ota, M., "Recent trends in research and development activities of polymer-modified paste, mortar and concrete in Japan," *Advanced Materials Research*, 687, 26-34, 2013.
16. Li, V. C., Wu, C., Wang, S., Ogawa, A, and Saito, T., "Interface Tailoring for Strain-Hardening Polyvinyl Alcohol-Engineered Cementitious Composites (PVA-ECC)," *ACI Materials J.*, 99(5), 463-472, 2002.
17. Kanda, T. and Li, V.C., "A New Micromechanics Design Theory for Pseudo Strain Hardening Cementitious Composite," *ASCE J. of Eng. Mechanics*, 125(4), 373-381, 1999.
18. Li, V. C., "Engineered Cementitious Composites – Tailored Composites through Micromechanical Modeling," *Fiber Reinforced Concrete: Present and the Future*, N. Banthia, A., Bentur, A. and Mufti, A., (ed.), Canadian Society for Civil Engineering, Montreal, Quebec, Canada, 64-97, 1998.

- 
19. Ohama, Y., "Handbook of polymer-modified concrete and mortars: properties and process technology", William Andrew, 1995.
  20. Ramakrishnan, V., "Properties and applications of latex-modified concrete," Advances in concrete technology, 2nd Ed., V. M. Malhotraed., Canada Ctr. for Mineral and Energy Technol., 839-890, 1994.
  21. Ohama, Y., "Polymer-based admixtures," Cement and concrete composites, 20(2), 189-212, 1998.
  22. Rossignolo, João A., and Marcos VC Agnesini., "Mechanical properties of polymer-modified lightweight aggregate concrete," Cement and Concrete Research, 32(3), 329-334, 2002.
  23. Song, S.H. and Liu, F.T., "Influences of Polymer Fiber and Polymer Latex on Physical Properties of Cement Mortar." Advanced Materials Research, 306, 814-818, 2011.
  24. ASTM Standard C109: Standard Test Method for Compressive Strength of Hydraulic Cement Mortars (Using 2-in. or [50-mm] Cube Specimens), Philadelphia, PA, 2002.
  25. JSCE: Recommendations for Design and Construction of High. Performance Fiber Reinforced Cement Composites with Multiple Fine Cracks (HPFRCC), March, 2008.
  26. Mindess, S., Young, F. and Darwin, D., Concrete (2nd ed.), 2003.
  27. Struble, L., "Microstructure and fracture at the cement paste-aggregate interface," In Proceedings of Symposium on Bonding in Cementitious Composites, Materials Research Society, Pittsburgh, 114, 11-20. 1988.
  28. Mansur, A.A.P., Santos, D.B. and Mansur. H.S., "A microstructural approach to adherence mechanism of poly (vinyl alcohol) modified cement systems to ceramic tiles." *Cement and concrete research* 37(2), 270-282, 2007.
  29. Kim, J. and Robertson, R.E., "Effect of polyvinyl alcohol on aggregate-paste bond strength and the interfacial transition zone", *Advanced Cement Based Material*, 8(2), 66-76, 1998.
  30. Mindess, S., "how important is it", *Bonding in Cementitious Composites*, Materials Research Society, Pittsburgh, 3-10, 1988.
  31. Su, Z., Bijen, J.M., Larbi, J.A., "Influence of polymer modification on the hydration of Portland cement", *Cement and Concrete Research*, 21 (2-3), 242-250, 1991
  32. Zhang, X., Groves, G.W., and Rodger, S.A., "The microstructure of cement aggregate interfaces", *Bonding in Cementitious Composites*, Materials Research Society, Pittsburgh, 89-95, 1988.
  33. UFGS- 07 81 00: Spray-applied fireproofing, February, 2011.
  34. ICC-ES, AC23: Acceptance Criteria for Spray-applied and Intumescent Mastic Coating Fire-protection Materials, 2011.
  35. Wang, S. and Li, V.C., "Tailoring of Pre-existing Flaws in ECC Matrix for Saturated Strain Hardening," *Proceedings of FRAMCOS-5*, Vail, Colorado, USA, 1005-1012, 2004.

## **CHAPTER 4 DEVELOPMENT AND CHARACTERIZATION OF SPRAY-APPLIED FIRE-RESISTIVE ENGINEERED CEMENTITIOUS COMPOSITES**

In this chapter, incorporating the discoveries in Chapter 2 and Chapter 3, Spray-applied fire-resistive ECC (SFR-ECC) was developed following the parallel design procedure. Material characterization was also conducted to confirm that SFR-ECC developed in this chapter met all the performance target regarding its functionality and durability properties.

### **4.1 INTRODUCTION**

In previous chapters, Fire-resistive ECC (FR-ECC) that combines thermal insulating property and high cohesive strength (facilitated by high tensile strength and ductility) has been developed. It has also been demonstrated that FR-ECC can be tailored to possess strong adhesion to steel. Therefore, FR-ECC exhibits substantially enhanced durability over the conventional SFRM.

Compared with the previous identified performance targets (listed in Chapter 1 section 1.2), the sprayability has not been achieved in the FR-ECC studied in Chapter 2 and 3. Sprayability offers versatility in construction and leads to reduced construction time and cost. Therefore, sprayability is highly desirable for such cement-based fire-resistive materials.

In this chapter, sprayability will be incorporated and spray-applied fire-resistive ECC (SFR-ECC) that satisfies all previously identified performance targets will be developed. As

described in Chapter 1, a parallel design process will be employed considering multiple design targets with the input from previous chapters.

A common technique to improve (or introduce) sprayability to the mixture is to incorporate vermiculites. Vermiculite is one of the most commonly used lightweight aggregates in conventional SFRM due to its low density (64-160 kg/m<sup>3</sup>), high water absorption (200-325% by weight and 20-50% by volume), low thermal conductivity (0.05-0.071 Wm<sup>-1</sup>K<sup>-1</sup>), high thermal stability, abundance in nature, and low cost. In addition to thermal and cost benefits, vermiculites, as aggregates, absorb and hold a large volume of water, which benefits the spraying process of SFRM. SFRM usually have very high water content so that it can be pumped to desired height and achieve high yield of material (lowering the cost). Vermiculites favors the spraying process by preventing segregation during the pumping process and prevent the mixture from being too watery when sprayed onto the steel. In addition, being non-abrasive, vermiculite will not cause additional frictional stress between the material and the hose during the pumping and spraying process, therefore it is well-suited for spray application. As a result, SFRM often use vermiculite to facilitate the application (low pressure spray) characteristics.

However, despite all the advantages of vermiculite, it has never been used as a constituent in ECC material before. Vermiculites are generally accordion-shaped granules. According to the micromechanics underlying ECC design,<sup>1,2</sup> such irregular shaped aggregates generally increase the matrix toughness that is undesirable for achieving strain-hardening behavior. Therefore adoption of vermiculite in ECC needs to be carefully experimented; the gradation and volume fraction of the vermiculite needs to be properly selected.

In addition to sprayability, incorporation of vermiculites as lightweight aggregates leads to reduced material cost. Vermiculites are of much lower cost compared to glass bubbles (and even fly ash cenospheres) used in previous FR-ECC. Lower material cost enhances the advantage of SFR-ECC over other passive protection materials (such as intumescent paints) and facilitates its broader adoption.

To further lower the material cost of SFR-ECC, high tenacity polypropylene (HTPP) fibers will also be incorporated into ECC as an economical alternative to PVA fibers. In a previous study conducted by Yang<sup>3</sup>, HTPP-ECC with ductility up to 4% and 2.5 MPa ultimate tensile strength were developed. A recent study by Felekoğlu et. al<sup>4</sup> further enhanced the robustness of HTPP-ECC material with controlled mixing and curing procedures. Some of the main drawbacks of HTPP fibers include lower tensile strength (800-900 MPa) and weak interfacial bond with cement, when compared with PVA fibers. In SFR-ECC design, the material is intrinsically of lower strength (compared to other structural ECC material), therefore, the use of HTPP fiber for SFR-ECC could be justified.

In this study, two mix design of spray-applied fire-resistive Engineered Cementitious Composite (SFR-ECC) have been developed. The mechanical properties of the resultant mixtures are evaluated by compressive test and direct uniaxial tensile test. Direct spray test is conducted to assess the sprayability of the newly developed materials. The thermal, mechanical and adhesive property of the sprayed material are characterized using thermal calorimetry (in accordance to ASTM E2584<sup>5</sup>), direct uniaxial tensile test and fracture energy based adhesion test<sup>6</sup>, respectively, to fully assess the in-situ performance of the material.

## 4.2 EXPERIMENTAL PROCEDURES

### 4.2.1 Material design

SFR-ECC material design involves simultaneous tailoring the material for multiple performance targets (low thermal conductivity, high tensile ductility, high adhesion to steel, and sprayability) in one mixture. There are many interrelated design parameters involved in this process as discovered in previous chapters. Designing for low thermal conductivity requires tailoring the microstructure of the material to possess high air void content and small air void size. This can be achieved by using porous or hollow lightweight aggregates in the mixture as found in Chapter 2. Designing for tensile ductility requires tailoring the fiber, matrix, and fiber/matrix interfacial micromechanical parameter of the mixture according to micromechanics<sup>7,8,9</sup>, including keeping the matrix toughness low and controlling the interfacial bond property between fiber and matrix for maximum bridging force but with minimum breakage. These considerations lead to using small-sized smooth-shaped aggregates that have less resistance to crack propagation, and carefully selecting the fiber type, geometry and content. Designing for high adhesion (to steel) involves modifying the cementitious material/steel interfacial transition zone and often requires adding polymeric admixtures into the mixture that might have side-effects on rheological and micromechanical characteristics as discovered in Chapter 3. Designing for sprayability involves controlling the rheology of the mixture<sup>10</sup>. This is often achieved by controlling the water content, chemical admixtures, aggregate absorption and geometry, using water holding and non-abrasive aggregates (e.g. vermiculites), and properly selecting the fiber content and geometry. To simultaneously attain the desired fresh property and mechanical and thermal properties of SFR-ECC, the interdependencies and potential conflicts highlighted above need to be taken into account in the design procedure.

Super fine grade vermiculite was used together with a small portion of glass bubbles or fly ash cenospheres as aggregates in the SFR-ECC mixture design. Vermiculite has an irregular concertina shape and a very porous structure, as shown in the micrograph in **Fig.4.1**. Superfine grade vermiculite was selected due to several considerations. The density, thermal property and water absorption of vermiculite all depend on the particle size. Smaller particle size is often associated with denser material and higher thermal conductivity which are less desirable. However, aggregate of smaller size limits the matrix toughness and, according to micromechanics underlying ECC design, is favorable for multiple cracking and strain hardening behavior. Smaller particles also have higher water absorption, which are preferred in fire-resistive materials. In addition, heat transfer theory indicates that smaller air voids are preferred to keep low radiation heat transfer at high temperature. Given the above considerations, the second finest grade vermiculite was chosen in this study. The particle distribution of the selected vermiculite is plotted in **Fig.4.2**. The measured water absorption is 214% by weight in accordance with ASTM C128<sup>11</sup>.

K25 glass microspheres having a density of 0.25 g/cm<sup>3</sup> and isostatic crush strength of 5.1 MPa were used in this study as a replacement of the previously used S38 glass bubble in the FR-ECC mixtures for economic efficiency. K25 are considered an economical alternative to the previously used S series 3M glass microspheres, which has the same composition and similar particle size. However, K25 has lower crush strength than S38 glass bubbles. The lower strength could be justified in nonstructural SFR-ECC application. The spherical-shaped glass bubbles are expected to improve the workability of the fresh mixture due to the ball bearing effect. They are also expected to effectively reduce the matrix toughness of designed SFR-ECC, which counterbalances the potential matrix toughness increase due to adoption of vermiculite.

Similarly, in another set of SFR-ECC mixtures, fly ash cenospheres (the same type as in Chapter 2) were also used

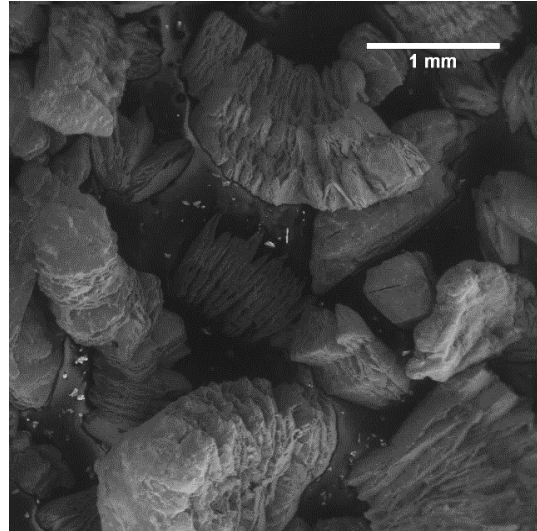


**Fig.4.1 Vermiculites have irregular shape and porous structure**

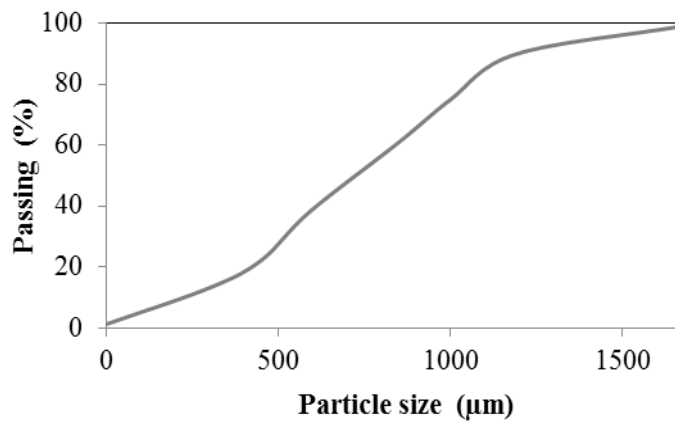


**Fig.4.2 Vermiculite particle size gradation**

Acrylic latex bonding agent, aimed at better adhesive properties to steel, was also used in the SFR-ECC mixture. In Chapter 2, it was demonstrated that adding latex bonding agent in the previous FR-ECC mixture significantly improves the adhesive energy between FR-ECC and steel. It is worth noting that the addition of bonding agent could alter the fresh and mechanical property



of the SFR-ECC material. As a result, the effect of acrylic latex bonding agent in the present SFR-ECC mix design needs to be carefully examined.

High Tenacity Polypropylene (HTPP) fibers are used in SFR-ECC mixtures. According to micromechanics, in order to achieve strain-hardening behavior, certain balance between the matrix property and the fiber bridging property needs to be met as discussed in Chapter 1. The fiber bridging property is closely associated with the fiber strength, elastic modulus and its bond to the cementitious matrix. Based on past experience with ECC, it is easier to achieve such balance with polymer fibers. ECC have been successfully developed with polyethylene (PE), poly vinyl alcohol (PVA) and polypropylene (PP) fibers. As previously discussed, this study mainly focuses on enhancing the durability of the passive fire protection material under ambient temperature, using polymer fibers with low melting temperature is then considered acceptable. Among the above mentioned polymer fibers, HTPP fibers are selected for economic reason. HTPP fibers, compared to PVA fiber typically used in regular ECC mixes, are of significantly lower cost (over 50% lower). HTPP fibers have lower strength than PVA fibers, however, since SFR-ECC has much lower strength requirement than that of regular density ECC material, HTPP fibers are therefore considered suitable in this application.

Based on the above considerations, three mixtures were designed as listed in **Table 4.1**. Vermiculites and glass bubbles (GB) were used as aggregates in Mix 1-3. Vermiculites and fly ash cenospheres (FAC) were used in Mix 4-5. Mix 1 has a lower glass bubble content than Mix 2 and 3, while Mix 2 has an acrylic dosage double that of Mix 3. Similarly, based on the experience with Mix 1-3, Mix 4-5 was designed. The fly ash cenospheres contents (by volume) in Mix 4 and 5 were designed to be similar to the content of glass bubbles in Mix 2 and 3. However, the water and

bonding agent dosage were slightly modified in Mix 5. All three mixes contain 1.5% (by volume fraction) HTPP fiber and the same amount of vermiculite (0.3 weight ratio of cement).

**Table 4.1 Mix details of SFR-ECC**

Mix ID	Cement	Water	Bonding Agent	Vermiculite	GB or FAC
1	1	1.08	0.12	0.3	0.125 (GB)
2	1	1.08	0.12	0.3	0.2 (GB)
3	1	1.14	0.06	0.3	0.2 (GB)
4	1	1.08	0.12	0.3	0.8 (FAC)
5	1	1.33	0.07	0.3	0.8 (FAC)

#### **4.2.2 Specimen preparation and testing**

The direct tension tests of the mixtures were conducted using the uniaxial tension test setup on a set of three dog-bone shape specimens in accordance with Recommendations for Direct Tension Testing of High Performance Fiber Reinforced Cementitious Composites by Japan Society of Civil Engineers<sup>12</sup>. The dog-bone shape specimens were tested on a load frame with 20 kN capacity, under a displacement control at the rate of 0.5 mm/min. Two external linear variable differential transducers (LVDTs) were attached to the specimen edges, with a gage length of approximately 101.6 mm, to measure the tensile strain.

Compressive strength of the mixtures was measured using a set of three cube specimens of side 50.8 mm. The test was conducted using a compression load frame at a loading rate of 1300±300 N/sec in accordance with ASTM C109<sup>13</sup>.

In the above studies, the mixing procedure follows that in Felekoğlu et. al<sup>4</sup> suggested for ECC with HTPP fibers, and the mixtures were cast into the desired specimen configuration.

Direct spray test were conducted to characterize the sprayability of the developed mixtures. A wet spray procedure was used to ensure proper fiber dispersion. After mixing, the fresh mix was pumped through a peristaltic pump connected to the spraying gun, and sprayed out. It is suggested

that peristaltic pump works well with fiber reinforced materials without fiber clumping as the pump is designed for pumping more viscous mixtures. A mill surface structural steel substrate of 914mm x 305mm x 12.7mm was placed vertically on the ground. The substrate was cleaned with alcohol prior to the spray test in order to remove the oil and dirt on the surface. During the low pressure spraying process, fresh SFR-ECC were sprayed onto the steel substrate and gradually built up. When the material started to fall off and could not build up further, the spray test was aborted and the maximum thickness was measured as the initial built-up thickness. Allowing the applied material setting for a period of time (24 hours in this study), a second spray was performed to further increase the built-up thickness. The total thickness built up after the second application was measured and recorded. The combined thicknesses of the two pass sprays were used to characterize the sprayability of the mixture.

To assess the in-situ properties of the sprayed SFR-ECC, specimens were cut from the sprayed material and tested for their thermal and tensile properties. Thermal conductivity measurements were conducted on plate specimens of 152.4 mm x 152.4mm x 25.4mm using a thermal capacitance calorimeter in accordance with ASTM E2584<sup>5</sup>. The detailed test procedure was adopted from that described in Chapter 2 with slight modification. Instead of a pair of specimens, only one specimen was used. The other side of the slug was covered by insulation. This modification was made to eliminate the effect of unevenly distributed temperature within the small furnace. The test configuration is shown in **Fig.4.3**. A type of commercially available medium-density Portland cement based SFRM was used as control to evaluate the thermal conductivity of SFR-ECC.

The tensile property of sprayed SFR-ECC was characterized by uniaxial direct tension test on coupon specimens of 203.2mm x 76.2mm x 12.7mm that were cut from the sprayed material.

Coupon specimens were used since it was very difficult to cut dogbone shaped specimens out of the sprayed material. Other than the specimen geometry, all test parameters were kept the same as the test on cast material.

As another key durability characteristic, the adhesion between SFR-ECC and structural steel were also characterized using an energy-based adhesion test method developed at NIST<sup>6</sup>; the detailed test procedure was documented in Chapter 3. In this chapter, the SFR-ECC were sprayed-applied into the box molds onto the structural steel strips (approximately 13 mm wide, 1.3 mm thick and 250 mm long) placed at the bottom of the molds (as shown in **Fig.3.2**). During the experiment, structural steel strips that were bonded to the SFR-ECC were peeled off by lifting one end. The load and corresponding interfacial crack length were recorded. Fracture resistance R-curves were then constructed. The adhesion is characterized by the steady-state critical energy release rate of the interfacial fracture, which is the plateau value of the R-curve. Again, the same medium-density conventional SFRM was used as control.

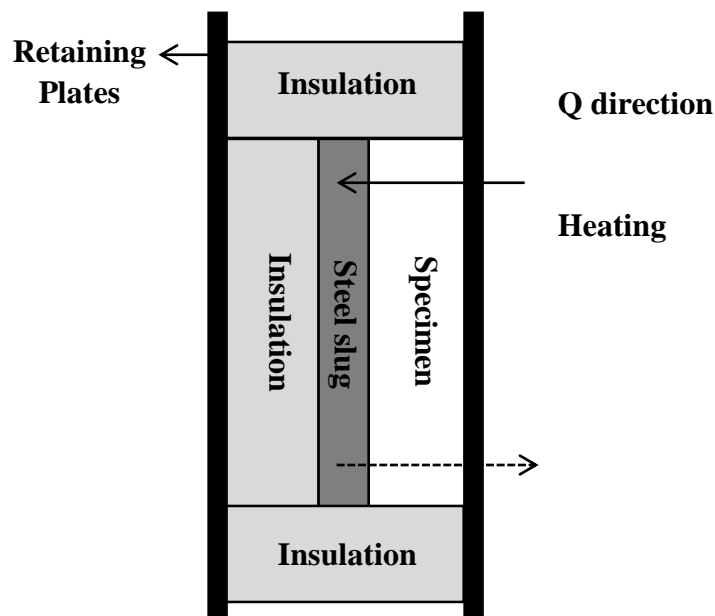


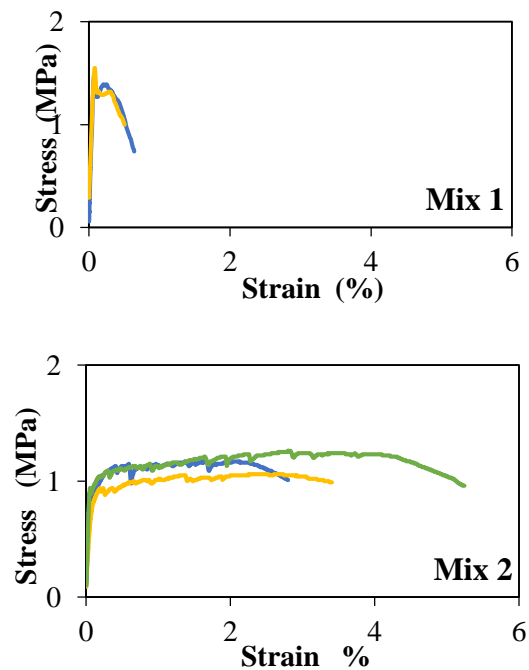
**Fig.4.3 Schematics of assembled single specimen for thermal conductivity test**

All specimens were tested at the age of 28 days after curing under laboratory room conditions ( $23 \pm 3$  °C;  $30 \pm 10\%$  RH).

## 4.3 RESULTS AND DISCUSSION

### 4.3.1 Mechanical property of Cast Material

The tensile test results of Mix 1-3 are plotted in **Fig.4.4**. Mix 2 and 3 exhibit robust strain hardening behavior with substantial tensile strain capacity (greater than 1.5%). Mix 2 has an average tensile strain capacity as high as 3.0%, which is about 300 times that of typical cement-based material. Mix 1 shows a strain softening behavior with significantly less tensile ductility. The reason behind the different behaviors is rooted in the micromechanics underlying ECC design.



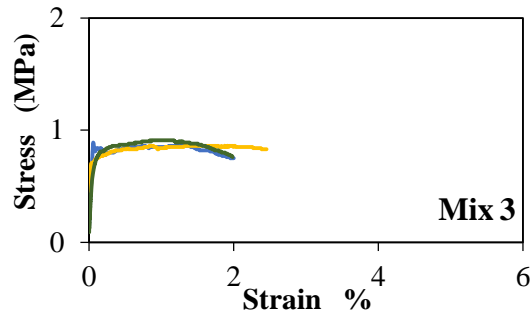


**Fig.4.4 Uniaxial tensile behavior of the cast Mix 1-3**

The first crack strength of the three mixes are shown in **Fig.4.5**. First crack strength is governed by the matrix toughness and largest flaw size. **Fig.4.5** clearly shows the decreasing trend of first crack strength with increasing glass bubble content (from Mix 1 to Mix 2/3). Glass bubbles, with spherical shape and micron scale diameter, have less resistance to crack propagation and therefore lower the matrix toughness, resulting in lower first crack strength. This is favorable for achieving the desired multiple cracking and strain hardening behavior. Comparing Mix 2 and Mix 3, the acrylic latex bonding agent dosage does not show significant influence on the first crack strength. This could be due to the combined effect of air entrainment (which alters the flaw size) and enhanced matrix fracture toughness (associated with the formation of cement-polymer co-matrix).

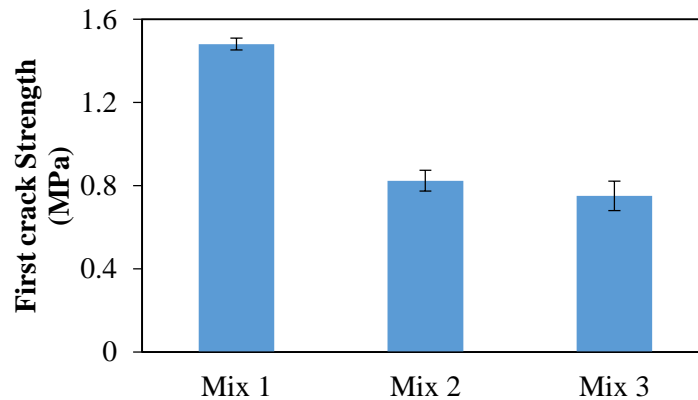


**Fig.4.5 Mix 2 and 3 with higher glass bubble content shows lower first crack strength**

The tensile ductility also depends on the fiber/matrix interfacial property. The ultimate tensile strength in ECC is closely associated with and serves as a good indicator of the interfacial property. The acrylic latex dosage greatly affects the ultimate tensile strength of the mixtures as shown in the comparison between Mix 2 and 3 in **Fig.4.4**. The increasing acrylic latex dosage (from Mix 3 to Mix 2) noticeably increases the ultimate tensile strength (from 0.87 MPa to 1.17 MPa). The larger margin between the ultimate tensile strength and first crack strength is favorable for strain hardening behavior and leads to a higher tensile ductility. This is also confirmed with the tensile behavior of the mixtures, which shows that Mix 2 has a significantly larger tensile strain capacity than Mix 3. Based on above discussion, Mix 2 seems to be the most promising candidate among the three mixes with glass bubbles for SFR-ECC and will be investigated in the following sections for its compressive strength, sprayability and in-situ performance.

For mixes with fly ash cenospheres, the tensile behavior of Mix 4 and Mix 5 are plotted in **Fig.4.6**. Mix 4 is almost identical to Mix 2 except that the glass bubbles (in Mix 2) were replaced by slightly higher volume fraction of fly ash cenospheres. Compared with Mix 2, Mix 4 shows similar first cracking strength but lower ultimate tensile strength, resulting in a lower tensile ductility. This is mainly due to the fact that Mix 4 has a lower workability than Mix 2. The fly ash cenospheres absorbs more water during mixing compared to glass bubbles, making the fresh mix less workable. Fly ash cenospheres, as an industrial waste material, has less smoothness and less controlled shape and size, compared to manufactured product glass bubbles, therefore, the benefit of fly ash cenospheres for improving workability (due to ball-bearing effect) is less significant than that of the glass bubbles. The poor workability of Mix 4 could result in less uniform fiber distribution and lower ultimate tensile strength (governed by fiber bridging strength). In addition, the poor workability of Mix 4 made it impossible to pump and spray.

Mix 5 was modified to have high water content and lower bonding agent dosage to improve the workability of the fresh mix. As shown in **Fig.4.6**, Mix 5 shows more ductile behavior with tensile strain capacity of (2.2%) compared to Mix 4 (1.8%). The ultimate tensile strength is measured to be 0.67 MPa, lower than that of Mix 4 (0.91 MPa) and Mix 2 (1.17 MPa). The strength reduction is strongly related to the increasing water/cement ratio. However, the tensile strength is still considered high in the context of SFRM. As a reference, normal SFRM of similar density range exhibit tensile strength around 0.1 MPa.<sup>14</sup> In addition, the better workability of Mix 5 made it possible for spray applications. Therefore, Mix 5 is considered of better performance than Mix 4 and therefore will be investigated in the following sections for its compressive strength, sprayability and in-situ performance.

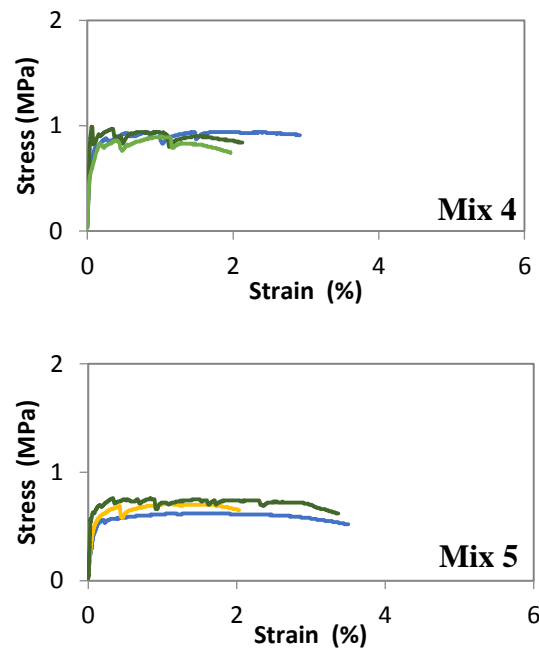


**Fig.4.6 Uniaxial tensile behavior of the cast Mix 4-5**

The compressive strengths of Mix 2 and Mix 5 are measured to be  $3.46 \pm 0.2$  MPa and  $3.3 \pm 0.28$  MPa, respectively. The dry density measured at 28 day are  $550 \text{ kg/m}^3$  for Mix 2 and  $600$



kg/m<sup>3</sup> for Mix 5. With such density, SFR-ECC mixes can be classified as medium density (352-640 kg/m<sup>3</sup>) SFRM. The compressive strength of Mix 2 and Mix 5 well exceed the requirement for SFRM of medium density in various specifications.<sup>15,16</sup>

It is also noticed that SFR-ECC exhibits cellular-like behavior under compression. The typical stress-strain curve of SFR-ECC (Mix 2) under compression is plotted in **Fig.4.7**. After the linear elastic stage, the stress–strain curve plateaus and then the stress starts to increase sharply at large deformation. During the compression test, the specimens were compressed all the way into a disk shape. This is typically found in metal/synthetic foam materials with porous or cellular structure. SFR-ECC possesses a very porous microstructure with large amount of air voids and pores inside the vermiculites, glass bubbles or fly ash cenospheres. However, the foam behavior under compression is not typically found in cementitious materials, since the cement-based material typically fails in brittle fracture. This unique behavior of SFR-ECC is found to be a result of the unique pore structure and fiber reinforcement that significantly toughens and confines the matrix. The details can be found in the microscopic study documented in Chapter 5.

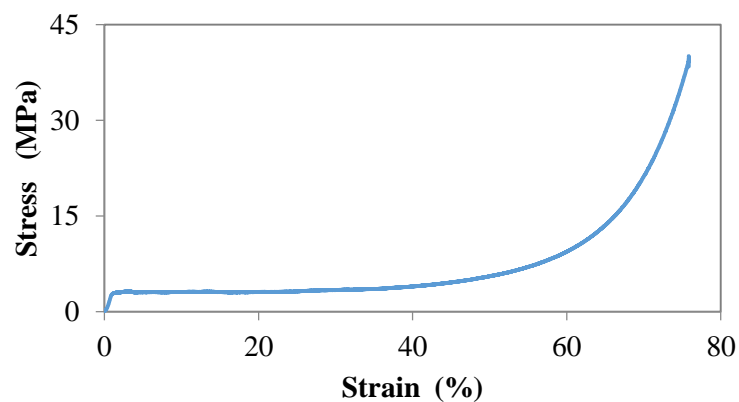


**Fig.4.7 Compressive stress-strain curve of SFR-ECC (Mix 2) indicating foam behavior**

Compared with the FR-ECC studied in previous chapters, the newly developed SFR-ECC exhibit lower density, strength and similar tensile ductility. The incorporation of vermiculites and HTPP fibers contribute towards the reduced compressive strength and tensile strength of SFR-ECC. However, by carefully tailoring the material according to micromechanics, the tensile ductility of SFR-ECC is maintained. In addition, the strengths of SFR-ECC is still considered satisfactory for medium density SFRM. In particular, SFR-ECC developed with glass bubbles (Mix 2) even satisfies the compressive strength criterion for high density SFRM (with density greater than  $640 \text{ kg/m}^3$ ). SFR-ECC still maintains its advantage in mechanical property over SFRM.

#### **4.3.2 Sprayability characterization**

Sprayability is an important functionality associated with the construction phase of SFRM type of material. Sufficient build-up thickness for each pass is critical to ensure a feasible construction schedule. The direct spray test shows that for both Mix 2 and Mix 5, a maximum built-up thickness of 10-15 mm (Mix 2) and 15-20 mm (Mix 5) can be achieved in a first spray application. Another 30 mm can be built up in a consecutive spray application after the first layer has been dried (after 24 hours in this study). The final maximum build-up thickness after two sprays adds up to 40-45 mm for Mix 2 and 60mm for Mix 5 as shown in **Fig.4.8**. The typical thickness of SFRM used for steel structures is 10-50 mm which is often achieved by multiple sprays. The built up thickness of SFR-ECC is therefore acceptable for field application; SFR-ECC offers ease of construction similarly to conventional SFRM.

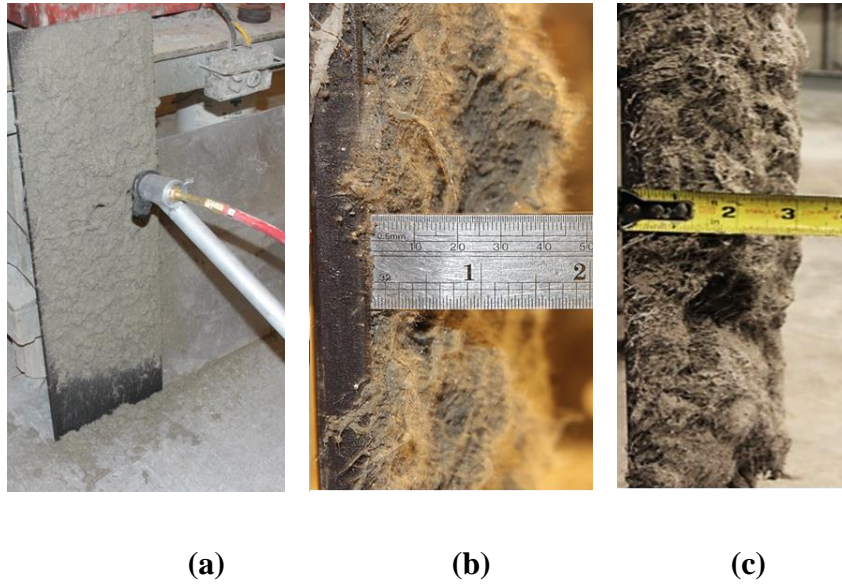


**Fig.4.8 Direct spray test (a) shows that SFR-ECC can build up to 40-45mm for (b) Mix 2 and 60 mm for (c) Mix 5 in 2 sprays**

#### **4.3.3 Performance of sprayed material**

Although cast SFR-ECC exhibits satisfactory mechanical performance, how the material is applied (cast versus sprayed) might affect the performance of the in-situ SFR-ECC. SFR-ECC is designed for low pressure spray application. The spray process could alter the microstructure of the material and how the fiber disperses within the mixture. Two key characteristics: tensile ductility and thermal conductivity are particularly sensitive to changes in material microstructure. As a result, the SFR-ECC needs to be characterized using spray-applied specimens to ensure meeting the performance targets.

The tensile stress-strain curves of sprayed SFR-ECC Mix 2 and Mix 5 are plotted in **Fig.4.9**. As shown in the figure, the sprayed SFR-ECC maintained significant tensile ductility. However, the tensile strain capacity of this sprayed version is noticeably lower than that of the cast version of the same mix (as shown in **Fig.4.4** and **Fig.4.6**). The difference between the tensile behavior of

cast and sprayed specimens could be associated with the differences in fiber orientation and fiber dispersion between the two methods of placing the material.

For SFR-ECC Mix 2, by comparing **Fig.4.9** with **Fig.4.4**, it is clear that the ultimate tensile strength of sprayed SFR-ECC Mix 2 is lower than that of the cast version, while the first crack strengths are quite similar. The first crack strength is closely associated with the matrix properties, including the matrix toughness and flaw size distribution. The consistent first crack strength indicates that the spray process has limited influence on the matrix property.

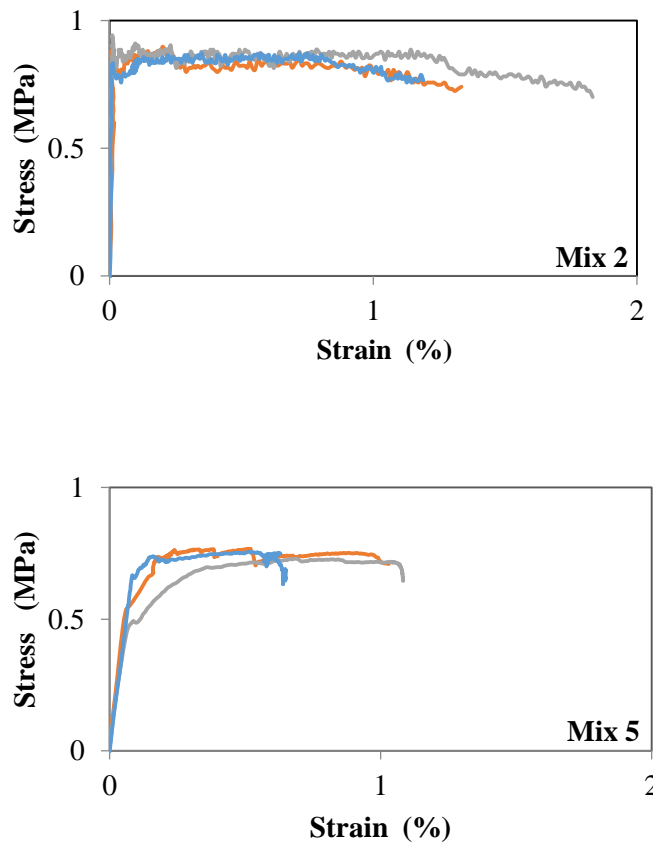


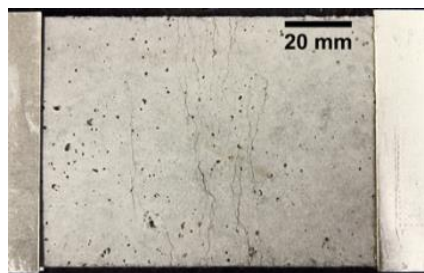
**Fig.4.9 Sprayed SFR-ECC maintains substantial ductility**

The reduced tensile ductility in SFR-ECC is closely associated with the reduced ultimate tensile strength. These reductions are most likely due to the change in fiber orientation in sprayed specimens compared to cast specimens. In cast specimens, due to the restraint of the mold edges,

the fiber tends to orient towards the longitudinal directions, which could result in a higher fiber bridging capacity in this direction. However, due to the nature of low pressure spray, the fibers in SFR-ECC is expected to have a 2-D random distribution. This could lead to a reduced fiber bridging capacity in the loading direction compared to that of cast specimens. The reduced ultimate tensile strength leads to a reduced margin between first crack strength and ultimate tensile strength, which is associated with the noticeably diminished multiple cracking (**Fig.4.10**) and reduced tensile ductility. Potential modifications to further improve the strain capacity include increasing the fiber content, for example, from 1.5% to 2%, or increasing the acrylic latex dosage. Nevertheless, the average tensile strain capacity of sprayed Mix 2 still reaches 1.0%, which is about 100 times larger than conventional SFRM.



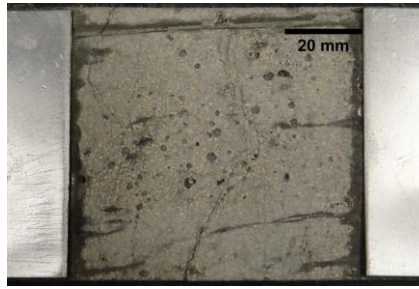
(a)



(b)



(c)

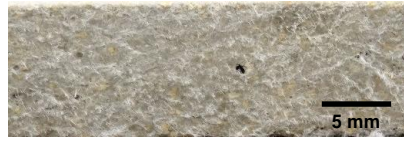


(d)

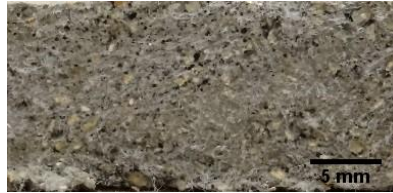
**Fig.4.10 Different multiple cracking behavior between cast specimens and sprayed specimens;**

**(a) casted Mix 2; (b) sprayed Mix 2; (c) casted Mix 5; and (d) sprayed Mix 5**

The tensile ductility of SFR-ECC Mix 5 also decreases from cast specimens (2.2%) to sprayed specimens (0.9%) with significantly less multiple cracking (**Fig.4.10**). However, the ultimate tensile strength of Mix 5 was not reduced due to the spray process, which is different from the case of Mix 2. Slightly higher first cracking strength was observed in sprayed specimens compared to cast specimen. This might be associated with the matrix being compacted during the spray process. This was not noticed for Mix 2, which might indicate better sprayability of SFR-ECC Mix 2. For SFR-ECC Mix 5, there were less flaws observed in the sprayed specimens (**Fig.4.11**) due to the compactness of the matrix, which could lead to less cracks under tension. This could contribute to the reduced tensile ductility. In addition, the reduced margin between first cracking strength and ultimate tensile strength also contribute towards reduced tensile ductility according to ECC micromechanical model. The reduced margin could be associated with matrix being compacted (resulting in higher first cracking strength and ultimate tensile strength) and the change of fiber orientation distribution (resulting in lower ultimate tensile strength) in sprayed specimens. Nevertheless, the tensile ductility of sprayed SFR-ECC Mix 5 is still considered very high compared to conventional SFRM.



(a)



(b)

**Fig.4.11 (a) Sprayed SFR-ECC (Mix 5) has less large flaws than (b) cast SFR-ECC specimen (Mix 5)**

Thermal property is the core functionality characteristic for SFR-ECC. Low thermal conductivity is the core requirement of these lightweight cementitious fire-resistive materials. The measured apparent thermal conductivity of sprayed SFR-ECC as a function of temperature is plotted in **Fig.4.12**. As a comparison, a medium-density conventional SFRM was also characterized as control specimens. The thermal conductivity of SFR-ECC is comparable to conventional SFRM over the investigated temperature range. The fire resistance of cementitious fire resistive materials mainly comes from their low thermal conductivity that delays the temperature rise in the steel structures. The comparable thermal conductivity of SFR-ECC and control SFRM suggests that the two materials have similar fire resistance (for the same thickness).

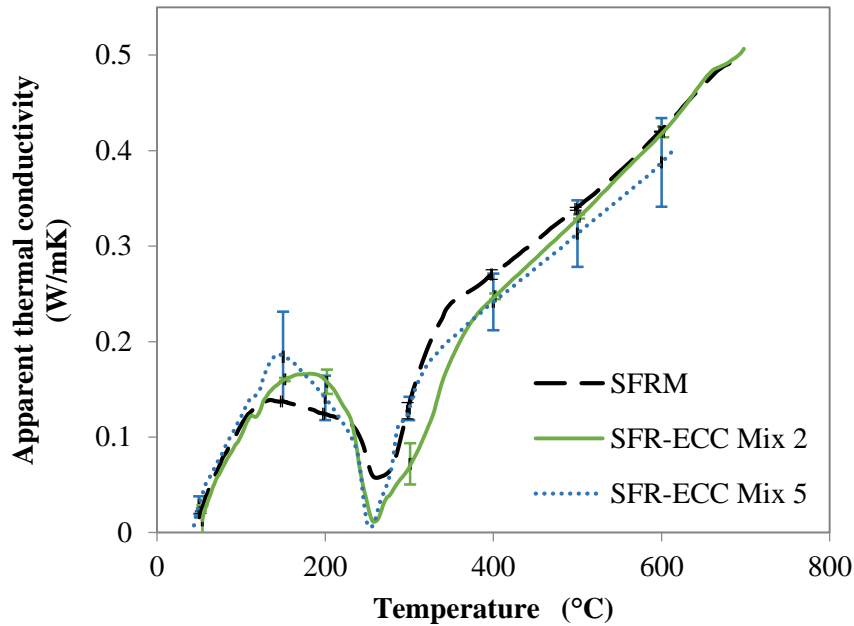


**Fig.4.12 Comparable apparent thermal conductivity of SFR-ECC to SFRM**

The measured adhesive fracture energy of SFR-ECC Mix 2 and Mix 5 (to structural steel) at 28 day are  $104.3 \pm 15.4 \text{ J/m}^2$  and  $310.4 \pm 45.3 \text{ J/m}^2$ , about an order of magnitude higher than that of conventional medium-density SFRM used as control specimen in this study ( $11.1 \pm 1.4 \text{ J/m}^2$ ). For both SFR-ECC and control SFRM, fracture occurs within the cementitious material adjacent to the interface, thus a cohesive type of failure. For SFR-ECC, the HTPP fibers actually bridge across the delaminating crack (as shown in **Fig. 4.13**) and SFR-ECC/steel “interface” exhibits a ductile fracture behavior with a rising R-curve. While SFRM/steel interface exhibits a typical brittle fracture behavior with a flat R-curve. For SFR-ECC, due to the large process zone and dimension limit of the specimen, the true steady-state critical energy release rate (plateau value of R-curve) was not reached; the adhesion energy was conservatively calculated as an average value measured between 150-200 mm crack length instead of the true plateau value for conservative and realistic considerations.

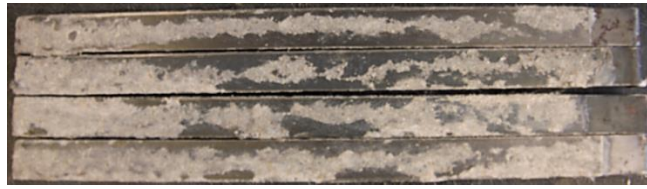


The high adhesive property of SFR-ECC comes from both enhanced adhesion due to polymeric latex addition and enhanced cohesion due to fiber bridging. Considering that the delaminating crack self-selects the plane requiring minimum energy for propagation, the cohesive type of fracture within the SFR-ECC suggests that SFR-ECC possesses sufficient adhesion (right at the interface) to the steel substrate, possibly due to its polymeric latex modification. In addition to the high interfacial adhesion, the fibers bridging across the fracture surface also greatly increases the energy required to drive the crack propagation. This is also reflected in the adhesion measurement.

Comparing Mix 2 and Mix 5, Mix 5 exhibit higher interfacial adhesion. **Fig.4.14** shows the condition of the steel strips there were peeled off from the SFR-ECC. It can be observed that there were more areas covered with SFR-ECC on the strips peeled off from SFR-ECC Mix 5. Due to the fiber bridging effect, such fracture requires much higher energy. That explains the higher adhesive energy of SFR-ECC Mix 5 (to steel). This could be associated with the compacting of the material during spraying, which could possibly densify the interfacial transition zone between SFR-ECC (Mix 5) and steel substrate. The significantly higher adhesive property of SFR-ECC compared to conventional SFRM helps to resist delamination of fire insulation under various loading conditions and contributes to enhanced durability of SFR-ECC fire protection system.



**Fig.4.13** Fibers bridge across the interfacial crack between steel and SFR-ECC



(a)



(b)

**Fig.4.14 Steel strips peeled off from SFR-ECC (a) Mix 2; (b) Mix 5**

#### **4.4 CONCLUSION**

Based on above findings in this chapter, it is concluded that the proposed SFR-ECC have been successfully developed following parallel design process and the resultant SFR-ECC should contribute to enhanced fire safety of steel structures due to enhanced durability over SFRM. Specifically the following conclusions are drawn:

1. Cast SFR-ECC with dry density of  $550\text{kg/m}^3$ , and tensile strength up to 1.1 MPa and strain capacity up to 3.0% that are one to two orders of magnitude higher than those of SFRM, has been developed incorporating vermiculite, glass bubbles/fly ash cenospheres, and HTPP fibers.
2. Spray-applied SFR-ECC exhibits reduced tensile ductility compared to cast specimens due to altered fiber bridging behavior and/or compacting of the matrix. Nevertheless, the sprayed SFR-ECC still exhibits ultimate tensile strength of 0.87 MPa (Mix 2) and 0.68 MPa (Mix 5) and tensile strain capacity of 1.0% (Mix 2) and 0.9% (Mix 5), significantly

higher than those ( $< 0.1$  MPa tensile strength and 0.01% strain capacity) of conventional SFRM.

3. SFR-ECC has apparent thermal conductivity and sprayability comparable to conventional SFRM, which ensures proper functionality of SFR-ECC as fireproofing material.
4. The measured adhesive fracture energy of SFR-ECC mixes (with structural steel) are  $104.3 \text{ J/m}^2$  and  $310.4 \text{ J/m}^2$ , significantly higher than that of conventional SFRM ( $11.1 \text{ J/m}^2$ ). The SFR-ECC/steel interface exhibits a ductile fracture behavior associated with fibers bridging across the crack.

SFR-ECC with enhanced durability (mechanical and adhesive properties) and comparable functionality (low thermal conductivity and sprayability) relative to conventional SFRM has been developed in this chapter. The high cohesion and adhesion are expected to contribute significantly towards enhanced durability of the fire protection under ambient temperature. This could prevent damages of the fire protection materials during earthquakes, impacts and normal service loads and ensure the fire safety of steel structures, especially under multi-hazards like post-earthquake/impact fires.

In Chapter 4, two mix design of SFR-ECC have been developed satisfying all the performance requirements identified in Chapter 1. In the next part of the dissertation, multi-scale investigation of the durability property of SFR-ECC will be conducted to further understand the behavior of the newly developed material.

## References

---

1. Li VC, Leung CK. Steady-state and multiple cracking of short random fiber composites. *Journal of Engineering Mechanics* 1992; 118(11): 2246-2264.
2. Li VC, Wang S, Wu, C. Tensile strain-hardening behavior of polyvinyl alcohol engineered cementitious composite (PVA-ECC). *ACI Materials Journal* 2001; 98(6): 483-492.
3. Yang E-H. Designing added functions in engineered cementitious composites. PhD thesis. University of Michigan, 2007.
4. Felekoğlu B, Tosun-Felekoğlu K, Ranade R, Zhang Q, Li VC. Influence of Matrix Viscosity, Fiber Mixing Procedure, and Curing Conditions on the Mechanical Performance of HTPP-ECC. *Composites Part B: Engineering* 2014; 60: 359-370.
5. ASTM E2584. Standard Practice for Thermal Conductivity of Materials Using a Thermal Capacitance (Slug) Calorimeter. West Conshohocken: ASTM International; 2010.
6. Tan KT, White CC, Hunston DL. An adhesion test method for spray-applied fire-resistive materials. *Fire and Materials* 2011; 35(4): 245-259.
7. Li, V. C., "Engineered Cementitious Composites — Tailored Composites through Micromechanical Modeling," *Fiber Reinforced Concrete: Present and the Future*, N. Banthia, A. Bentur, A. and Mufti, A., eds., Canadian Society for Civil Engineering, Montreal, QC, Canada, 1998; 64-97.
8. Kanda, T., and Li, V. C., "A New Micromechanics Design Theory for Pseudo Strain Hardening Cementitious Composite," *Journal of Engineering Mechanics*, ASCE, 1999; 125 (4), 373-381.
9. Li, V. C., and Leung, C. K. Y., "Steady-State and Multiple Cracking of Short Random Fiber Composites," *Journal of Engineering Mechanics*, 1992; 118 (11), 2246-2264.
10. Kim YY, Kong HJ, Li VC. Design of Engineered Cementitious Composite (ECC) Suitable for Wet-mix Shotcreting. *ACI Materials J.* 2003; 100 (6): 511-518.
11. ASTM C128. Standard test method for density, relative density (specific gravity), and absorption of fine aggregate. West Conshohocken: ASTM International; 2006.
12. Japan Society of Civil Engineers (JSCE). Recommendations for design and construction of high performance fiber reinforced cement composites with multiple fine cracks (HPFRCC); March 2008.
13. ASTM C109. Standard Test Method for Compressive Strength of Hydraulic Cement Mortars (Using 2-in. or [50-mm] Cube Specimens). Philadelphia: ASTM International; 2002.
14. Carino, N. J.; Starnes, M. A.; Gross, J. L.; Yang, J. C.; Kukuck, S. R.; Prasad, K. R.; and Bukowski, R. W., "Passive Fire Protection," *Federal Building and Fire Safety Investigation of the World Trade Center Disaster NIST NCSTAR 1-6A*, National Institute of Standards and Technology, Gaithersburg, MD, 2005, 326 pp.
15. AC23. Acceptance Criteria for Spray-applied and Intumescent Mastic Coating Fire-protection Materials. ICC-ES; 2011.
16. UFGS-07 81 00. Spray-applied fireproofing. USACE/NAVFAC/AFCEC/NASA; 2011.

## **CHAPTER 5 MICROSTRUCTURE AND MICROMECHANICS OF SFR-ECC**

This chapter documents the investigations on the micromechanical and microscopic properties of the newly developed SFR-ECC. The micro mechanisms within SFR-ECC that lead to the unique tensile and compressive behavior are investigated.

### **5.1 INTRODUCTION**

In Chapter 4, SFR-ECC with enhanced durability performance has been developed as a durable alternative to the current SFRM. The enhanced durability is associated with the unique mechanical behavior of SFR-ECC compared to other cement-based SFRM. SFR-ECC exhibits high ductility under tension and ductile behavior under compression similar to cellular material, while maintaining the low thermal conductivity critical to its fire-protection function. This unique combination of high tensile ductility and high compressive ductility makes SFR-ECC different from any other materials.

In this chapter, the micromechanical behavior of SFR-ECC is quantitatively assessed and discussed. Its influence to the macro-level composite behavior is also quantitatively studied using the micromechanics-based model. In addition to the ductile behavior under tension, it is also observed that SFR-ECC exhibits a ductile cellular-like behavior under compression. This is very special for cement-based material in general, and ECC in particular. The mechanisms that result in such unique behavior is also investigated under microscopy in this chapter.

In this chapter, the SFR-ECC Mix 2 (developed incorporating glass bubbles) is used for the study. However, it is expected that the findings can be generalized to understand the similar behavior of SFR-ECC Mix 5.

## **5.2 MICROMECHANICS UNDERLYING TENSILE BEHAVIOR**

### **5.2.1 Experimental programs**

In the ECC design theory, the two criteria (energy and strength criteria, **Eq.1.1** and **1.2**) for achieving strength hardening behavior need to be satisfied in order to achieve desirable ductile tensile behavior. These two criteria essentially represent the energy and strength balance between the matrix property ( $J_{ip}$  and  $\sigma_{cs}$ ) and the fiber bridging property (the fiber bridging stress-crack opening ( $\sigma-\delta$  relationship) or the maximum bridging stress  $\sigma_0$ ). All of these properties can be experimentally assessed. The objective of this experimental program is to verify the previously used design approach and quantitatively characterize the micromechanical mechanisms for achieving the macroscopic ductile tensile behavior.

In this chapter, the matrix fracture toughness was measured in accordance with ASTM E399<sup>1</sup> using a three-point bending test setup (**Fig.5.1**). Although ASTM E399 is a standard for testing the fracture toughness of metals, it can be used for determining fracture toughness of brittle materials such as the SFR-ECC matrix that shows small scale yielding and, therefore, the assumptions of linear elastic fracture mechanics are valid<sup>2</sup>. The configuration of the specimen was selected based on the recommendations of the standard. SFR-ECC matrix (without fibers) materials were casted into beam specimens of 152.4 mm long, 25.4 mm wide and 25.4 mm deep. A thin notch (0.6mm thick) of approximately 12.7 mm deep was cut into the tension face of the beam specimen at mid-span to initiate the fracture. The span length between the bottom supports

for the beam was selected to be 101.6 mm. After the test, conditions for small scale yielding were checked using the measured data and confirmed the validity of the test results.

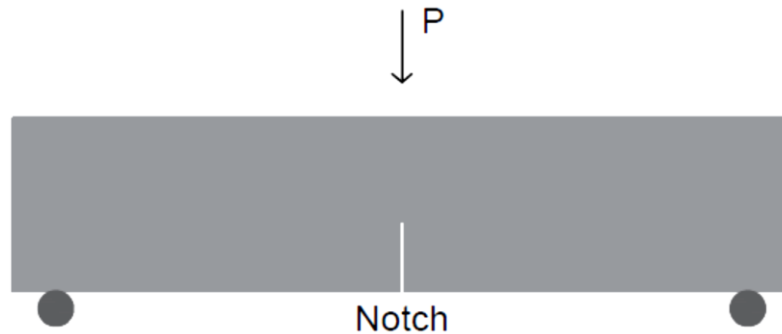


**Fig.5.1 Matrix toughness test configuration**

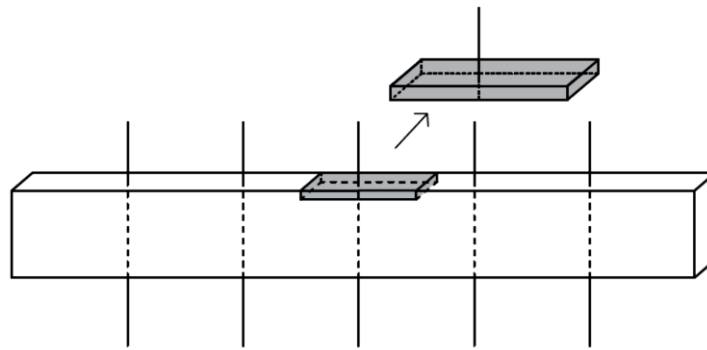
The fiber bridging property was assessed using single fiber pull-out test and scale-linking technique. The single fiber pull-out test characterized the load-displacement relationship of a single fiber being pulled out (from one end) from the SFR-ECC matrix. Scale linking that integrates the contribution of all the fibers on a crack plane was then performed to derive the fiber bridging behavior of the cross section. The derived fiber bridging  $\sigma-\delta$  relation also can be compared with experimental data from single crack test for verifications.

The configuration of single fiber pull-out test is depicted in **Fig.5.2**. As shown in **Fig.5.2(a)**, the single fiber specimens were prepared by placing the long fibers across the rectangular prism mold and then casting the SFR-ECC matrix (without fibers) around the fibers. Then the individual single fiber pull-out specimen was cut from the prism using a precision saw. The thickness of these specimens was carefully controlled to be very small (preferably less than 2mm) to prevent fiber breakage during the pull-out test.

As seen in **Fig.5.2(b)**, during the test, the free end of the fiber was glued to an aluminum plate using super glue and masking tape, which were held by the top grip of an electrical tensile

testing system. The bottom of the specimen was glued to a metal attachment that were then screwed into a high precision load cell with a maximum capacity of 5 N and precision of 0.0125 N. The load cell was attached to an x-y displacement stage that was held by the bottom grips of the tensile testing system. The fiber was pulled out at a controlled displacement rate of 0.5 mm/min (0.008mm/min). The load-displacement relationships were recorded. Single fiber test, by its nature, exhibit large scatter in the data, therefore, large number of specimens were prepared and 15 were successfully pulled out.

The single fiber pull-out tests were also conducted on specimens with inclined fibers that were placed at an inclination angle to the loading direction (as shown in **Fig.5.2(c)**) to characterize the bridging behavior of fibers that are not in the loading direction. Specimens with fibers placed at 17 °, 27 °and 45 °angles to the loading direction were prepared and tested. At least 14 specimens were prepared and tested for each angle and at least 4 specimens were successfully pulled out.



(a)



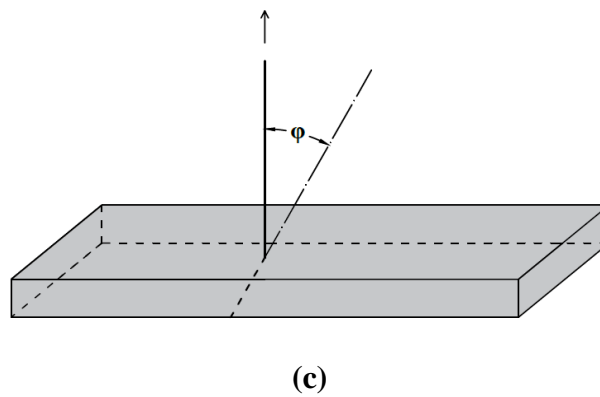
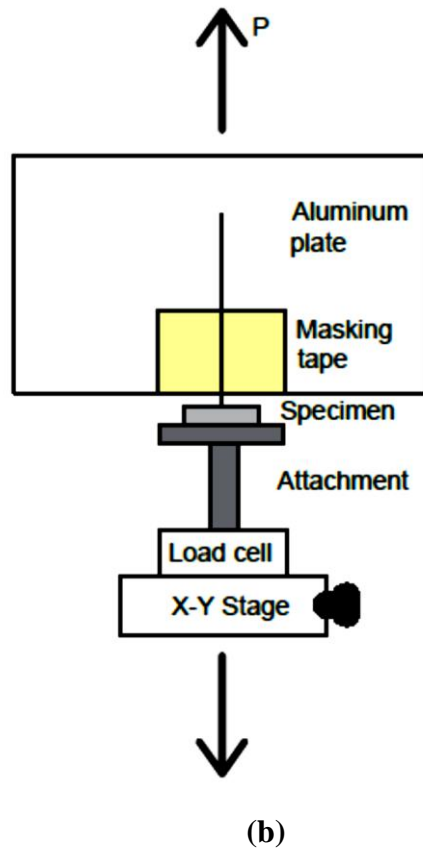


**Fig.5.2 Single fiber pull-out test configuration**

**(a) preparation of specimens, (b) test setup, and (c) specimen for inclined fiber**

The single fiber pull-out test setup can also be used to study the fiber strength and modulus.

When testing fiber properties, one end of the fiber was glued to the metal attachment (which was

attached to the high precision load cell) using super glue and the other end was fixed to the aluminum plate using super glue and masking tape, similarly to the single fiber pull-out test.

Single crack test that directly measures the post-crack fiber bridging behavior of SFR-ECC was also conducted to compare with the  $\sigma - \delta$  relationships deduced from the single fiber tests. Single crack specimen was prepared by creating a thin notch around the surface of tensile dogbone specimens (**Fig.5.3**), so that a weak plane with reduced cross section was created in the tensile specimen. By doing so, the multiple cracking behavior of SFR-ECC was suppressed and single crack behavior was enforced. Two LVDTs were attached close to the crack location to measure the crack opening. The fiber bridging stress was calculated using the recorded load and the reduced cross-sectional area (measured using a caliber after the test). Then the fiber bridging stress-crack opening curves can be constructed.

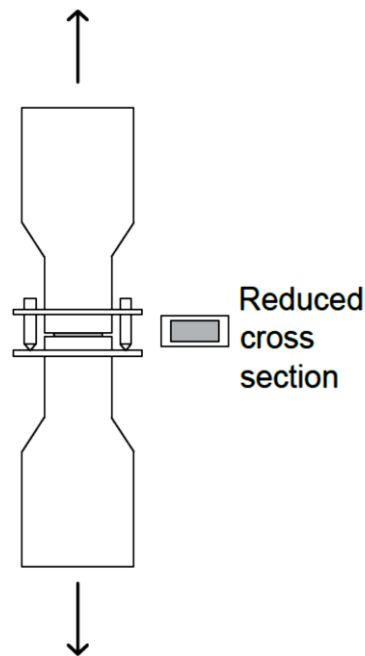


**Fig.5.3 Single crack test configuration**

### 5.2.2 Interpretation of the single fiber pull-out test data

The single fiber pull-out process has two distinct stages. The first stage is called the fiber debonding. The debonding process was modeled as a crack propagation along the fiber/matrix interface, which was studied by Lin et al.<sup>3</sup> as a tunnel crack problem. The debonding load in the fiber as a function of the relative (to the crack plane) pull-out displacement  $u$  is expressed as:

$$P_{debonding} = \sqrt{(\tau_0 u + G_d) \pi^2 E_f d_f^3 (1 + \eta) / 2} \quad (5.1)$$

where  $\tau_0$  is the interfacial frictional stress (assumed to be constant);  $G_d$  is the debonding fracture energy, which is often referred to as chemical bond;  $\eta$  is the volume weighted modulus ratio (assuming fiber volume fraction  $V_f = 0$  for single fiber test and then  $\eta = 0$ );  $E_f$  is the fiber elastic modulus; and  $d_f$  is the fiber diameter.

At the end of the debonding stage, when  $u = u_0$  ( $u_0$  is called critical relative displacement, which can be calculated as  $u_0 = \frac{2\tau_0 L_e^2 (1 + \eta)}{E_f d_f} + \sqrt{\frac{8G_d L_e^2 (1 + \eta)}{E_f d_f}}$ , with  $L_e$  being the fiber embedment length), the debonding load reaches its maximum. The maximum debonding force is then

$$P_a = \pi d_f \tau_0 L_e + \sqrt{\pi^2 G_d E_f d_f^3 / 2} \quad (5.2)$$

After the debonding stage, the fiber enters the pullout stage. In this stage, the force is purely governed by the frictional stress. The pullout load (as a function of the relative displacement  $u$ ) can be expressed as:

$$P_{pullout} = \pi d_f \tau_0 [1 + \beta(u - u_0)] [L_e - (u - u_0)] \quad (5.3)$$

where  $\beta$  is called the slip-hardening coefficient. It denotes the curvature of the  $P-u$  curve at the pullout stage. Slip-hardening effect has been observed due to the fibrillation of the fiber during the pullout stage, resulting in a positive slip-hardening coefficient.<sup>4</sup>

At the start of the pullout stage where  $u = u_0$ , the pullout force:

$$P_b = \pi d_f \tau_0 L_e \quad (5.4)$$

Comparing **Eq.5.2** with **5.4**, we can see that there might be a load drop at the completion of the debonding process. This load drop ( $P_a - P_b$ ) is governed by the chemical bond. Therefore the chemical bond  $G_d$  can be calculated as:

$$G_d = \frac{2(P_a - P_b)^2}{\pi^2 E_f d_f^3} \quad (5.5)$$

The initial frictional stress is then calculated as

$$\tau_0 = \frac{P_b}{\pi d_f L_e} \quad (5.6)$$

The slip-hardening coefficient  $\beta$  in **Eq.5.3** can be determined from the  $P-u$  curve at  $u > u_0$  using least-square estimation.

In short fiber composite such as regular ECC material, fibers that are at an angle to the loading directions often experience additional frictional stress due to the interactions with the matrix at the exit. This is called the snubbing effect. The force to pull out a single fiber at an angle  $\phi$  to the loading direction can be modeled as:<sup>5,6</sup>

$$P(\phi) = P(0) e^{f\phi} \quad (5.7)$$

Where  $f$  is called snubbing coefficient;  $P(\phi)$  is the pull-out force for fiber at an inclination angle  $\phi$  and  $P(0)$  is the pull-out force for aligned fiber with the same embedment length. The snubbing coefficient can be calculated by determining the slope of  $\ln(P_{peak}(\phi)/P_{peak}(0))$  v.s.  $\phi$ .

It is also observed that some fibers are vulnerable to lateral stress, therefore, the fiber strength decreases when loaded at an inclination angle. Lin et al.<sup>3</sup> modeled this behavior using a strength reduction coefficient  $f'$ .  $f'$  can be assessed using the in-situ fiber strength  $\sigma_{fu}(\phi)$  and  $\sigma_{fu}(0)$  (which are the stress at rupture for aligned and misaligned fibers):

$$\sigma_{fu}(\phi) = \sigma_{fu}(0) e^{-f'} \quad (5.8)$$

### 5.2.3 Deduction of $\sigma(\delta)$ using scale linking

Scale linking technique was used to compute the fiber bridging v.s. crack opening ( $\sigma(\delta)$ ) relationship using the measured fiber/matrix interactional parameters.<sup>6</sup> The fiber bridging stress  $\sigma$  as a function of the crack opening  $\delta$  can be computed as:

$$\sigma(\delta) = \frac{V_f}{A_f} \int_0^{\pi/2} \int_0^{(L_f/2)\cos(\phi)} P(u) p(z) p(\phi) dz d\phi \quad (5.9)$$

In the above equation,  $P(u)$  is the single fiber pullout load modeled using **Eq. 5.1, 5.3 and 5.7**;  $p(z)$  and  $p(\phi)$  are the probability density function of the embedded fiber's centroidal distance from the crack plane and the inclination angle, respectively (these functions are used to model the randomness of the fiber distribution);  $V_f$  and  $A_f$  are the fiber volume fraction and the cross sectional area of one fiber. Considering a two way pull-out behavior, the crack opening  $\delta = u_1 + u_2$ ,

where  $u_1$  and  $u_2$  are the relative displacement of both fiber ends. The details of the two-way pull-out mechanism can be found in the reference.<sup>7</sup>

## 5.2.4 Results and discussion

### Matrix toughness

The SFR-ECC matrix fracture toughness ( $K_m$ ) was measured to be  $0.09 \pm 0.01 \text{ MPa} \cdot \sqrt{m}$ . This fracture toughness is considered to be very low compared to other regular and even low density ECC matrices (with matrix toughness between  $0.2\text{-}0.7 \text{ MPa} \cdot \sqrt{m}$ ).<sup>8,9</sup> This can be attributed to high water/cement ratio, and large quantity of micron-sized smooth spherical aggregates. Assuming the Young's Modulus of the matrix is the same as that of the composite (since the fiber volume fraction is low), using the modulus of the SFR-ECC composite (2.01 GPa) calculated from the tensile stress-strain relationships in Chapter 4,  $J_{ip}$  is calculated to be  $4.03 \text{ J/m}^2$ . The low matrix toughness of SFR-ECC is considered favorable for achieving strain-hardening behavior.

### Single fiber pull-out behavior

Two distinct types of pull-out behavior (P-u relationships) were observed from the single fiber pull-out tests as shown in **Fig.5.4**. For the data presented in **Fig.5.4(a)**, there is an obvious load drop after the peak load. As reviewed in section 5.2.2, such drop indicates the presence of chemical bond on the fiber matrix interface. This is in contradiction with previous experience. HTPP fiber has a hydrophobic nature, therefore, the chemical bond between HTPP fiber and cement matrix was typically considered negligible in previous studies.<sup>10,11</sup> However, unlike pure cementitious matrix, in SFR-ECC, the addition of polymeric latex results in the formation of a cement-polymer co-matrix. The polymer matrix/polymer fiber interface is then expected to possess

chemical bond. **Fig.5.4(b)** shows another type of pull-out behavior. This set of data exhibits no load drop after the peak load. This indicates zero chemical bond on the HTPP fiber/SFR-ZECC matrix interface, which is a typical HTPP fiber/cement matrix interfacial bonding behavior.

The presence of the two distinct types of pull-out behavior indicates that the polymer matrix is not continuous within the material. The polymer (solid)/cement ratio (3%) in SFR-ECC is considered low, therefore the polymer matrix cannot bond everywhere on the fiber/matrix interface (**Fig.5.5**). This discontinuity in the matrix results in different single fiber pull-out behaviors. It was observed that about 40% specimens showed chemical bond while the remaining 60% showed no chemical bond. In addition, the measured chemical bond was subject to large variability.

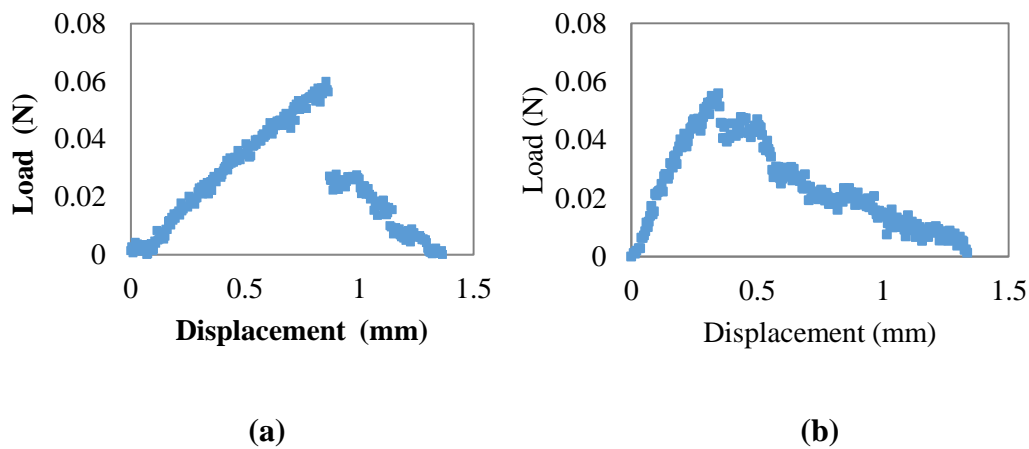


**Fig.5.4 Examples of different single fiber pull-out behaviors of SFR-ECC specimens data suggesting chemical bond, (b) data suggesting no chemical bond**

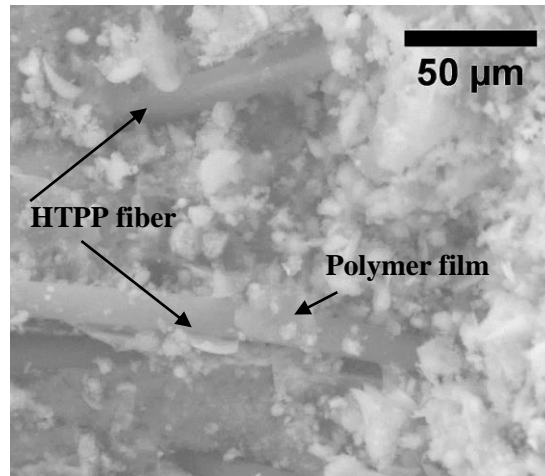


**Fig.5.5 SEM image of HTPP fibers pulled-out from SFR-ECC showing nonhomogeneous fiber/matrix interface**

**Table 5.1** summarizes the calculated interfacial bonding properties for specimens that showed chemical bond and specimens that didn't. Comparing the data in **Table 5.1**, we can see that when chemical bond exists on the fiber/matrix interface, the chemical bond is high. As a reference, in previous study, the chemical bond between the hydrophilic PVA fibers (without oil coating) and cement-based ECC matrix is around  $5 \text{ J/m}^2$ .<sup>12</sup> This is expected, since the primary reason for introducing polymeric latex into the SFR-ECC is because of its highly adhesive nature. However, the measured chemical bond values were subject to large variability. In the single fiber pull-out model, it is assumed that the chemical bond is constant along the embedment length, which is not true in the SFR-ECC case, therefore, the derived chemical bond (according to the single fiber pull-out model) showed large scatter.



**Table 5.1 Measured interfacial properties of SFR-ECC**

	$G_d$ J/m <sup>2</sup>	$\tau_0$ MPa	$\beta$
Specimens with chemical bond	19.3 ± 5.3	1.08 ± 0.37	-0.03 ± 0.02
Specimens without chemical bond	0.02 ± 0.01	0.97 ± 0.23	-0.04 ± 0.03
Average for all fibers	2.83	1.01	-0.035

The frictional bond and slip-hardening coefficient measured for both type of specimens are fairly similar. This indicates that all fibers exhibit similar behavior after the debonding stage. The slip-hardening coefficient is slightly negative, however, the value is very close to zero. This shows that the frictional stress on the HTPP fiber/SFR-ECC matrix interface is kept constant or slightly decreases during the fiber pull-out stage. Previous study also observed that the slip-hardening coefficient approaches zero for HTPP fibers.<sup>10,11</sup>

The average values of the  $G_d$ ,  $\tau_0$  and  $\beta$  considering all the specimens are also summarized in **Table 5.1**. When taking the average of  $G_d$ , the measured quantity ( $P_a$ - $P_b$ ), which is proportional to  $\sqrt{G_d}$  (**Eq.5.2**), is averaged instead of directly averaging the derived  $G_d$ .

The snubbing coefficient is determined following the aforementioned procedure using the single fiber pull-out test data of the inclined fibers. In **Fig.5.6**, the calculated  $\ln(P_{peak}(\phi) / P_{peak}(0))$  are plotted as a function of the angle. Based on the measured data, there is no noticeable increase in the pull-out load as the fiber inclination angle  $\phi$  increases. The snubbing coefficient of 0.07 is considered very low compared to previously measured data for regular ECC (with  $f$  between 0.2-0.8).<sup>12,13</sup> The weak matrix (at the fiber exit) could greatly limit the snubbing effect,<sup>6</sup> with much weaker and softer matrix, the snubbing coefficient of SFR-ECC is expected to be significantly lower than regular ECC materials.

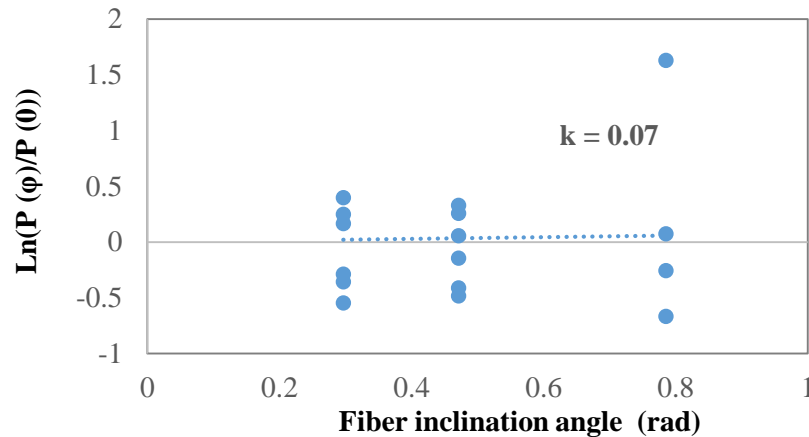


**Fig.5.6 Deduction of the snubbing coefficient f**

### Computed $\sigma(\delta)$ relationships

A MATLAB code developed by Yang<sup>10</sup> was adopted with some modifications in this study to compute the  $\sigma(\delta)$  relationship of SFR-ECC, based on the single fiber model and scale linking described in section 5.2.3. In this study, the fiber dispersion was assumed to be a random 2-D distribution. The input values for the MATLAB code, including fiber, matrix and fiber/matrix interaction properties, are listed in **Table 5.2**.

In this table, the fiber length, fiber diameter, and modulus of fiber were all obtained from the fiber manufacturer. The fiber strength was measured by direct tension test on individual fibers, and the tested value (857 MPa) are very similar to the manufacturer’s data (850 MPa). The fiber volume fraction is set to be 0.8% in this study. During the mixing of SFR-ECC, 1.5% (by volume fraction) fiber was added into the matrix based on calculated volume of the mixture (using rule of mixtures assuming no air entrainment). However, due to the air entraining effect, the fresh density was lower than the calculated one. Therefore, the actual fiber volume fraction is less than 1.5%; it is around 0.8-0.9%.

**Table 5.2 Input parameters for computing  $\sigma(\delta)$  relationship**

Parameter	Input value	Parameter	Input value
Fiber length, mm	10	Micro-spall coefficient	500
Fiber diameter, $\mu\text{m}$	12	Frictional stress, MPa	0.60*
Modulus of Fiber, GPa	6	Chemical bond, $\text{J/m}^2$	1.0 *
Tensile strength of fiber, MPa	875	Slip hardening coefficient	-0.035
Fiber volume fraction, %	0.8	Snubbing coefficient	0.07
Matrix modulus, GPa	2.01	Strength reduction factor	0.1
Matrix tensile strength, MPa	1.0	Cook Gordon paramter	180

The matrix properties were assumed to be the same as SFR-ECC composite (with fibers) properties and therefore were obtained from the composite tensile test documented in Chapter 4. The micro-spall coefficient, strength reduction factor and Cook Gordon coefficient are assumed values based on previous research.<sup>7,14,15</sup>

In **Table 5.2**, lower than measured values were selected for inputs of frictional stress and chemical bond (indicated with “\*”). Using the original measured values (from **Table 5.1**) resulted in a much stiffer and stronger  $\sigma(\delta)$  relationship than the measured curves. This suggests that in actual SFR-ECC, the interfacial bond could be lower than that in single fiber pull-out test.

There are several possible reasons for this phenomenon. Firstly, in the single fiber pull-out test, the fiber is pulled out from pure matrix (without other fibers). However, for actual SFR-ECC composite, during the mixing, additional air entrainment due to the presence of fibers has been observed.<sup>16</sup> This might be especially true for HTPP fibers. Since they are very thin, equal volume fraction of HTPP fibers possess 10 times more fibers and 2 times more surface areas than the PVA fibers regularly used in ECC. This could reduce the interfacial bond in real composite.

Secondly, the single fiber specimens are very thin (typically between 0.5mm and 2mm thick to enable full fiber pull-out behavior), which lowers the chance of larger flaws. The size of

the air pores inside SFR-ECC composite ranges from 0.2-0.5 mm. The larger air pores are less likely to be present within the thin single fiber specimens. In actual composite, fibers could go through an air pore (**Fig.5.7**), and under such case, the fibers are not bonded with the matrix at all in that portion. This phenomenon also could lead to lower interfacial bond in actual composite than that measured with single fiber pull-out test.

Thirdly, despite the high energy mixing procedure, the fiber dispersion is not perfect in SFR-ECC, due to very low mixture viscosity.<sup>17</sup> **Fig.5.7** also shows the bundled fibers within the SFR-ECC. Previous research also suggests that bundled fibers could reduce the interfacial bond due to reduced effective surface area.<sup>6</sup>

In the reference, to account for the bundle effect, the effective bond properties are used. The effective bond property is calculated by the measured bond property (from single fiber pull-out test) multiplied by the percentage of interfacial area reduction (due to fiber bundles). Since all the factors that lead to lower interfacial bond (than measured values) are to some extent associated with reduced bonded area, therefore, the effective interfacial bond concept is adopted in this research.

In this chapter, assuming an average of 60% reduction in the interfacial surface area, the effective interfacial bond parameters ( $\tau_0$  and  $\sqrt{G_d}$ ) were then selected to be 60% of their measured values from the single fiber pull-out test. The measured values for slip hardening coefficient and snubbing coefficient were used without reduction, since they are not directly associated with surface area.

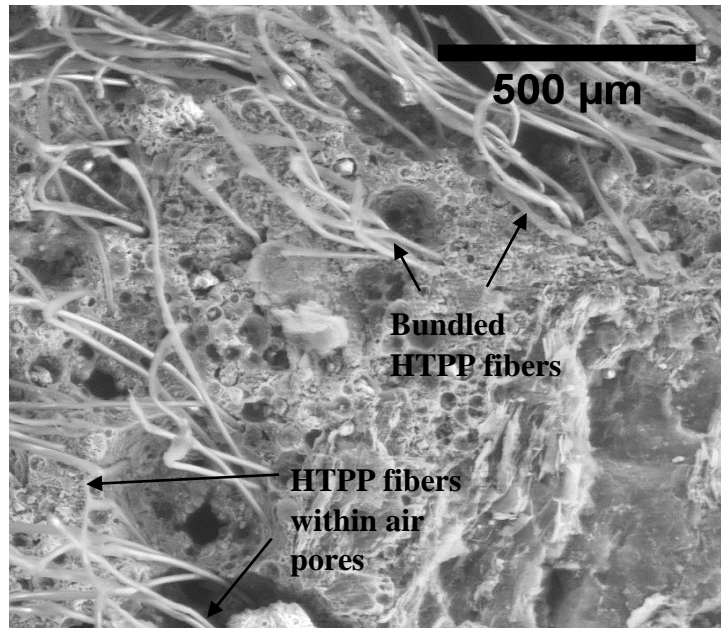


**Fig.5.7 SEM image showing bundled fibers and fibers within air pores in SFR-ECC**

It is worth mentioning that the reduction factor of 0.60 was selected to match the average measured  $\sigma(\delta)$  curve. The bundle effect (and other factors) could vary among cross-sections, since naturally the cross-section with more fibers should have more bundled fibers.

The computed  $\sigma(\delta)$  curve is plotted together with the tested curves obtained from single crack test in **Fig.5.8**. As **Fig.5.8** suggests, the computed fiber bridging curve matches the testing curve acceptably well in the initial part of the curve. However, the computed curve is slightly stiffer around the peak and much stiffer in the post-peak portion.

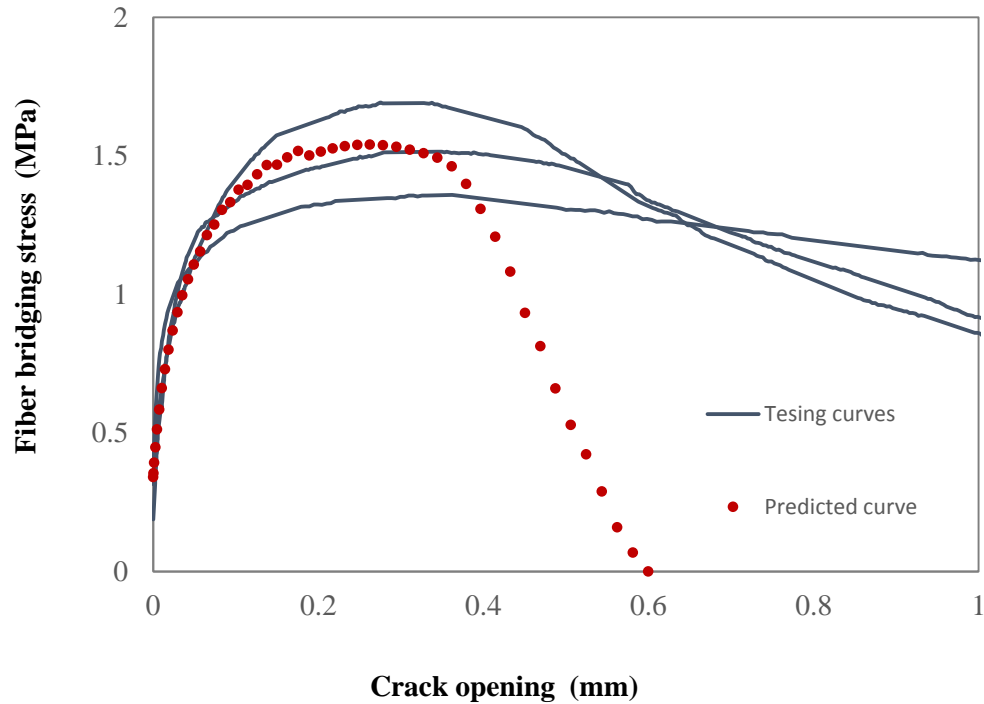


**Fig.5.8 Computed fiber bridging curve using micromechanical model as comparison to testing curves from single crack test**

The micromechanical model predicts that most fibers are ruptured instead of being pulled out, which is confirmed with experimental observations. **Fig.5.9** shows the crack surface of single crack specimen under SEM. The parts of fibers that stick out of the crack surface are mostly under 1 mm long, which indicates that most of the fibers were ruptured. The HTPP fibers used in SFR-ECC are 10 mm long. If the fiber were pulled out without rupture, the part of fibers sticking out should be between 0-5 mm. There is only a couple of long fibers sticking out, which might be a result of variability in the fiber strength and matrix/fiber interfacial property.

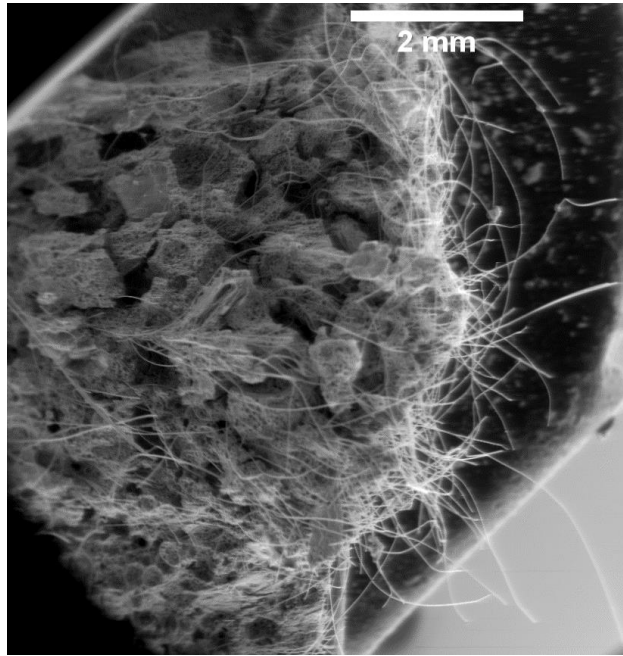


**Fig.5.9 SEM image of cracked surface of single crack specimen**

It is hypothesized that the discrepancy between the computed curve and the testing curves in the post-peak portion is a result of the stretching of HTPP fibers. In previous micromechanical models<sup>7</sup>, only the relative displacement between the fibers and matrix due to elastic stretching were accounted for in the calculation of the fiber bridging load at a given crack opening during the debonding stage. In the post-debonding stage when the fiber is slipping out, even this elastic stretching is considered negligible when compared with the fiber end slippage, and is ignored. Such assumptions are reasonable for PVA and PE fibers that have relatively high modulus and low failure strain. However, for HTPP fibers, the elastic modulus is low (6 GPa), which is 1/7 of the modulus of the PVA fibers that were typically used in ECC. In addition, the strain of HTPP fiber at rupture is as high as 21%. Under tension, HTPP fiber stretches significantly and non-linearly before failure. Neglecting this could artificially result in a stiffer fiber bridging behavior, especially when there are fiber ruptures at failure.

To examine this hypothesis, the elastic and inelastic stretching of fibers are taken into consideration. Two fiber constitutive models were considered. Firstly, the fiber is assumed to have linear elastic behavior under tension all the way to rupture (dashed line in **Fig.5.10**). The elastic modulus is assumed to be the initial elastic modulus of the fiber (6 GPa). Using the data for HTPP fiber, at failure, this model accounts for 14% tensile strain of the fiber. Secondly, a bilinear model is used. The initial elastic portion is the same as the linear elastic model up to 2/3 of the fiber strength, and then the stiffness reduces (solid line in **Fig.5.10**). At failure, the rupture strain was set to be  $1.5 * \sigma_f / E_f$  (where  $\sigma_f$  is the fiber strength and  $E_f$  is the initial fiber elastic modulus) to match the data for HTPP fibers, which resulted in 21% strain at fiber rupture. The second model is considered more representative for the actual fiber behavior.

When computing the fiber bridging behavior, two stretching conditions are considered. Firstly, the stretching of fibers is considered only within the crack opening. In this case, it is assumed that other than the relative displacement between the fibers and matrix due to elastic stretching during the debonding stage (which is captured in the original model), the straining (elastically and inelastically) of fibers over the length within the crack opening ( $\delta$ ) also contributes to the crack opening. This assumption could be very conservative. In fact, the fibers are not bonded with the matrix everywhere (due to the presence of air pores), and the interfacial bond is also subject to large variation. Therefore it is very likely that the fibers are strongly bonded (and therefore almost fixed) to the matrix at certain location while loosely bonded at other locations. As the crack opens up, those loosely bonded portion could be slipping relative to the matrix and start to stretch under load. Such stretching should be significantly larger than the originally



assumed elastic straining during the debonding stage. Therefore, in a second case, it is assumed that the fibers stretch over a length segment of  $3\delta$ .

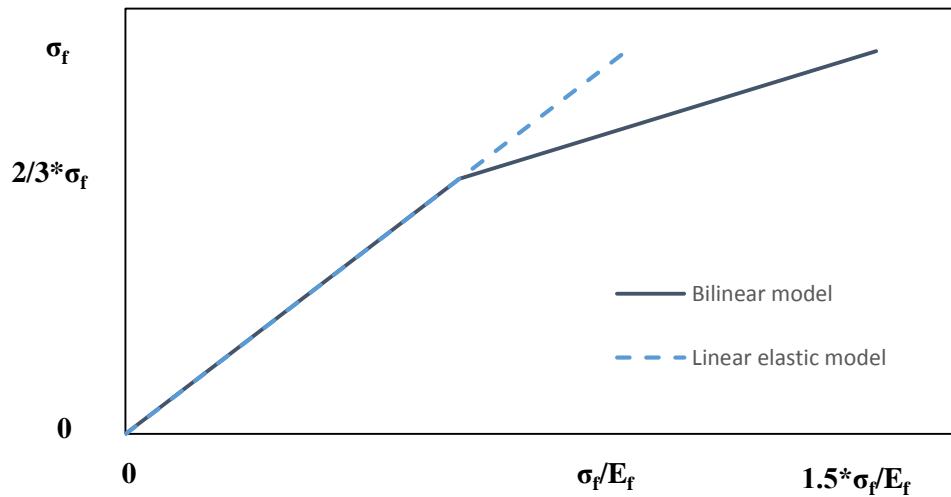


**Fig.5.10 Linear elastic and bilinear fiber constitutive models**

**Fig.5.11** plots the computed fiber bridging curves considering above assumptions. For reference, the testing curves and previous computed curve are also plotted in this figure. From the figure, we can see that the fiber stretching does not significantly alter the bridging behavior in the pre-peak portion other than slightly softening the curve around the peak. At this portion, the fibers are not experiencing large strain, and the crack opening (or the gage length of the stretching portion of the fibers) are also relatively small. However, the post-peak load drop is much slower if considering fiber stretching and get further slowed down if the nonlinear behavior of fibers is considered, which explains the much slower load drop of the testing curves compared with previous model.

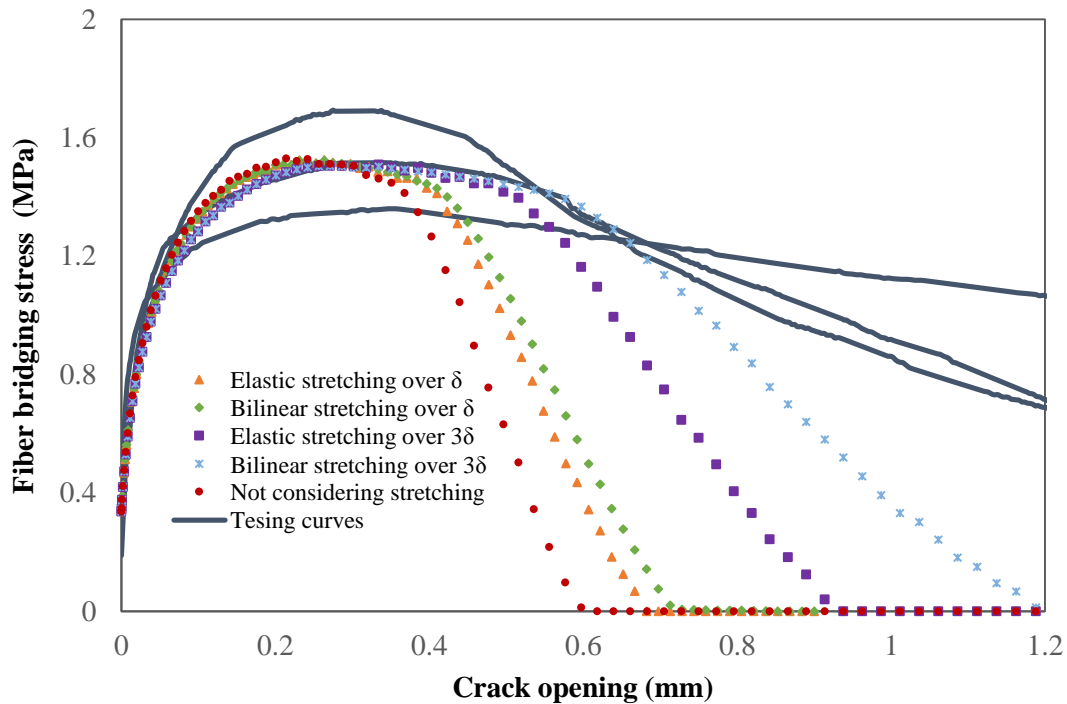


**Fig.5.11 Computed fiber bridging curve considering fiber stretching as comparison to the previous model**

Other factors may further slow the post-peak load drop. For example, it is also observed some fibers are not straight inside the matrix. Such fibers might not engage in the fiber bridging until relatively larger crack openings, which could slow down the load drop at larger crack opening. The fiber rupture strength and strain also vary, which could also lead to larger crack opening as the fiber bridging stress diminishes to zero. All these effects (including fiber stretching) are mostly associated with the post-peak portion of the fiber bridging curve, however, to assess the strain hardening potentials of SFR-ECC, the pre-peak portion of the fiber bridging effect is of greater interest. All the above described models predict the same fiber bridging strength ( $\sigma_0$ ), very close fiber bridging complementary energy ( $J_b'$ ) and all give the same conclusions in the following analysis and studies in Chapter 6. Therefore, the result from the fiber bridging model that considers

additional linear elastic stretching over crack opening ( $\delta$ ) is used for the following analysis and in Chapter 6.

## Discussion

The calculated  $J_b'$  using the computed  $\sigma(\delta)$  curve is  $59.5 \text{ J/m}^2$  and  $J_b'/J_{tip}$  is 14.8. In previous research,<sup>18</sup> an empirical threshold for achieving robust tensile ductility is set to be  $J_b'/J_{tip} > 3$ . This is satisfied comfortably in SFR-ECC. In fact, due to the extremely low matrix fracture toughness, the energy inequality ( $J_b' > J_{tip}$ ) can be easily satisfied.

Regarding the strength criteria, the ratio  $\sigma_{cu}/\sigma_{cs}$  could be used as an indicator of the level of satisfaction of the strength criterion.  $\sigma_{cu}$  is the tensile ultimate strength of SFR-ECC, which is governed by the minimum fiber bridging capacity of all cross-sections and  $\sigma_{cs}$  is the first cracking strength. For SFR-ECC, the  $\sigma_{cu}/\sigma_{cs}$  is relatively low. From the composite test results, this ratio is around 1.14. Although greater than 1 (satisfying the strength criterion), the  $\sigma_u/\sigma_{cs}$  value is slightly lower than the recommended empirical threshold of 1.2 for ECC material to achieve robust strain hardening.<sup>18</sup> However, in SFR-ECC, the relatively lower margin might be compensated by large number of flaws (compared to regular density ECC material) associated with its porous microstructure. Thus despite the relatively low  $\sigma_{cu}/\sigma_{cs}$  ratio, SFR-ECC still exhibits robust strain hardening behavior.

To further understand the effect of the chemical bond, the  $\sigma(\delta)$  relationship assuming zero chemical bond was also computed using the analytical model. The other inputs were assumed to be the same as in **Table 5.2**. The computed  $\sigma(\delta)$  curve is plotted in **Fig.5.12** (solid line) and the

previous computed  $\sigma(\delta)$  curve (considering linear elastic fiber stretching over crack opening) is also plotted for comparison (dashed line in **Fig.5.12**).

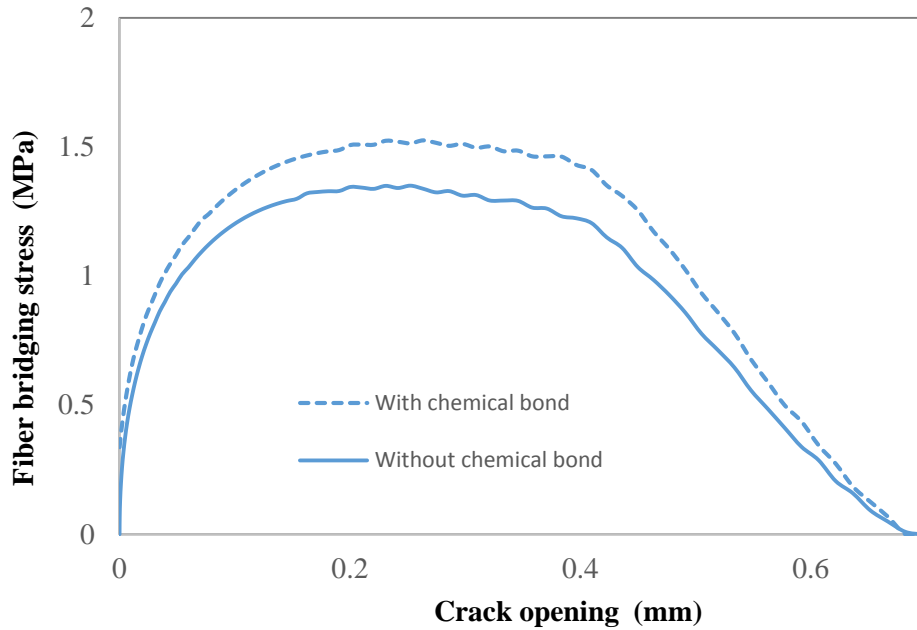


**Fig.5.12 Effect of chemical bond on  $\sigma(\delta)$  relationship of SFR-ECC**

Comparing the two computed  $\sigma(\delta)$  curves, it can be observed that the new curve (calculated assuming  $G_d = 0$ ) shows a slightly softer behavior. The fiber bridging strength  $\sigma_0$  is about 11.5% lower than the reference curve and the complementary energy  $J_b'$  also decreases by 14.5 % compared to the reference. Based on both energy and strength criteria for achieving strain hardening behavior, the presence of chemical bond is considered beneficial for the strain hardening behavior, especially because its effect in enhancing  $\sigma_0 / \sigma_{cs}$  (and therefore  $\sigma_{cu} / \sigma_{cs}$ ).

The presence of chemical bond is caused by the incorporation of the polymer latex. Therefore, in addition to modification of the adhesive property (to steel), the incorporation of polymer latex also improves the interfacial bonding properties. It is worth noticing that this may only be beneficial for hydrophobic polymer fibers, such as polypropylene fibers and polyethylene

fibers, of which the interfacial bond is considered weak. For PVA fibers that already possess high chemical bond, further increase of chemical bond may be undesirable. When using polymer latex to modify the interfacial property, the air entraining effect (as found in Chapter 2) should be carefully controlled if necessary (e.g. by using anti-foaming agent).

### 5.3 MICROSTRUCTURAL INVESTIGATION ON COMPRESSIVE BEHAVIOR

In Chapter 4, it was discovered that the compressive behavior of SFR-ECC resembles the behavior of cellular (foam) materials, which is very different from the brittle failure often observed in cement-based material. The typical compressive stress-strain relationship of SFR-ECC is plotted in **Fig.5.13**. The entire curve can be divided into three stages: the linear elastic stage (before point 1), the plateau stage (between 1 and 2) and the densification stage (after point 2, the rapid rising portion of the curve). This type of behavior was observed both with cube specimens and cylindrical specimens of SFR-ECC, confirming that it is a true material behavior.

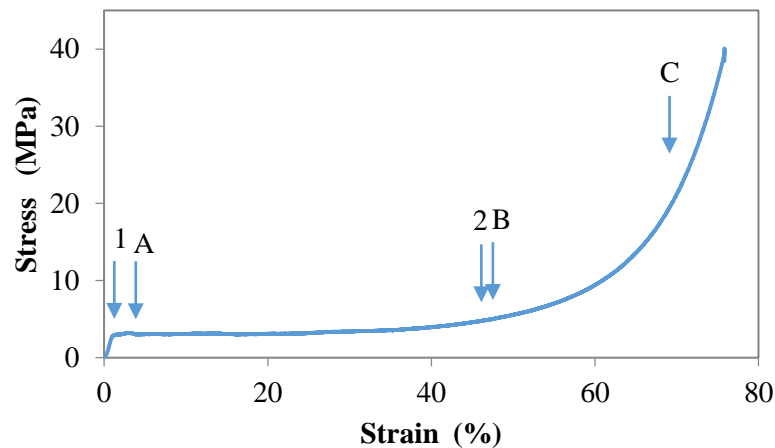


**Fig.5.13 Typical compressive stress-strain relationship of SFR-ECC**

The mechanism behind the ductile compressive behavior in typical cellular material is that they have a cellular (porous) microstructure. Under compression, the cell walls around the cells

yield, buckle or even fracture, successively closing the cells (pores). At the end of the plateau, all the cells close and the cell walls crush into each other. During the densification stage, the material get further compacted as collapsed cell wall materials are in full contact, as a result, there experiences a sharp increase in the compressive stress.<sup>19</sup> The ductile cellular compressive behavior is more often observed in metallic and synthetic foams.

Regarding brittle matrix foams (including lightweight concrete), both brittle fracture and cellular behavior have been observed.<sup>20,21</sup> The transition between brittle and ductile failure is associated with differences in porosity and pore size. According to previous researches, high porosity and smaller pore size are favorable for achieving the ductile cellular behavior. The fracture failure is governed by isolated large pores while the cellular behavior is caused by successive collapse of the closely distributed cells (as indicated by **Fig.5.14**). For material with lower porosity (<50%), the fracture failure is dominant, resulting in a brittle failure, which is the case for most normal density and lightweight concrete. For higher porosity material, depending on the pore size, either failure mode could happen.

In addition, even for brittle matrix foam with ductile cellular behavior, the brittle fracture of the cell walls often leads to fluctuation of stress during the cell collapse (in the plateau stage due to the load drop at fracture of cell walls) and expansion on the lateral direction (“barreling”)<sup>22,23</sup>. If the fracture of the walls and deformation are not well confined, very likely, the densification stage will not be reached.<sup>22</sup>

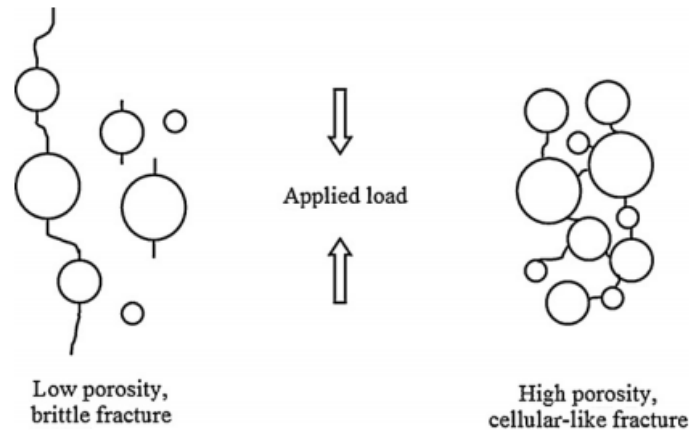


**Fig.5.14 Brittle and cellular-like fracture of brittle matrix foam material<sup>21</sup>**

In SFR-ECC, both air pores (introduced by air entrainment) and glass bubbles could form a cellular structure. The porosity of SFR-ECC is expected to be very high. A rough estimate of the porosity of air pores can be made by taking the ratio between the calculated density (using rule of mixture) and measured fresh density of SFR-ECC, which is above 40%. Plus, the glass bubbles take up 20% of the total volume of SFR-ECC, which are mostly closed pores. The size of the air pores are typically 0.2-0.5 mm and the pores inside the glass bubbles are around 0.05mm. These pore sizes are considered very small. The high porosity and small pore size of SFR-ECC provide the potential for a ductile cellular-like compressive behavior. However, whether the air pores or the glass bubbles govern the cellular behavior remains unknown.

In SFR-ECC, the plateau stage shows little stress fluctuation and the densification stage is apparent. It is hypothesized that the presence of toughening mechanism in SFR-ECC (fiber reinforcement) helps suppress the brittle fracture, provide confinement and favor the cellular behavior.

To verify the above hypothesis, a microscopic study was conducted to uncover the underlying mechanisms of the ductile compressive behavior of SFR-ECC.

### 5.3.1 Specimens and procedures

Four small cube specimens of 10 x 10 x 12.7 mm were prepared for observation under the Environmental Scanning Electron Microscope. The specimens were made by cutting from the SFR-ECC tensile dogbone specimens. The cubes were then compressed using an electrical testing system and the load-displacement curves were monitored. When the cubes reached desired stage, the loading was aborted. The microstructure of the SFR-ECC under three loading stages (as indicated by the arrows in **Fig.5.13**) were studied: (A) during plateau stage, (B) starting of densification, and (C) later stage of densification. The fourth specimen was not loaded. The four specimens were then observed under an Environmental Scanning Electron Microscope to characterize their microstructure.

### 5.3.2 Results and discussions

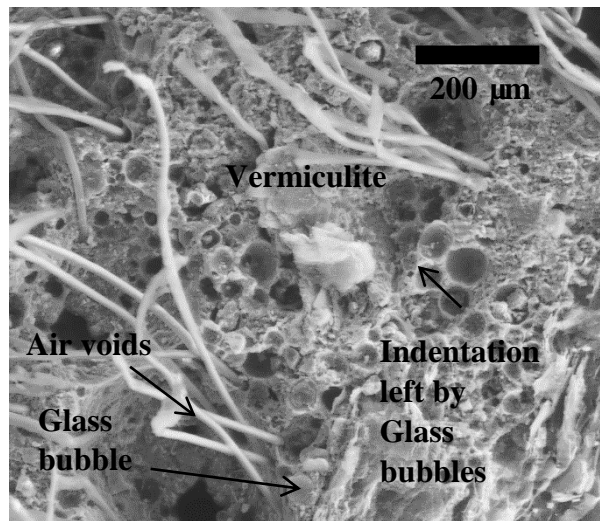
**Fig.5.15(a)** shows the original (without loading) microstructure of SFR-ECC. SFR-ECC has a very porous (cellular) microstructure. There're two major type of pores (cells) in SFR-ECC: larger size air pores (~200-500  $\mu\text{m}$ ) and the pores inside the glass bubbles (~50  $\mu\text{m}$ ). The SFR-ECC matrix forms the cell walls for the larger air pores, and the fiber reinforcement further toughens these walls. Regarding the smaller cells formed by glass bubbles, the polymer-cement co-matrix that wraps around the glass bubbles also forms the cell walls for these micron-sized cells (as shown in **Fig.5.15(b)**).

The large volume of air pores within SFR-ECC are mainly because of air entrainment during the mixing. There are several causes for the significant air entrainment. Acrylic latex admixtures were found to have significant air entraining effect in FR-ECC (Chapter 3), which should contribute to the air entrainment in SFR-ECC as well. Large number of HTPP fibers, which

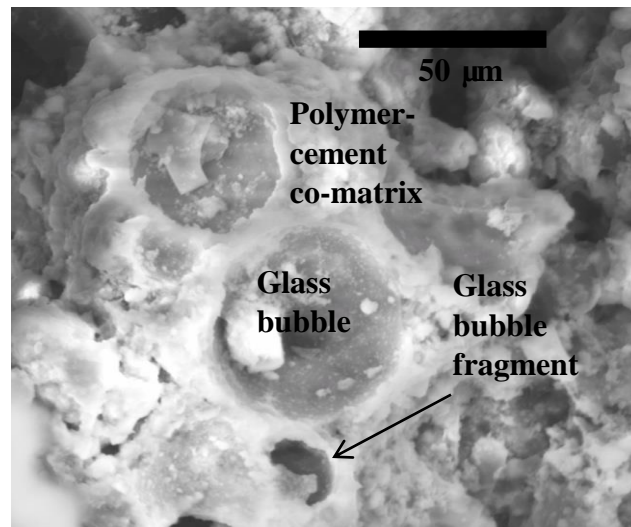


have hydrophobic surfaces, could also introduce large volume of air during mixing. The above factors could be further enhanced by the high energy mixing (necessary for dispersing the fibers in SFR-ECC). In addition to the air entrainment, the high water/cement ratio (1.2) also leads to higher porosity within the material.

It is worth pointing out that the air pores are of small size. Most of the pores are 200-300  $\mu\text{m}$ , with maximum size around 500  $\mu\text{m}$ . These air pores are significantly smaller than those in SFRM (up to several millimeters). The fine air pore structure is a result of the fine microstructure of all other components within the SFR-ECC and low viscosity of SFR-ECC at fresh state. In addition to contributing to the cellular behavior under compression, these pores should also contribute to the low thermal conductivity of SFR-ECC according to the heat transfer theory as discussed in Chapter 2.



(a)



(b)

**Fig.5.15 Cellular microstructure of SFR-ECC**

**Fig.5.16** shows the microstructure of SFR-ECC at loading stage A (plateau stage). From the figure, we can observe that during this stage, cracks formed from the edge of the large air pores under compressive load and continued to propagate and connect to other pores similar to the cellular behavior shown in **Fig.5.14**. The crushing and controlled fracture of the cracked cell walls under compression gradually closed the air pores. The closing of the pores occurred layer by layer successively, leading to large deformation under compression while maintaining almost constant load level. Macroscopically, the compressive deformation also happens layer by layer as shown in **Fig.5.17**. There was also observed lateral barreling deformation of the specimen as the figure indicates.

Such behavior is similar to the cellular-like fracture of brittle matrix foam reported in literature. However, there was no fragmentation of the cell walls during the collapse of air pores, associated with the fiber bridging across the cracks, which could explain the minimal stress fluctuation during the plateau stage. Also, the fiber bridging effect provided effective lateral confinement and allowed SFR-ECC to reach densification stage without losing stability. From the

microscopic study, we can see that the ductile plateau is primarily associated with the collapse of air pores; the glass bubbles are not engaged at this stage.

At the end of the plateau stage, all air pores collapsed with cell walls crushed into each other, and further compression led to densification of the matrix, which involved collapse of glass bubbles. As shown in **Fig.5.18**, the glass bubbles deformed and fractured under compression, and the cement-polymer co-matrix around the glass bubbles gradually crushed into each other. However, the collapse of glass bubbles is part of the densification stage, which does not govern the failure mode (brittle vs. cellular) of SFR-ECC under compression.

At later stage of the densification, most of the voids (both air pores and glass bubbles) disappeared as shown in **Fig.5.19**. The microstructure revealed crushed fragments of glass bubbles. Therefore, the compressive stress has increased sharply during the densification stage.

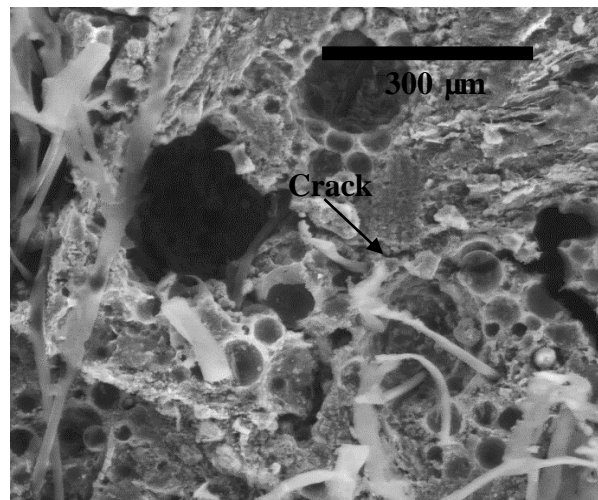


**Fig.5.16 Crack forms connecting air pores at plateau stage**

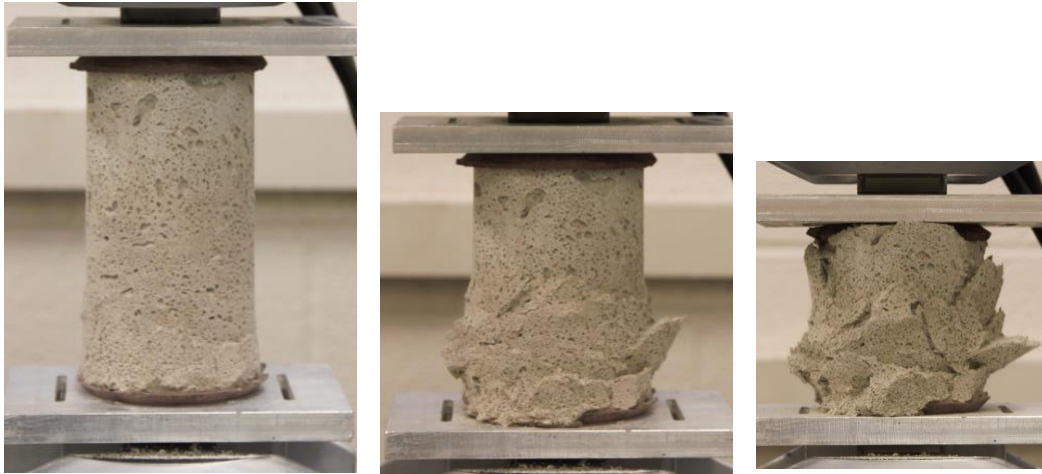


**Fig.5.17** Successive deformation SFR-ECC during the plateau stage under compression

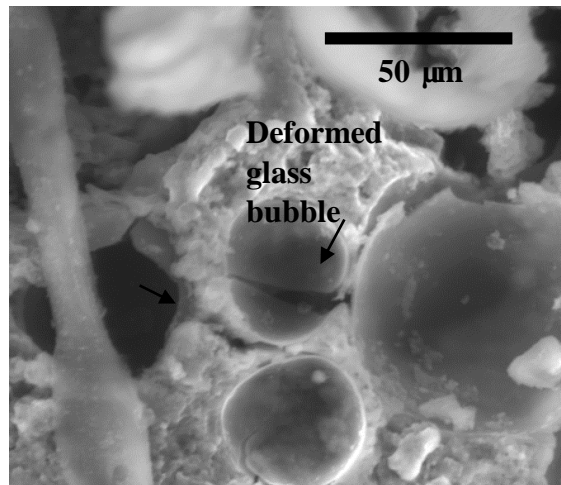


**Fig.5.18** Collapse of glass bubbles during densification

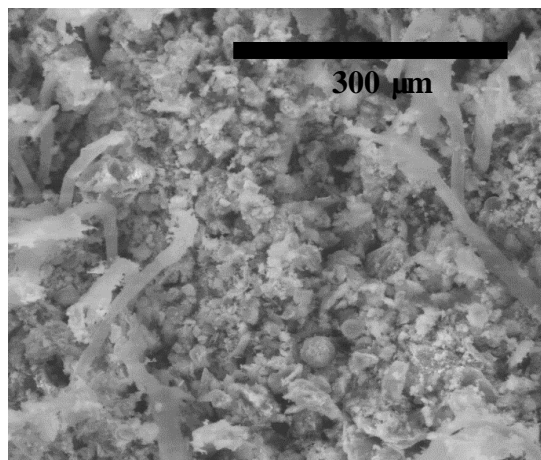


**Fig.5.19** Microstructure of SFR-ECC at later stage of densification

As alluded to in the above discussion, the fiber reinforcement offers lateral confinement which favors the cellular behavior. To further look into the role of fiber reinforcement, cube specimens (50.8 x 50.8 x 50.8 mm) and cylindrical specimens ( $\Phi 76 \times 152$  mm) of SFR-ECC matrix (without fibers) were also tested under compression.

The cube specimens of the SFR-ECC matrix showed the ductile cellular-like behavior while the cylindrical specimens showed fracture failure. For more confined configuration (smaller cube specimen with stronger confinement effect due to specimen end constraints from lateral straining), after fracture of the cell walls (for air pores), the fracture and fragmentation of the matrix were controlled within the core of the specimen (although the outer surface were gone), allowing successive collapse of the air pores and further densification of the matrix (**Fig.5.20(a)**). However, in the less confined configuration (cylinders), the fracture and fragmentation was not controlled; the specimens lost stability and failed in fracture (**Fig.5.20(b)**). For SFR-ECC composite (with fibers), even in the less confined configuration, the fiber bridging suppressed the fracture failure, provided effective confinement and allowed further densification of the composite (**Fig.5.21**).

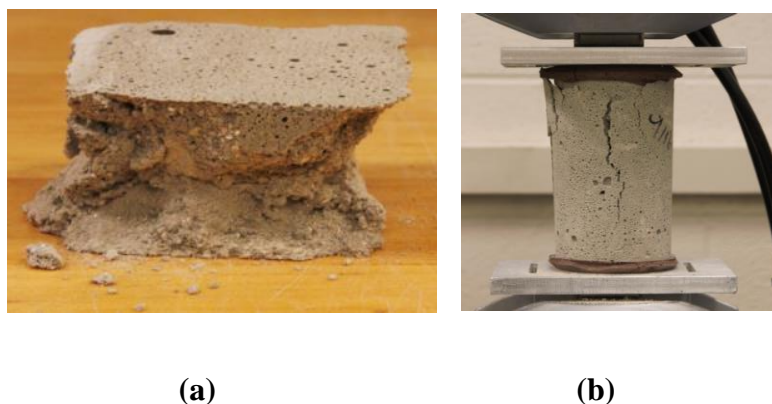


**Fig.5.20 Different compressive failure mode for (a) cube and (b) cylinder specimen of SFR-ECC matrix due to different confinement level**



**Fig.5.21 Densification of SFR-ECC composite under compression ( $\Phi 76 \times 152$  mm cylindrical specimen)**

To summarize the above findings, SFR-ECC has a cellular microstructure formed primarily by high content of small-sized air pores (introduced due to air entrainment). The successive collapse of air pores by controlled cracking and crushing of cell walls results in a ductile compressive behavior. The fiber bridging effect also offers lateral confinement, suppresses fracture failure and favors the cellular-like behavior. The unique combination of high tensile ductility and high compressive ductility in SFR-ECC significantly increases the energy absorption capacity of such material. The energy absorption capacity of SFR-ECC is expected to be an order of magnitude higher compared to normal concrete material both under tension and compression. This opens the opportunity for various applications of SFR-ECC other than spray-applied fireproofing application. For example, it may replace the synthetic or metallic foam often used in sandwich structural panels<sup>24</sup> or as a protective layer to mitigate the impact or blast damage in reinforce concrete slab.<sup>25,26</sup>

#### **5.4 SUMMARY AND CONCLUSIONS**

In this chapter, the micromechanics and micro-mechanisms underlying the unique tensile and compressive behavior of SFR-ECC have been investigated, and the following findings are made:

1. The micromechanical parameters of SFR-ECC have been experimentally determined. The fiber/matrix interface exhibit chemical bond due to the addition of polymer latex admixtures. However, the chemical bond is discontinuous due to the discontinuous interface between polymeric material and HTPP fibers. The average chemical bond is measured to be  $2.83 \text{ J/m}^2$ . The frictional stress is measured to be  $1.01 \text{ MPa}$ . The slip-hardening coefficient is measured to be  $-0.0355$ , indicating slightly slip softening behavior. The snubbing coefficient is determined to be  $0.007$ , and such low value is associated with the weak SFR-ECC matrix.
2. Reduction of effective interfacial bond due to fiber bundle and elastic stretching of fibers are considered when deriving the analytic  $\sigma(\delta)$  relationship of SFR-ECC. The resulted curve is generally in good agreement with the measure curves from the single crack test.
3. Analytic investigation suggests that SFR-ECC satisfies the energy criterion (for achieving strain hardening behavior) comfortably, while the strength criterion is just met. The presence of chemical bond increases the margin for satisfying the strength criterion and therefore is considered beneficial for SFR-ECC.
4. The cellular-like ductile behavior of SFR-ECC under compression is a result of the cellular microstructure formed by large volume of small air pores (caused by air entrainment). Under compression, the successive collapse of air pores leads to the cellular-like compressive behavior and the fiber bridging further favors the cellular-like behavior.

This chapter provides in-depth understanding of the unique mechanical behavior of SFR-ECC. The findings and methodology used in this chapter will also be used in Chapter 6 to investigate the durability behavior of SFR-ECC under high rate loading.



## References

---

1. ASTM E399–12. Standard test method for linear-elastic plane-strain fracture toughness  $K_{Ic}$  of metallic materials.
2. Li VC, Mishra DK, Wu HC. Matrix design for pseudo strain-hardening fiber reinforced cementitious composites. *RILEM J Mater Struct* 1995;28(10):586–95.
3. Lin, Z., T. Kanda and V.C. Li, "On Interface Property Characterization and Performance of Fiber Reinforced Cementitious Composites," *J. Concrete Science and Engineering, RILEM*, Vol. 1, pp. 173-184, 1999.
4. Yang, E.H., Y. Yang, and V.C. Li, "Use of High Volumes of Fly Ash to Improve ECC Mechanical Properties and Material Greenness," *ACI Materials J.*, Vol.104, No.6, pp.620-628, Nov-Dec 2007.
5. Morton, J., and G. W. Groves. "The effect of metal wires on the fracture of a brittle-matrix composite." *Journal of Materials Science* 11.4 (1976): 617-622.
6. Li, V.C., and Wang, Y., and Backer, S. "Effect of Inclining Angle, Bundling, and Surface Treatment on Synthetic Fiber Pull-Out from a Cement Matrix", *J. Composites*, Vol. 21, 2, pp. 132-140, 1990.
7. Yang, E.H., and V.C. Li, "Fiber-bridging Constitutive Law of Engineered Cementitious Composites", *Journal of Advanced Concrete Technology*, Vol. 6, No.1, pp.181-193, February 2008
8. Wang, S. and Li, V. C., "Engineered Cementitious Composites with High-volume Fly Ash", *ACI Material Journal*, Vol 104, No. 3, May-June, 2007, pp. 233-241.
9. Huang, X., Ranade, R., Zhang, Q., Ni, W., and Li, V.C., "Mechanical and thermal properties of green lightweight engineered cementitious composites, *J. Construction and Building Materials*, 48, 954-960, 2013.
10. Yang E-H. Designing added functions in engineered cementitious composites. The University of Michigan, PhD Thesis (Civil Engineering); 2007. 276p.
11. Felekoğlu, B., Tosun-Felekoğlu, K., Ranade, R., Zhang, Q., and Li, V.C., "Influence of matrix flowability, fiber mixing procedure, and curing conditions on the mechanical performance of HTPP-ECC, . *Composites, Part B: Engineering*, 60, 359-370, 2014.
12. Li, V. C., C. Wu, S. Wang , A. Ogawa and T. Saito, "Interface Tailoring for Strain-hardening PVA-ECC," *ACI Materials Journal*, Vol. 99, No. 5, Sept.-Oct., 2002, pp. 463-472.
13. Wu, C., "Micromechanical Tailoring of PVA-ECC for Structural Applications," PhD Thesis, Department of Civil and Environmental Engineering, University of Michigan, Ann Arbor, USA, Jan., 2001.
14. Kanda, T., and V.C. Li, "Interface Property and Apparent Strength of High Strength Hydrophilic Fiber in Cement Matrix," *ASCE J. Materials in Civil Engineering*, Vol. 10, No. 1, pp. 5-13, 1998.
15. Li, V.C., Stang, H., and Krenchel, H., "Micromechanics of Crack Bridging in Fiber Reinforced Concrete", *J. of Materials and Structures*, 26, pp. 486-494, 1993.
16. Sahmaran, M., Ozbay, E., Yucel, H.E., Lachemi, M., and Li, V.C., "Frost resistance and microstructure of Engineered Cementitious Composites: Influence of fly ash and micro poly-vinyl-alcohol fiber." *Cement and Concrete Composites* 34.2 (2012): 156-165.

- 
17. Li, M., and Li, V. C., "Rheology, fiber dispersion, and robust properties of Engineered Cementitious Composites", *RILEM J. of Materials and Structures*, Vol.46, No.3, pp.405-420, 2013
  18. Kanda, T. and Li, V. C., "Multiple Cracking Sequence and Saturation in Fiber Reinforced Cementitious Composites," *Concrete Research and Technology, JCI*, Vol. 9, No. 2, pp. 19- 33, 1998.
  19. Ashby, Michael F., and RF Mehl Medalist. "The mechanical properties of cellular solids." *Metallurgical Transactions A* 14.9 (1983): 1755-1769.
  20. Miled, K., K. Sab, and R. Le Roy. "Particle size effect on EPS lightweight concrete compressive strength: experimental investigation and modelling." *Mechanics of Materials* 39.3 (2007): 222-240.
  21. Meille, S., et al. "Mechanical properties of porous ceramics in compression: On the transition between elastic, brittle, and cellular behavior." *Journal of the European Ceramic Society* 32.15 (2012): 3959-3967.
  22. Markaki, A. E., and T. W. Clyne. "The effect of cell wall microstructure on the deformation and fracture of aluminium-based foams." *Acta Materialia* 49.9 (2001): 1677-1686.
  23. Song, Hong-Wei, et al. "Fracture mechanisms and size effects of brittle metallic foams: In situ compression tests inside SEM." *Composites Science and Technology* 68.12 (2008): 2441-2450.
  24. Li, Guoqiang, and Venkata D. Muthyala. "A cement based syntactic foam." *Materials Science and Engineering: A* 478.1 (2008): 77-86.
  25. Wu, Chengqing, Liang Huang, and Deric John Oehlers. "Blast Testing of Aluminum Foam–Protected Reinforced Concrete Slabs." *Journal of Performance of Constructed Facilities* 25.5 (2010): 464-474.
  26. Schenker, A., Anteby, I., Nizri, E., Ostrach, B., Kivity, Y., Sadot, O., Haham, O., Michaelis, R., Gal, E., and Ben-Dor, G., "Foam-protected reinforced concrete structures under impact: experimental and numerical studies." *Journal of structural Engineering* 131.8 (2005): 1233-1242.

## CHAPTER 6 SFR-ECC UNDER HIGH RATE LOADING

In Chapter 4 and 5, the tensile and compressive properties of SFR-ECC under normal rate loading have been studied, and in this chapter, these properties under higher rate/impact loadings will be further investigated.

### 6.1 INTRODUCTION

SFR-ECC has been developed aiming at enhanced durability under multi-hazards as well as normal service conditions. Multi-hazard condition may involve impacts and high rate loading. In previous chapters, the tensile and compressive properties of SFR-ECC were characterized under quasi-static load with strain rate around  $10^{-4} \text{ s}^{-1}$ , however, under earthquakes and impacts, the strain rate could go up to  $10^1$ - $10^2 \text{ s}^{-1}$  and even higher under blast loads.<sup>1</sup> It is very important to investigate the behavior of SFR-ECC under those higher loading rates and ensure that the desirable performance of SFR-ECC is maintained.

Among all the mechanical properties, the tensile ductility is of most concern, since previous research<sup>2</sup> indicates that certain ECC made of PVA fibers can show significant reduction in tensile ductility as loading rate goes up, associated with increasing chemical bond under higher rate loading. However other researches<sup>3,4</sup> suggest that low density ECC and ECC produced with hydrophobic fibers, including polypropylene fibers (that are used in SFR-ECC), do not show significant rate dependency due to the absence of (or very low) chemical bond; rather the slight rate effect comes from increasing fiber strength and modulus with increasing loading rate.

In SFR-ECC, as discovered in Chapter 4, there exists chemical bond on the HTPP fiber/matrix interface, which might cause rate sensitivity of the tensile ductility. However, in Chapter 5, the analytic investigation also suggests that the chemical bond could positively affect the tensile ductility in SFR-ECC, unlike the case of PVA-ECC. Therefore, the tensile behavior of SFR-ECC under high rate loading cannot be predicted from past experience. It is critical to experimentally study the tensile property of SFR-ECC under high rate and impact loads.

In addition to the tensile property, in Chapter 4 and 5, the ductile compressive behavior of SFR-ECC has also been studied under quasi-static load. Whether this behavior is maintained under higher rate loadings is also of interest.

In this chapter, the macro-scale tensile and compressive properties of SFR-ECC are investigated under multiple strain rates ranging from  $10^{-4}$  to  $10^1$  s<sup>-1</sup>, covering quasi-static, earthquake and impact loads. The micromechanics underlying the rate effects of tensile behavior are also investigated using micromechanical modeling and scale linking techniques (as detailed in Chapter 5). Low velocity impact tests on SFR-ECC protected steel panels and I-beams were conducted to further evaluate the impact resistance of the fire protection material in actual structural configurations. In this chapter, the SFR-ECC Mix 2 (as detailed in Chapter 4) is used to represent all SFR-ECC mixtures.

## **6.2 COMPOSITE MECHANICAL PROPERTY**

### **6.2.1 Experimental procedures**

Uniaxial direct tension tests of SFR-ECC were conducted under multiple loading rates on dogbone shaped specimens as recommended by the Japan Society of Civil Engineers (JSCE) for high performance fiber reinforced cementitious composite<sup>5</sup>. 6 different displacement were selected

in this study: 0.008 mm/s, 0.08 mm/s, 0.8 mm/s, 8 mm/s, 80 mm/s and 800 mm/s. The loading rates correspond to tensile strain rates of  $10^{-4} \text{ s}^{-1}$ ,  $10^{-3} \text{ s}^{-1}$ ,  $10^{-2} \text{ s}^{-1}$ ,  $10^{-1} \text{ s}^{-1}$ ,  $10^0 \text{ s}^{-1}$ , and  $10^1 \text{ s}^{-1}$ . The detailed test procedures can be found in Chapter 4.

Digital image correlation (DIC) technique was also employed to study the crack widths of SFR-ECC under different loading rates. Prior to the tensile test, the specimen surface were painted white and marked with random black speckles. Photos were taking during the tensile test to track the displacement of the speckles. A commercial software was used to analyze the photos and extract the displacement field of the specimen based on relative displacement between the speckles. The strain field were also calculated, based on which the crack widths were calculated. In previous research, DIC procedure has been successfully used to study the crack pattern of ECC material.<sup>6</sup> Details of the DIC procedure can be found in the reference.

In this study, instead of measuring the crack widths under load, the residual crack widths were measured for specimens under different loading rates by taking and analyzing the photos before the test and after unloading. This is because that under high strain rate ( $10^{-1} \text{ s}^{-1}$  and above) loading scenarios, the tensile test became too fast (less than 1 second) to be photo documented using the regular camera.

The compressive property of SFR-ECC was characterized using direct uniaxial compressive test on a set of three 50.8 x 50.8 x 50.8 mm cube specimens under multiple displacement rates of 0.005 mm/s, 0.05 mm/s, 0.5 mm/s, 5 mm/s, 50 mm/s and 500 mm/s, corresponding to the same strain rates as the direct tensile test.

## 6.2.2 Results and discussions

### Tensile property

Representative tensile stress-strain curves of SFR-ECC obtained from the uniaxial direct tension test under various strain rates are plotted in **Fig.6.1**. It can be concluded from the tensile test results that SFR-ECC maintains the ductile behavior under all strain rates investigated. There is a general increasing trend of the Elastic modulus and tensile strengths (both first cracking strength and ultimate strength) as the strain rate increases. The tensile strain capacity shows little change from static load ( $10^{-4} \text{ s}^{-1}$ ) to strain rate of  $10^{-2} \text{ s}^{-1}$ , then increases at strain rate of  $10^{-1} \text{ s}^{-1}$ , and slightly decreases under higher strain rates ( $10^0 \text{ s}^{-1}$  and  $10^1 \text{ s}^{-1}$ ). This might indicate competing rate effects within SFR-ECC. Nevertheless, the average tensile strain capacity all exceeds 2% for all the 6 strain rates, which is about 200 times that of the conventional cement-based material. The tensile strengths and strain capacity of SFR-ECC under all strain rates are summarized in **Table 6.1**. The investigated strain rates cover static load, earthquake load and impact load. Therefore, it is expected that SFR-ECC will maintain its ductile behavior under earthquakes and impacts.

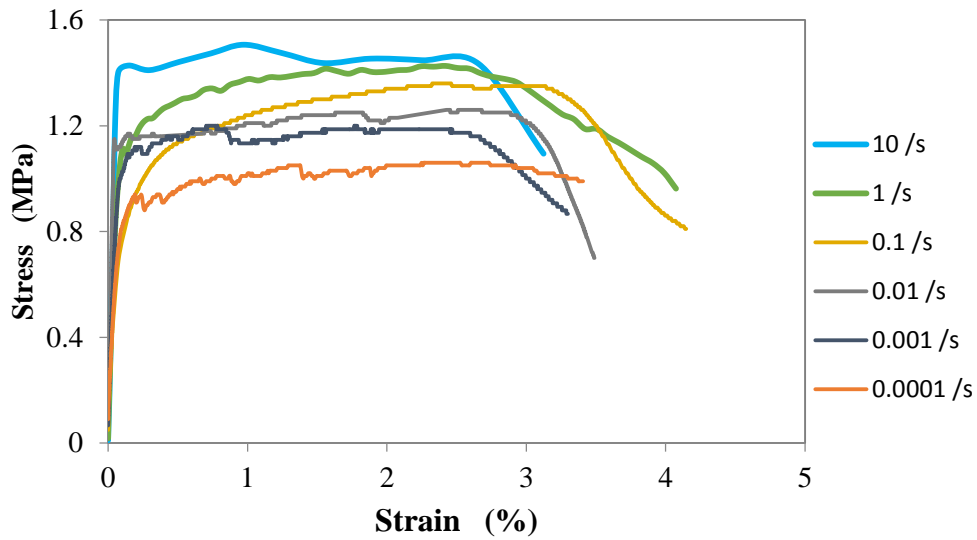


**Fig.6.1 SFR-ECC remains ductile under high rate loading**

The average  $\sigma_{cu} / \sigma_{cs}$  (ultimate tensile strength/first cracking strength) is also listed in **Table 6.1**. As the data suggests, the  $\sigma_{cu} / \sigma_{cs}$  under higher loading rates are slightly higher. All the  $\sigma_{cu} / \sigma_{cs}$  values are above 1, satisfying the strength criterion for strain hardening, but most of the ratios are slightly lower than the recommended practical value<sup>7</sup> of 1.2. However, due to the presence of large number of flaws (air pores), even with narrower margin between  $\sigma_{cu}$  and  $\sigma_{cs}$ , robust tensile strain hardening behavior has been still achieved SFR-ECC under all strain rates investigated.

The representative crack pattern for SFR-ECC specimens under different strain rates obtained from DIC analysis were presented in **Fig.6.2**. These selected representative specimens have tensile strain capacity close to the measured average value. From the figure, we can see all these specimens showed significant multiple cracking (above 20 cracks within 80 mm gage length).

However, the specimens that were loaded under higher strain rates ( $10^{-1} \text{ s}^{-1}$  and above) showed slightly more saturated cracking pattern, which could be associated with higher  $\sigma_{cu} / \sigma_{cs}$  ratio.

It was also observed that the crack widths became notably smaller under high strain rates above  $10^1 \text{ s}^{-1}$ . Under lower strain rates, the crack widths did not show noticeable change. The average residual crack width calculated from the DIC analysis are listed in **Table 6.2**.

Based on above observation, the change in tensile strain capacity could be a result of competing effect between the crack number and crack widths, which resulted a slight increase of strain capacity under strain rate of  $10^{-1} \text{ s}^{-1}$  and a decrease thereafter.

**Table 6.1 Tensile property of SFR-ECC under various strain rates**

Strain rates $\text{s}^{-1}$	Elastic modulus GPa	First cracking strength MPa	Ultimate tensile strength MPa	Tensile strain capacity %	$\sigma_{cu} / \sigma_{cs}$
$10^{-4}$	$2.01 \pm 0.18$	$1.01 \pm 0.08$	$1.15 \pm 0.07$	$2.5 \pm 0.8$	1.14
$10^{-3}$	$2.00 \pm 0.17$	$1.08 \pm 0.15$	$1.26 \pm 0.10$	$2.5 \pm 1.0$	1.17
$10^{-2}$	$2.17 \pm 0.37$	$1.20 \pm 0.07$	$1.30 \pm 0.08$	$2.4 \pm 0.6$	1.08
$10^{-1}$	$2.12 \pm 0.33$	$1.22 \pm 0.11$	$1.41 \pm 0.12$	$2.9 \pm 0.9$	1.16
$10^0$	$2.19 \pm 0.27$	$1.25 \pm 0.08$	$1.49 \pm 0.07$	$2.2 \pm 0.8$	1.19
$10^1$	$2.22 \pm 0.15$	$1.43 \pm 0.03$	$1.64 \pm 0.12$	$2.2 \pm 0.6$	1.15

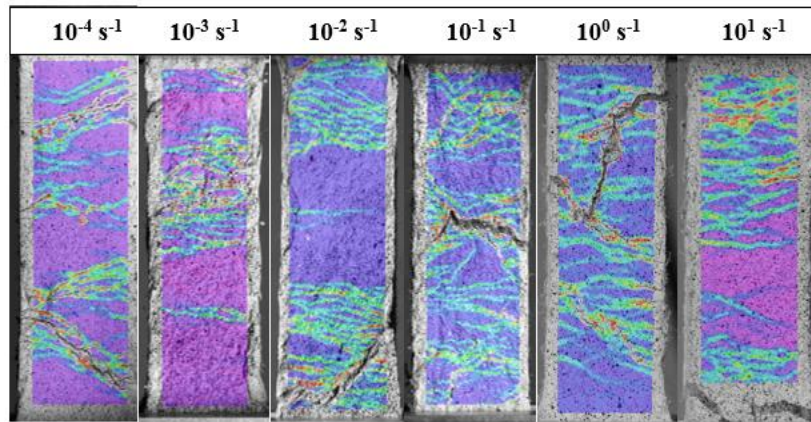


**Fig.6.2 Crack pattern of SFR-ECC under different strain rates**



**Table 6.2 Observed average residual crack width of SFR-ECC under various strain rates**

Strain rates $s^{-1}$	Average residual crack width* $\mu m$
$10^{-4}$	~35
$10^{-3}$	~40
$10^{-2}$	~40
$10^{-1}$	~35
$10^0$	~20
$10^1$	~20

\* These values are subject to large variability

### Compressive property

The measured compressive strengths of SFR-ECC under all investigated strain rates are listed in **Fig.6.3**. The presented compressive strengths are the strength of SFR-ECC at 10% compressive deformation (during the yielding stage). As observed, there is a general increasing trend of the compressive strength, and the increase is about 35% from strain rate of  $10^{-4} s^{-1}$  to  $10^1 s^{-1}$ . Under all strain rates, the ductile cellular-like compressive behavior (with densification) were observed. This is anticipated, since the cellular structure and the fiber bridging effect are the root cause of such behavior and the fiber bridging effect is well maintained under high rate loading.

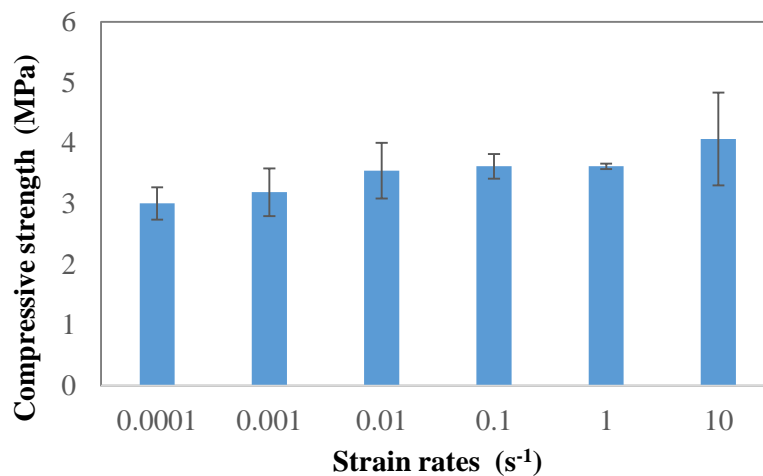


**Fig.6.3 Measured compressive strengths of SFR-ECC under various strain rates**

## 6.3 MICROMECHANICAL INVESTIGATION

### 6.3.1 Investigation procedure

Although macroscopically SFR-ECC showed minimal rate sensitivity, it is helpful to better understand the rate effect of fiber strength, modulus and chemical bond within the material. Therefore, micromechanical investigation under various loading rates were conducted. Matrix fracture toughness test<sup>8</sup>, fiber tensile test and single fiber pull-out test<sup>9</sup> were conducted to experimentally determine the matrix, fiber, and interfacial bond properties under multiple loading rates. Scale linking technique was used to compute the fiber bridging-crack opening  $\sigma(\delta)$  under different loading rates. 6 loading rates: 0.008 mm/s, 0.08 mm/s, 0.8 mm/s, 8 mm/s, 80 mm/s and 800 mm/s were selected (same as the composite tensile test) for this study. The details of the test procedures can be found in Chapter 5 and references.

### 6.3.2 Results and discussions

#### Matrix toughness

The measured matrix fracture toughness ( $K_m$ ) under different loading rates are listed in **Table 6.3**. Assuming the matrix elastic modulus is the same as the composite modulus (corresponding to the values in **Table 6.1**), the calculated  $J_{tip}$  for SFR-ECC under all loading rates is listed also listed in the table. The matrix toughness increases with increasing loading rate. This is anticipated and similar to typical cement-based materials.

The first cracking strengths and matrix fracture toughness ( $K_m$ ) are plotted together in **Fig.6.4**. From the figure, we can see that the first cracking strength generally follows the matrix fracture toughness trend, which is anticipated from the Irwin's fracture criterion.

**Table 6.3 Matrix toughness of SFR-ECC under various loading rates**

Displacement rates mm/s	$K_m$ MPa* $\sqrt{m}$	$J_{tip}$ J/m <sup>2</sup>
$8 \times 10^{-3}$	$0.090 \pm 0.01$	4.03
$8 \times 10^{-2}$	$0.091 \pm 0.01$	4.14
$8 \times 10^{-1}$	$0.097 \pm 0.02$	4.34
$8 \times 10^0$	$0.101 \pm 0.01$	4.81
$8 \times 10^1$	$0.103 \pm 0.02$	4.84
$8 \times 10^2$	$0.117 \pm 0.04$	6.17

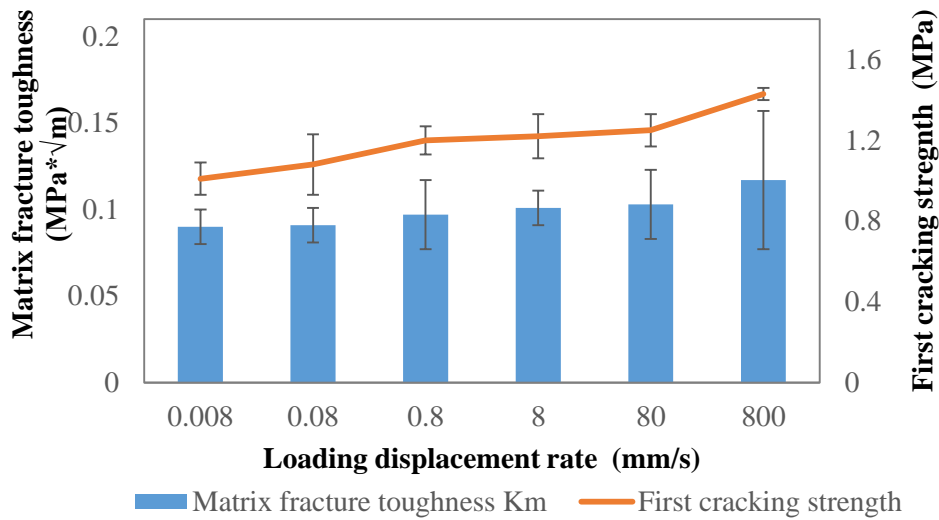


**Fig.6.4 Observed trend of first cracking strength and matrix fracture toughness of SFR-ECC**

### Fiber and fiber/matrix interfacial properties

The measure interfacial properties between the HTPP fiber and SFR-ECC matrix are listed in **Table 6.4**. From these data, we can see that the chemical bond  $G_d$  shows a notable increasing trend. The nonhomogeneous chemical bond were observed under all strain rates, similar to that under quasi-static load. The significant increase of chemical bond has been observed in previous study on PVA-ECC,<sup>1</sup> which is considered as the primary reason for the rate sensitivity of PVA-ECC. As shown in the table, the increase of chemical bond is significant, especially under high displacement rate ( $8 \times 10^2$  mm/s). Higher chemical bond generally leads to reduced

complementary energy  $J_b'$  and higher fiber bridging strength  $\sigma_0$ , which has mixed influence on the strain hardening potentials.

**Table 6.4 Measured fiber/matrix interfacial properties of SFR-ECC under various loading rates**

Displacement rate mm/s	$G_d$ J/m <sup>2</sup>	$\tau_0$ MPa	$\beta$	f	$\sigma_f$ MPa	$E_f$ GPa
$8 \times 10^{-3}$	2.83	1.01	-0.034	0.07	857	6.0
$8 \times 10^{-2}$	3.28	0.99	-0.020	0.07	1068	6.3
$8 \times 10^{-1}$	5.07	1.00	-0.033	0.07	1154	6.7
$8 \times 10^0$	5.44	1.09	-0.026	0.08	1200	7.3
$8 \times 10^1$	6.12	1.06	-0.021	0.08	1255	8.4
$8 \times 10^2$	10.20	1.14	-0.021	0.09	1312	8.9

The interfacial frictional bond  $\tau_0$  also shows a general increasing trend with increasing displacement rate. However, the increase is to a much smaller extent compared to the rate effect of the chemical bond. This observation also agrees with previous research findings on PVA-ECC interfacial behavior.

The slip hardening coefficient does not show noticeable trend, nevertheless the values are all negative and very close to zero, indicating a slight slip softening behavior. The snubbing coefficient also shows slightly upward trends, however, the data suggests very minimal snubbing effect due to the weak matrix.

The strength and modulus of HTPP fiber both increases significantly under higher rate loading. Previous study suggests that the increase of fiber strength and modulus is the most influential factor for the rate sensitivity of ECC made with hydrophobic fibers.<sup>4</sup>

## Analytical investigation

Scale linking technique was used in this chapter to study the influence of the rate effect in fiber and fiber/matrix interface level on the fiber bridging behavior of the cross-sections, which is then related to the composite behavior of SFR-ECC. The details of the scale linking can be found in Chapter 5.

The calculated fiber bridging parameters are summarized in **Table 6.5** and the computed fiber bridging  $\sigma(\delta)$  relationships under all displacement rates are plotted in **Fig.6.5**.

**Table 6.5** Calculated fiber bridging properties for SFR-ECC under various loading rates

Displacement rate mm/s	$J_b'$ J/m <sup>2</sup>	$\sigma_0$ MPa	$\delta_0$ μm	$J_b'/J_{tip}$	$\delta_{avg}$ μm
$8 \times 10^{-3}$	59.5	1.52	264	14.8	80
$8 \times 10^{-2}$	55.7	1.52	253	13.5	74
$8 \times 10^{-1}$	52.9	1.59	253	12.2	69
$8 \times 10^0$	60.1	1.75	242	12.5	70
$8 \times 10^1$	48.8	1.76	191	10.1	58
$8 \times 10^2$	49.4	2.01	191	8.0	52

In **Fig.6.5**, we can see that as the loading rate goes up, the fiber bridging curve shift upwards and leftwards. These are associated with combine effects of fiber strength, modulus and interfacial chemical bond increase. The complementary energy  $J_b'$ , as a result, experiences a downward trend with fluctuation. Combined with the increasing trend of  $J_{tip}$ , the  $J_b'/J_{tip}$  value decreases notably under high rate loading. Nevertheless, the ratio are all well above the recommended value of  $3^7$ , indicating strong satisfaction of the energy criterion for achieving strain hardening behavior.

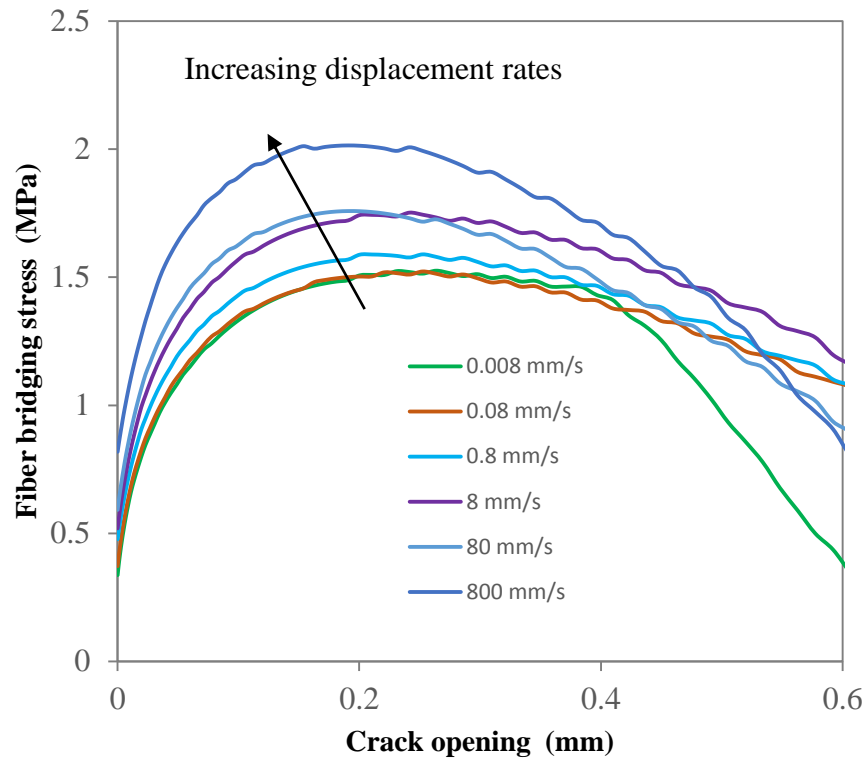


**Fig.6.5 Computed  $\sigma(\delta)$  curve of SFR-ECC under various loading rates**

The calculated fiber bridging strength  $\sigma_0$  generally matches the trend of the measured ultimate strength well as shown in **Fig.6.6**. In the tensile test, major fiber rupture was observed as the analytical computation predicted. The observed ultimate tensile strength (governed by the fiber bridging strength of the weakest cross-section) is around 82% of the calculated fiber bridging strength.

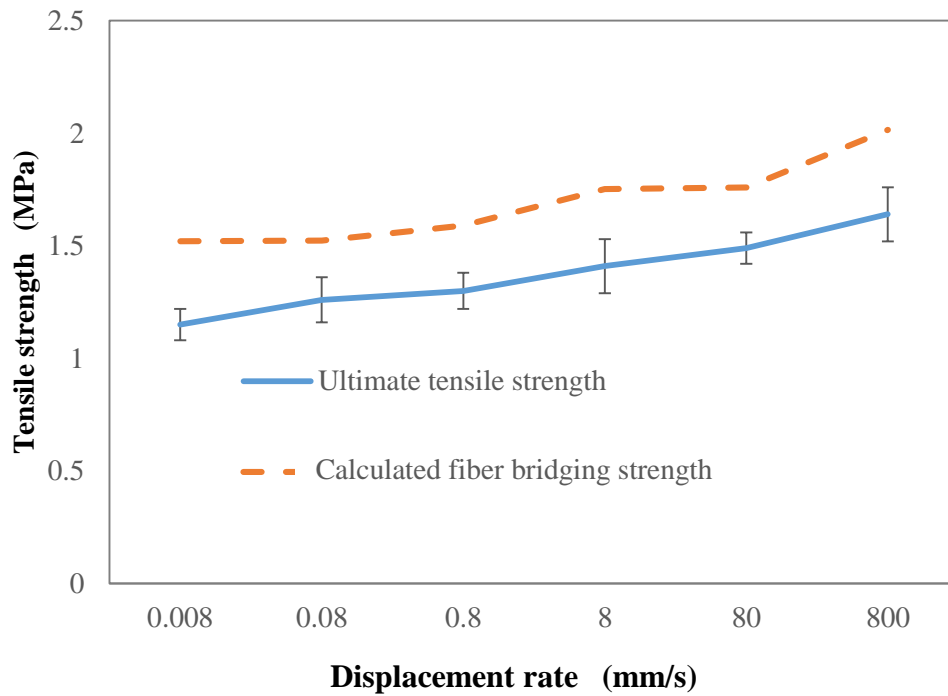


**Fig.6.6 Comparison between calculated fiber bridging strength and measured composite ultimate tensile strength of SFR-ECC**

The calculated  $\delta_0$  could be used as an indicator of the crack width, which shows a decreasing trend. However, a more reasonable estimation could be the crack opening at  $0.82\sigma_0$  (estimated ultimate tensile strength), which is also listed in **Table 6.5** (denoted as  $\delta_{avg}$ ). As we can see, the crack width decreases slightly from static load to  $8 \times 10^{-1}$  mm/s loading and then decreases notably under higher displacement rates. This trend agrees with the observed trend for average residual crack widths, although the numbers are notably larger, partly because the residual crack widths are lower than the crack widths under load. The sharp decrease in crack widths should

be the major reason for the reduction of tensile strain capacity under displacement rate above  $8 \times 10^1$  mm/s.

Macroscopically, the tensile ductility is governed by crack number and crack widths. Since the energy criterion is well satisfied under all loading rates, the strength criterion could be the control factor for crack number. We can use  $\sigma_0 / K_m$  to represent the potential for multiple cracking based on strength criterion.  $\sigma_0 / K_m$  is expected to be proportional to  $\sigma_{cu} / \sigma_{cs}$ . The calculated  $\delta_{avg}$  can be used as an estimate for the average crack widths.

**Fig.6.7** plotted the calculated  $\sigma_0 / K_m$  and  $\delta_{avg}$  values under various loading rates. It can be observed that the  $\sigma_0 / K_m$  are generally higher under higher displacement. This is because of the competing effect between increasing fiber bridging strength and increasing matrix fracture toughness. The  $\delta_{avg}$  decreases with increasing loading rates, however, the decrease is not significant until displacement rate reaches 80 mm/s. This figure could explain the slight increase of tensile ductility under 8 mm/s and decrease of ductility under higher displacement rates, which is a result of combined effect of crack number increase and crack widths decrease.



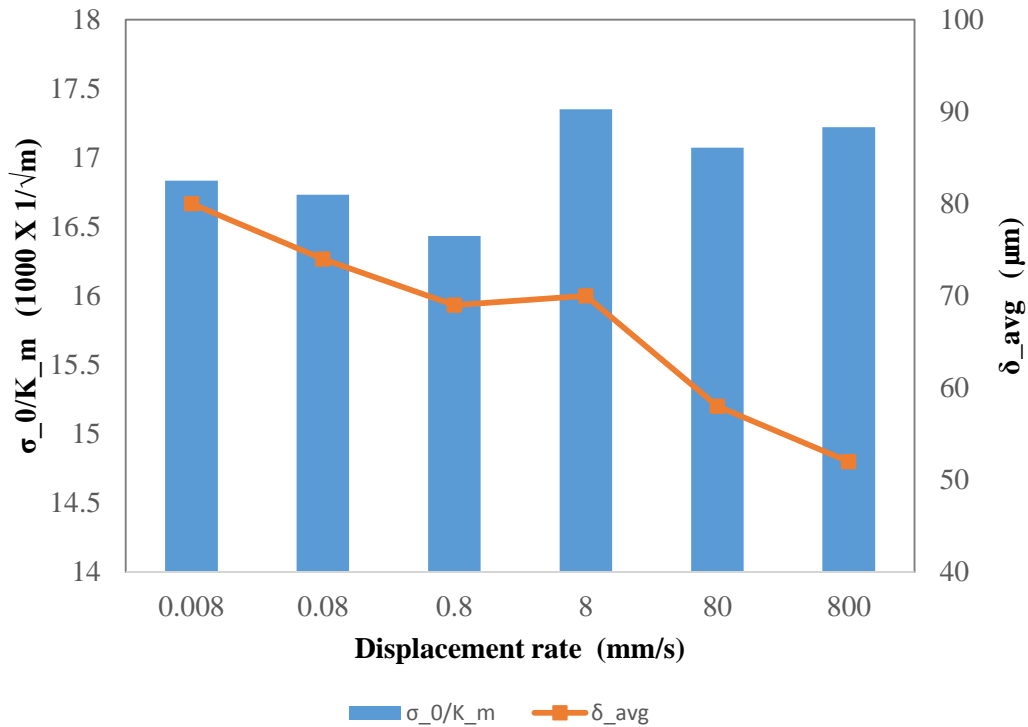
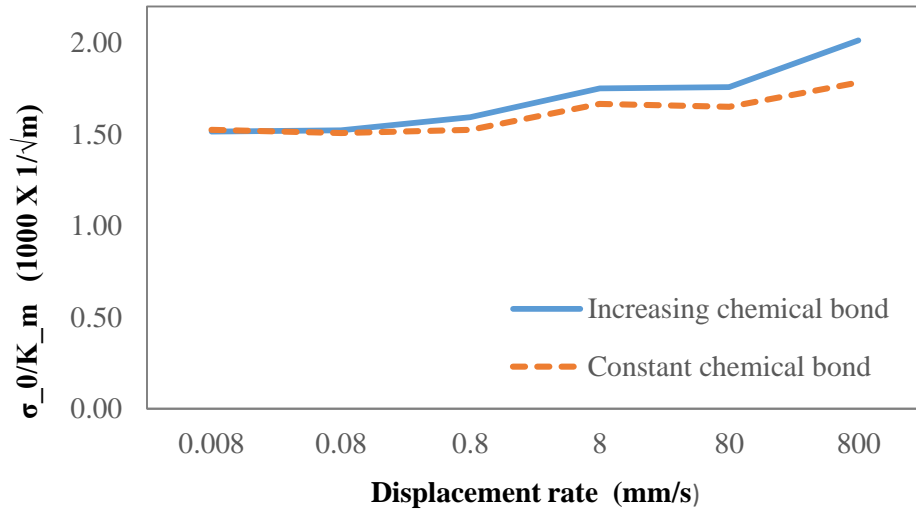


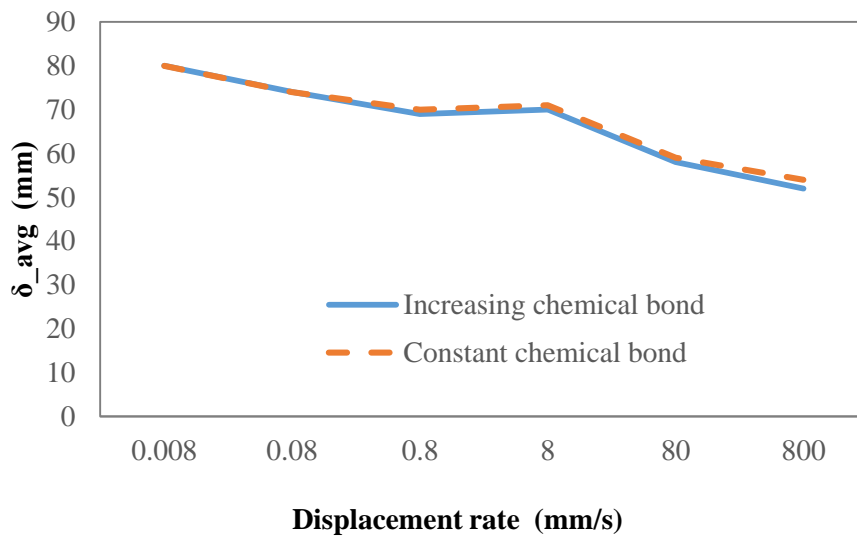
**Fig.6.7 Trend for  $\sigma_0 / K_m$  and  $\delta_{avg}$  under increasing displacement rates**

To further understand the effect of chemical bond, the analytical  $\sigma(\delta)$  curves were computed assuming constant chemical bond under all displacement rates. In **Fig.6.8(a)**, the calculated  $\sigma_0$  v.s. displacement rate is plotted. The  $\sigma_0$  computed with the measured chemical bond is also plotted for comparison. In **Fig.6.8(b)**, the computed  $\delta_{avg}$  v.s. displacement rate curve is also plotted. As the figures suggest, the increasing chemical bond further increases the fiber bridging capacity under high rate loading, which is considered beneficial as it increases the  $\sigma_{cu} / \sigma_{cs}$  and potentially the crack number. However, the fiber strength increase is shown to be more influential for the rate effect of  $\sigma_0$ , especially under higher displacement rates. The crack width is not noticeably affected as **Fig.6.8(b)** shows. Therefore, the increase of chemical bond

under increasing displacement rate is considered beneficial for maintaining the tensile ductility under high rate loading.



(a)



(b)

**Fig.6.8 The influence of chemical bond on computed (a) fiber bridging strength; (b) crack width**

In general, the tensile ductility of SFR-ECC is not significantly rate sensitive, especially under strain rates up to  $10^{-1} \text{ s}^{-1}$  as a result of combined effects of increasing matrix toughness, fiber modulus, fiber strength and interfacial chemical bond. The increasing chemical bond shows positive effect on maintaining the tensile ductility under higher rate loading, unlike the case of PVA-ECC.

## **6.4 IMPACT RESISTANCE OF SFR-ECC AS COATINGS ON STEEL MEMBERS**

Although SFR-ECC maintains the tensile ductility under higher strain rates, it is important to directly evaluate the impact resistance of SFR-ECC in actual structural configurations. Therefore low velocity impact tests were conducted on steel panels and I-beams coated with SFR-ECC or SFRM (controlled test) to directly evaluate the performance of SFR-ECC under real impacts.

Similar low velocity impact tests were previously conducted on FR-ECC protected members, which is documented in Chapter 2. In Chapter 2, these tests were used to validate the idea that by developing a highly cohesive fire protection material facilitated by tensile ductility, the durability of the fire protection system could be greatly enhanced. In this chapter, in addition to directly evaluating the impact resistance of SFR-ECC, the validity of the above idea will also be reconfirmed with the new SFR-ECC material.

### **6.4.1 Experimental procedure**

The impact was realized by dropping a weight of 14.5kg onto the panel specimens at a height of 0.48m or onto the I-beam specimens at a height of 0.86m. The impacts repeated 5 times for all the specimens. Such impacts did not cause structural damage or permanent deformation in the steel members, however, they could introduce damage to the SFR-ECC and SFRM. Therefore,

the low velocity impact test was used to study the behavior and failure mode of the fire protection material.

Three steel panel specimens were prepared and tested under impacts. Thin square structural steel panels with dimensions of 304.8mm x 304.8mm x 6.35 mm were used as steel substrates to emulate real steel structural elements. The mill-scale steel surface was cleaned with alcohol to remove oil and dirt before applying the fire protection materials. The first specimen is the control specimen. In this specimen, the steel panel was surface coated with a layer of acrylic latex-bonding agent and then sprayed with 25mm thick commercially available medium-density SFRM of similar density to SFR-ECC. For the second specimen, the steel panel was surface coated with the same bonding agent on the surface and sprayed with 25mm thick SFR-ECC. The third panel was directly sprayed with 25mm thick SFR-ECC without applying bonding agent. In the first and second specimen, the acrylic latex-based bonding agent was used to enhance interfacial adhesion. With strong adhesion, the different cohesive performance between SFR-ECC and SFRM can be clearly compared. The third specimen was tested to study the behavior of naturally bonded (without external bonding agent) SFR-ECC under impacts. In such case, both adhesive failure and cohesive failure are possible. The damage condition of the specimens was carefully examined and photo documented after each impact.

In addition to panel specimens, low velocity impact testing of steel I-beam section fully wrapped with SFR-ECC (and SFRM as control) was also performed using the drop-weight test. The beam specimens were prepared by applying approximately 13 mm thick SFR-ECC/SFRM layer on an S4x7.7 I-beam. The beam was 610 mm long, and the fireproofing material was applied on the mid 410 mm length leaving about 100 mm space at each end for simple-support.

Similarly to the study in Chapter 2, oil release agent was applied on steel surface to deliberately create a totally “bond-free” interface between steel and SFR-ECC to evaluate the performance of the fire-proofing material with no bond with steel under impact loadings. In the control specimen made with SFRM, no oil release agent was used and SFRM was naturally bonded to the steel surface. The damage condition of the specimens was carefully examined and photo documented after each impact.

#### **6.4.2 Result and discussion**

Similar to previous observed failure mode of high-density SFRM under impact (in Chapter 2) , drop weight impact test on the conventional medium-density SFRM protected steel panel also showed that even with the enforced strong adhesion at the interface, SFRM delaminated from the steel substrate under impacts. The final condition of the SFRM protected steel panel specimen after 5 impacts is shown in **Fig.6.9**. **Fig.6.9(a)** shows the final condition of the steel substrate. There was only a thin layer of cementitious SFRM left on the steel substrate; major portion of the SFRM was already delaminated, which can be more clearly seen in **Fig.6.9(c)**. **Fig.6.9(b)** shows the delaminated SFRM. This photo tells that under impacts, radial cracks formed within SFRM due to tensile stress. In addition, minor pieces on the edges and corners were delaminated prior to the delamination of the middle part. As discussed in Chapter 2, this indicates that during the delamination process, adjacent materials that were still bonded to the substrate did not prevent the delamination of the falling piece. This is also a result of the low cohesive strength of SFRM. This test result reiterates that that the low cohesive strength of SFRM is the root cause of the poor durability under impacts, which was found in Chapter 2.

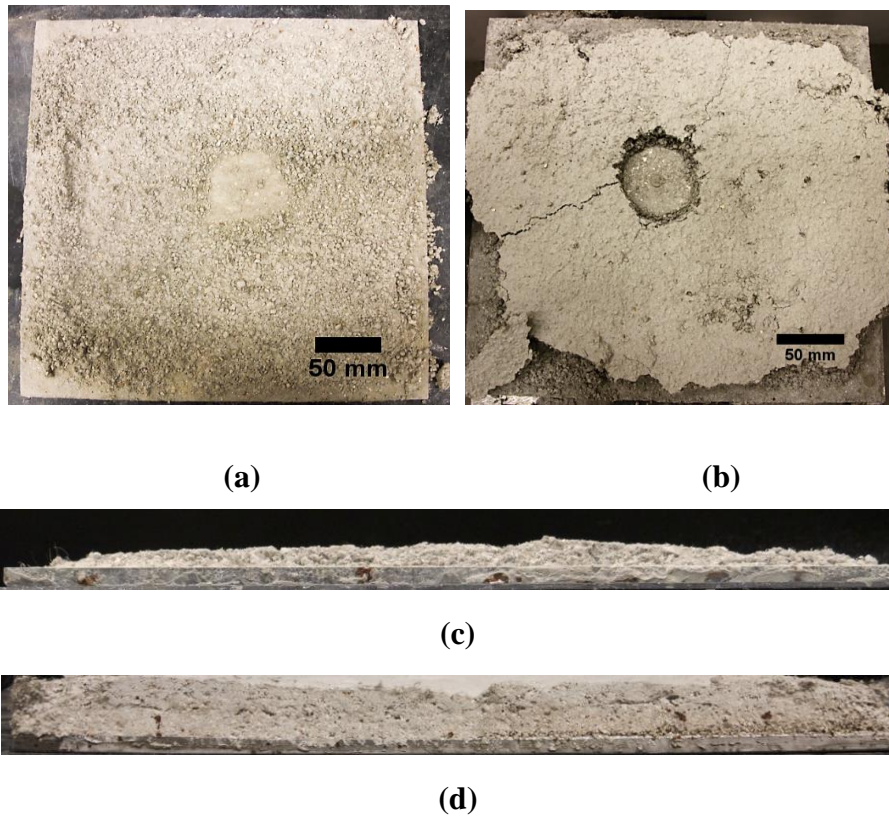


**Fig.6.9 Condition of conventional SFRM protected steel panel after impacts**  
**(a) Final condition of the steel panel; (b) Delaminated SFRM; (c) The thickness of residual SFRM on the steel panel after impacts as comparison to (d) The original thickness of the SFRM on the steel panel**

During the low velocity impact tests on SFR-ECC protected panels, the damage of the second panel specimen (with surface bonding agent) consisted of multiple cracks on the top surface as shown in **Fig.6.10**. The cracks are very tight; many of them are almost invisible. The formation of multiple fine cracks confirms that the highly ductile behavior of SFR-ECC is maintained under the impact load and with sprayed on material. In order to show the full crack pattern, in **Fig6.10(a)**, lines were drawn along the fine cracks using pencil to facilitate visibility in the photo. During the test, there was no delamination or detachment of the SFR-ECC observed. The integrity of the SFR-ECC fire protection was well preserved under impacts. Compared to SFRM, the highly cohesive

SFR-ECC exhibits much higher impact resistance, facilitated by the highly ductile behavior maintained under impact loads.

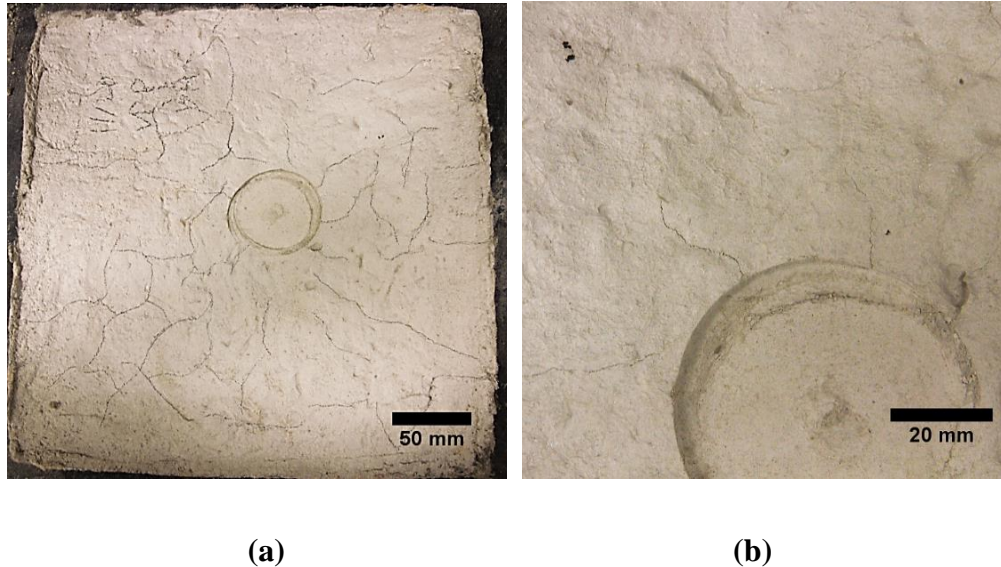
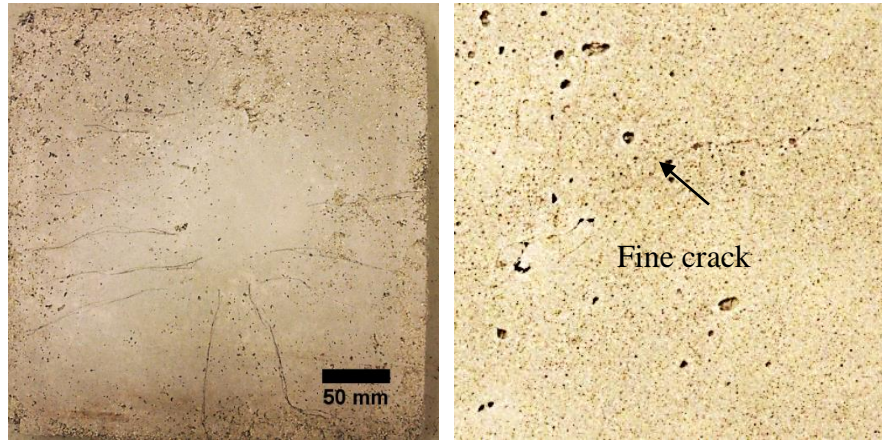


**Fig.6.10 Condition of SFR-ECC protected steel panel (with surface bonding agent) after impacts**  
**(a) Crack pattern on the top surface; (b) Close-up view of the cracks**

The second specimen possessed strong adhesion to steel facilitated by external bonding agent. In actual construction, bonding agent might not be necessary. The third specimen was used to evaluate the impact resistance of SFR-ECC that were naturally bonded to the steel panel.

The damage of the third specimen (*without* surface bonding agent) under impacts mainly consisted of local adhesive failure and formation of multiple fine cracks in SFR-ECC. During the entire impact test, no global adhesive failure was observed. The specimen was still attached to the steel substrate after all impacts. Local adhesive failure happened along the edges of the specimen while the central part remained bonded throughout the impacts. No visible damage was observed on the top surface of the specimen. To investigate the damage within the SFR-ECC material, after the test, the SFR-ECC was fully pried off the steel panel. Then it was observed that on the bottom surface, multiple fine flexural cracks formed as shown in **Fig.6.11**. Again, in **Fig.6.11(a)**, pencil

lines were drawn along the cracks to facilitate visibility in the photo. There were less cracks and the cracks were finer compare to the second specimen. This is because that part of the impact energy was dissipated through local debonding (adhesive failure) and only the remaining energy was dissipated through cracking.



(a)

(b)

**Fig.6.11 Cracking on the bottom surface of the SFR-ECC in SFR-ECC protected steel panel specimen (without surface bonding agent)**

**(a) Crack pattern; (b) Close-up view of the fine cracks**

As the impact test results shown, the integrity of the SFR-ECC in both specimens were preserved. Multiple cracking were observed in both specimens as the major damage mode for the SFR-ECC material itself, confriming the desired tensile behavior under impact loads. Local debonding (adhesive failure) was also observed in the third specimen (without surface bonding agent). However, no global debonding was observed, nor did the debonding cause any detachment of the fire protection material. Unlike the SFRM, with high cohesive strength, the part of SFR-ECC that were still bonded prevented the detachment of the debonded portion. The overall performance of SFR-ECC under impacts are therefore considered satisfactory.



In panel configuration, adhesive strength is critical since the debonding stress is normal to the interface. As described in Chapter 2, in fully wrapped beam configuration, the adhesion is not as critical for SFR-ECC. In such case, SFR-ECC can rely on its own cohesive strength to maintain integrity under impacts, which was referred to as the “wrapped-around durability” concept in Chapter 2. In fact, the panel configuration might be the least favorable configuration for SFR-ECC. In reality, under most conditions, SFR-ECC will be wrapping around flanges, angled shapes or openings that could provide extra support for SFR-ECC and disable the debonding failure mode.

**Fig.6.12(a)** shows the condition of the SFR-ECC on the steel beam after 5 repeated impacts. From the photo, we can conclude that the integrity of the SFR-ECC was well preserved under impacts. There was no visible loss of fire protection material. The condition of the SFRM wrapped beam after 5 impacts is shown in **Fig.6.12(b)**. The failure mode of the SFRM is again similar to the observed failure mode of another type of high density SFRM discussed in Chapter 2. It can be seen that SFRM on the flanges were totally lost after the impacts, leaving only a very thin layer of cementitious SFRM on the steel surface. The test demonstrates that even without interfacial adhesion, in a fully wrapped configuration, SFR-ECC achieves much higher impact resistance, compared to conventional SFRM, solely depending on its highly cohesive nature (that is well maintained under high rate loading). This also reconfirms the validity of the “wrapped-around durability” concept with the newly developed SFR-ECC.

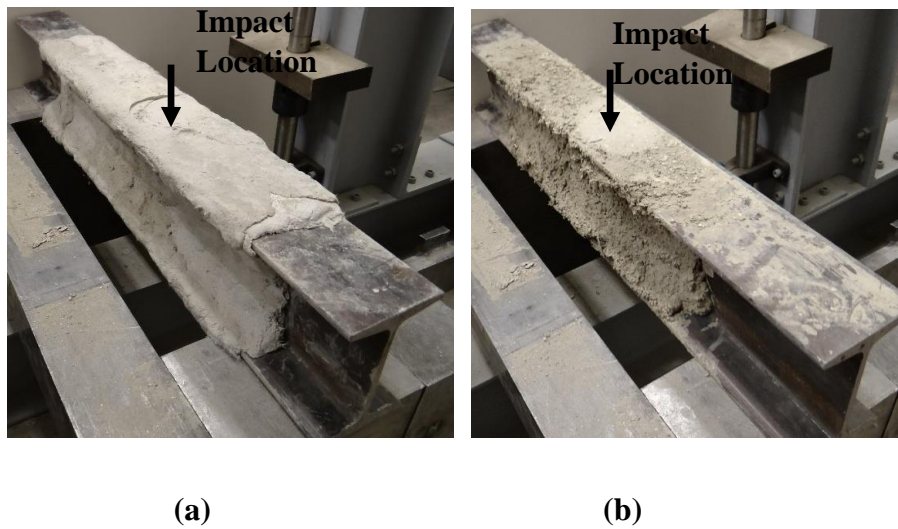


**Fig.6.12 Conditions of protected beams after impacts**  
**(a) SFR-ECC protected beam; (b) SFRM protected beam to impacts**

As the study indicates, in both panel and fully wrapped beam configuration, SFR-ECC exhibits much higher impact resistance than conventional SFRM, attributed to the highly cohesive nature of SFR-ECC facilitated by high tensile ductility under impact loads.

## 6.5 CONCLUSION

Based on the the research findings presented in this chapter, the following conclusions can be drawn:

1. SFR-ECC maintains high tensile strength and ductility under investigated strain rates from quasi-static load ( $10^{-4} \text{ s}^{-1}$ ) up to impact load ( $10^1 \text{ s}^{-1}$ ). The tensile ductility shows slight increase under  $10^{-1} \text{ s}^{-1}$  compare to that under quasi-static load and slight decrease under higher strain rates.
2. The compressive strength increases with increasing strain rates from quasi-static load ( $10^{-4} \text{ s}^{-1}$ ) up to impact load ( $10^1 \text{ s}^{-1}$ ). The ductile compressive behavior are maintained under all investigated strain rates.

3. The slight rate sensitivity of the tensile ductility is attributed to competing effect of decreasing crack width and increasing crack number under high rate loading, as a result of combined effect of increasing matrix toughness, fiber strength, fiber modulus, and chemical bond. The analytic investigation indicates the increasing chemical bond has positive effect on the tensile ductility under high rate loading.
4. Under impacts, SFR-ECC protected steel panel damaged in the form of local debonding and formation of multiple fine flexural cracks within SFR-ECC without loss of integrity or detachment. In contrast, the SFRM totally delaminated, leaving the steel panel unprotected. The impact resistance of SFR-ECC protected steel panels are much higher than that of the SFRM protected ones.
5. The “wrapped-around durability” concept is reconfirmed with the SFR-ECC material, providing extra safeguard for SFR-ECC protected steel members.

## References

---

1. Chandra, D. "A fracture mechanics based constitutive model for concrete under high loading rates" PhD Dissertation, University Park, PA: Pennsylvania State University, 1993
2. Yang, E.H., Li, V.C., "Strain-rate effects on the tensile behavior of strain-hardening cementitious composites. *Journal of Construction and Building Materials.*" 52(15), 96-104, 2014
3. Yang, E.H., Li, V.C., "Tailoring engineered cementitious composites for impact resistance." *Journal of Cement and Concrete Research.* 42, 1066-1071, 2012
4. Ranade, R, Li, V.C., and Heard, W.F., "Tensile Rate Effects in High Strength-High Ductility Concrete," *J. Cement and Concrete Research*, 68, 94-104, 2015
5. JSCE: Recommendations for Design and Construction of High. Performance Fiber Reinforced Cement Composites with Multiple Fine Cracks (HPFRCC), 2008
6. Ohno, M., and Li, V.C., "A feasibility study of strain hardening fiber reinforced fly ash-based geopolymer composites," *J. Construction and Building Materials*, 57, 163-168, 2014.
7. Kanda, T. and Li, V. C., "Multiple Cracking Sequence and Saturation in Fiber Reinforced Cementitious Composites," *Concrete Research and Technology, JCI*, 9(2), 19-33, 1998
8. ASTM E399–12. Standard test method for linear-elastic plane-strain fracture toughness  $K_{Ic}$  of metallic materials.
9. Lin, Z., T. Kanda and V.C. Li, "On Interface Property Characterization and Performance of Fiber Reinforced Cementitious Composites," *J. Concrete Science and Engineering, RILEM*, 1, 173-184, 1999.

## **CHAPTER 7 CONCLUDING REMARKS**

This chapter summarizes the major findings and their impacts in this doctoral research, and points out a few future research directions.

### **7.1 ACCOMPLISHMENT AND FINDINGS**

#### **7.1.1 Development and characterization of SFR-ECC**

SFR-ECC incorporating cement, water, vermiculites, microspheres (glass bubbles or fly ash cenospheres), acrylic latex admixtures, and HTPP fibers, has been developed. It is concluded that fire-resistive material can be made ductile, thus providing durability as a coating on steel members during the service life of a structure. The newly developed SFR-ECC has dry density of  $550\text{kg/m}^3$ , tensile strength from 0.68 to 1.1 MPa and strain capacity from 0.9 to 3.0%. These properties represent improvement by several times to several hundreds time when compared to those of conventional SFRM. The significant increase in cohesive properties minimizes common observations of dislodging of SFRM, and is expected to reduce the risk of rapid softening of steel structural members due to damage or loss of fire protection when exposed to fire hazards.

It is discovered that SFR-ECC exhibits ductile cellular-like behavior under compression, which enhances its energy absorption capacity.

The hypothesis that adhesion between SFR-ECC and steel can be enhanced using chemical additive is experimentally verified. The measured adhesive fracture energy of SFR-ECC mixes

(with structural steel) is found to range from 104.3 J/m<sup>2</sup> to 310.4 J/m<sup>2</sup> depending on SFR-ECC mixture design, significantly higher than that of conventional SFRM (11.1 J/m<sup>2</sup>). The SFR-ECC/steel interface exhibits a ductile fracture behavior associated with fibers bridging across the crack.

In addition to desirable durability properties, SFR-ECC exhibits apparent thermal conductivity and sprayability comparable to conventional SFRM, which ensures proper functionality of SFR-ECC as a sprayable fireproofing material.

Based on experimental findings of low velocity impact tests on SFR-ECC protected steel panels and beams, it is concluded that the high durability performance, especially high cohesion (mechanical property), helps to maintain integrity of SFR-ECC even under severe loadings (impacts). The formation of multiple micro-crack (instead of fracture and delamination) helps to dissipate the energy induced by impact loading without catastrophic failure, while conventional SFRM fails in brittle fracture and delamination.

Taking advantage of the highly cohesive nature of SFR-ECC, it is hypothesized that steel members can be protected by SFR-ECC even without depending on adhesion between the fire-resistive material and the steel. This “wrapped-around” concept is experimentally verified. SFR-ECC insulation systems can withstand impact load even without the presence of adhesion at the steel/SFR-ECC interface when the SFR-ECC forms a continuous enclosure around the steel member, which is impossible for low cohesive SFRM. Such mechanism provides extra level of safeguard in addition to interfacial adhesion and results in more robust durability behavior of SFR-ECC (high tolerance to local or even global adhesive failure).

To ensure that the cohesive properties of SFR-ECC are maintained under high strain-rate, direct tension test experiments were conducted at strain rates of  $10^{-4} \text{ s}^{-1}$  to  $10^1 \text{ s}^{-1}$ . It is concluded that tensile strength and ductility are both maintained through the four orders of magnitude in strain rates, representing quasi-static loading to low velocity impact loading. Under compression, the strength of SFR-ECC increases with increasing strain rates from quasi-static load ( $10^{-4} \text{ s}^{-1}$ ) up to impact load ( $10^1 \text{ s}^{-1}$ ) while maintaining the ductile cellular-like behavior under all strain rates.

### **7.1.2 Material investigation**

Micromechanical investigations have been conducted to investigate the underlying mechanisms behind the ductile behavior of SFR-ECC. It is discovered that the SFR-ECC matrix/HTPP fiber interface exhibits discontinuous chemical bond (with an average value of  $2.83 \text{ J/m}^2$ ), which is not typically found in HTPP/cement interface. The chemical bond is a result of the acrylic latex admixtures in SFR-ECC. Through analytical investigations, it is concluded that the presence of chemical bond increases the fiber bridging strength and fiber bridging complementary energy, and is therefore favorable for achieving strain hardening behavior of SFR-ECC. This is in contrast to previous investigations on ECCs using PVA fibers, where surface coating is needed to reduce chemical bonding in order to achieve composite strain-hardening.

It is concluded that that the slight rate sensitivity of the tensile ductility of SFR-ECC can be attributed to the competing effects of decreasing crack width and increasing crack number as the loading rate increases, resulting from combined effect of increasing matrix toughness, fiber strength, fiber modulus, and chemical bond. The enhanced chemical bond through the use of chemical admixture is found to have a positive effect on maintaining the tensile ductility of SFR-

ECC under high rate loading. This is again contradictory to the behavior of ECC reinforced with PVA fiber under high rate loading.

It is hypothesized that the ductile cellular-like behavior of SFR-ECC under compression is a result of the extremely porous cellular-like microstructure of SFR-ECC and further confinement provided by the fiber reinforcement. This hypothesis has been verified by microscopic investigations. It is found that the successive collapse of large volume of air pores (caused by air entrainment during mixing) leads to the cellular-like compressive behavior and the fiber bridging further confines the material, prevents fracture failure, and favors the cellular behavior under compression.

## **7.2 RESEARCH IMPACTS AND CONTRIBUTIONS**

This doctoral research presents a promising solution for solving the urgent problem of conventional SFRM for lacking of durability performance. The successful development of spray-applied fire-resistive engineered cementitious composites (SFR-ECC) with enhanced durability performance and proper functionality performance provides a durable alternative to the conventional SFRM. It is expected that SFR-ECC will greatly enhance structural fire safety, especially under multi-hazards, such as post-earthquake/impact fires.

Multiple performance requirements have been satisfied within one single SFR-ECC material following the parallel design procedure. This demonstrates the effectiveness and sets a successful example of employing parallel design concepts in developing multi-functional engineering material.



Durability and functionality properties of the developed SFR-ECC have been experimentally determined, providing useful data for further research and application of this material in large scale and real-world situation.

Fundamental knowledge regarding the micromechanical and microstructural mechanisms underlying the unique durability (adhesive, compressive and tensile) behavior of SFR-ECC has been generated. These findings can be used for further study of SFR-ECC under various conditions (e.g. environmental loading and elevated temperature) and as guidelines for developing materials requiring similar performance.

## **7.3 FUTURE RESEARCH DIRECTIONS**

### **7.3.1 Structural scale investigations of SFR-ECC**

The present research mainly focuses on the development, characterization and research on SFR-ECC at the material level. Before field application of SFR-ECC, large-scale structural-level testing and simulation are still needed to further verify the performance of SFR-ECC.

Standard fire resistance tests on SFR-ECC coated full-scale steel members are required to further evaluate the fire resistance of SFR-ECC and provide design guidelines to determine the required fire protection thickness for a given fire rating. The overall effectiveness of SFR-ECC as passive fire protection coating, in terms of withstanding combined thermal/mechanical load during the heating without major dislodgement or delamination and effectively insulating the steel members to keep them below critical failure temperature, will be directly evaluated by the test. SFR-ECC is measured to possess similar thermal insulating property to conventional SFRM. Regarding mechanical performance under elevated temperature, SFR-ECC is also expected to behave similarly to (if not better than) conventional SFRM. Therefore, the fire rating of SFR-ECC

coated steel members is expected to be similar to that of the conventional SFRM coated members given the same (or very similar) configuration, design thickness (of SFR-ECC/SFRM) and other detailing. However, this still needs to be experimentally verified.

Structural scale tests and/or simulations on SFR-ECC protected steel member under earthquake (or cyclic) load are needed to fully evaluate the advantage of SFR-ECC over conventional SFRM in structural level. This may also provide feedback for optimization of the material properties in the future.

### **7.3.2 SFR-ECC as energy absorption and protective material**

The unique combination of high tensile ductility and compressive ductility greatly improves the energy absorption capacity of SFR-ECC. This opens new possible applications for SFR-ECC other than fire protection material. As discussed in Chapter 5, SFR-ECC may be able to replace the metallic and synthetic foam and be used as protective foam layer for reinforced concrete members against impact and blast load.<sup>1,2,3</sup> It will be of great interest for researchers to verify the performance of SFR-ECC for such applications both experimentally and analytically.

### **7.3.3 Design for high temperature resistance**

A further step down the material design part is designing the material for maintaining the performance under elevated temperature. Present version of SFR-ECC maintains considerable tensile ductility up to temperature of 150 °C (before the melting of HTPP fiber), similarly to other ECC material developed with polymer fibers<sup>45</sup>.

Designing SFR-ECC to maintain the ductile behavior under higher temperature is expected to be beneficial for accommodating the deformation of steel due to combine mechanical and

thermal loads. This involves re-design the material using high temperature resistant fibers (e.g. basalt fiber) or even high temperature resistant binder materials (e.g. geopolymer binders).

To achieve efficient material design, fundamental knowledge of the temperature effect on the matrix, fiber property and fiber/matrix interfacial property needs to be generated for a wide range of temperatures.

Apart from SFR-ECC, this research direction is also of great interest for regular ECC, which is used in structural members, to further enhance the fire safety of the structure.

## References

---

1. Bhat, Prakash S., Vivian Chang, and Mo Li. "Effect of elevated temperature on strain-hardening engineered cementitious composites." *Construction and Building Materials* 69 (2014): 370-380.
2. Mechtcherine, Viktor, et al. "Coupled strain rate and temperature effects on the tensile behavior of strain-hardening cement-based composites (SHCC) with PVA fibers." *Cement and Concrete Research* 42.11 (2012): 1417-1427.
3. Schenker, A., I. Anteby, E. Nizri, B. Ostraich, Y. Kivity, O. Sadot, O. Haham, R. Michaelis, E. Gal, and G. Ben-Dor. "Foam-Protected Reinforced Concrete Structures under Impact: Experimental and Numerical Studies." *Journal of Structural Engineering* 131, no. 8 (2005): 1233-1242.
4. Li, Guoqiang, and Venkata D. Muthyala. "A cement based syntactic foam." *Materials Science and Engineering: A* 478.1 (2008): 77-86.
5. Ye, Z. Q., and G. W. Ma. "Effects of foam claddings for structure protection against blast loads." *Journal of engineering mechanics* 133.1 (2007): 41-47.